Università degli Studi di Catania

Dottorato di Ricerca in Scienza dei Materiali
XXIII Ciclo
Anno Accademico 2009-2010

Metal Nanoparticles Produced by Pulsed Laser Ablation in Liquid Environment

Elena Messina

Tutor:
Chiar.mo Prof. G. Compagnini

Coordinatore:
Chiar.mo Prof. A. Licciardello

A Roberto e
alla mia famiglia

Table of contents

1 SCOPE OF THIS THESIS

Particles in the nanometer size range have attracted increasing attention with the growing interest in nanoscience and nanotechnology. They hold potential as basic components for sub-wavelength optical devices, for surface-enhanced spectroscopy, for biological labelling and sensing, and for cancer therapy. For such applications, it is crucial to prepare metal nanoparticles with desired shape, and size distribution. The intense research in this field is also motivated by the search for new multifunctional materials that will allow designing of the modern miniature electronic and optical devices for ultra fast data communication and optical data storage. In this regard, the interaction of light with small particles depends strongly on the size, shape and composition of the particles, as well as on the composition of the medium in which the particles are embedded. A large number of chemical methods have been developed for the synthesis of silver and gold nanostructures that have well-controlled shapes, including triangular plates, cubes, wires and rods either in the form of colloidal dispersion or nanostructured films.

In this context, Pulsed Laser Ablation in Liquids (PLAL) has become a key method for synthesis of nanoparticles with controlled geometry and size. The ablation of metal targets in liquid environments is considered as a unfailing alternative to traditional chemical reduction methods for obtaining noble metal colloids, since such a strategy is considered

environmental friendly ("green" technique) with products which frequently do not need stabilizing molecules or other chemicals. Laser ablation-based synthesis can be implemented in pure deionized water or even in biologically-compatible aqueous solutions and can be coupled with well established protocols to enhance the sensitivity of classical vibrational spectroscopies such as in the case of Surface Enhanced Raman (SER) phenomena

In the past few years, the interest toward metals doped or bonded with carbon nanostructures has grown enormously, thanks to their wide use in optics and microelectronics applications.

Many recent publications deal with the possibility to incorporate heteroatom into carbon allotropes to significantly improve most of their physical properties.

On the other hand, metal nanoparticles are often susceptible to oxidation and aggregation (thus reducing their free energy), leading to a loss of their peculiar properties. Therefore, several efforts are devoted to protect metal nanoparticles with inert shells, to preserve them from surface modifications and to keep their main characteristics unchanged.

Finally, Gold nanoparticles are proven to be excellent candidate for *in vivo* micro-manipulation using Optical Tweezers.

Optical tweezers (OT), instruments based on a strongly focused laser beam, have been recently used to trap, manipulate, control and assemble metal and semiconducting nanostructures and their latest combination with Raman spectroscopy enables a thorough investigation of trapped samples. Historically, optical trapping of 36nm gold nanoparticles was first demonstrated by Svoboda & Block. More recently, the trapping range of gold spherical nanoparticles was expanded up to 250 nm, and very accurate measurements of optical forces have become possible[30]. A complete theory of optical trapping for spherical metal particles has been developed[31] that

was shown to be in very good agreement with experiments. The optical trapping of non-functionalized gold nanoparticles obtained by chemical methods can also originate particles agglomeration due to the observation of reversible electrical conductivity changes of the solution of the nanoparticles upon laser illumination or direct heating. Particles agglomeration during trapping experiments can be an obstacle for the accurate determination of the optical forces generated by the trapping beam and for the investigation of the effect of the plasmonic properties of nanoparticles on the trapping process.

In details, this PhD thesis pass through the synthesis of gold and silver nanoparticles, with final aim of studying optical properties and SERS applications.

Three fundamental aspect of metal nanoparticles were studied: (1) synthesis of nanostructures by PLAL using both the first (1064 nm) and the second harmonic (532 nm) wavelengths, (2) the interaction between LCCs (polyynes) and different metal nanoparticles (Cu, Au, Ag) to provide an insight into the factors influencing chemical (reactivity) and physical (optical) properties of the metal/LCCs core/shell systems produced at different experimental conditions, (3) optical tweezers working in the near-infrared of gold nanoaggregates.

The study of these nanostructures was performed by using transmission electron microscopy high resolution (HRTEM). TEM analysis allows accurate measurement of particles average size and is useful to investigate their crystalline or defective structure.

The optical properties were studied by UV-visible near infrared absorption spectroscopy. This analysis is particularly helpful to obtain raw information about size, structure and composition.

X-ray photoelectron spectroscopy (XPS) analysis is used to quantity the gold or silver to check oxidation state of metal atoms.

1.1 Metal nanoparticles

The term nanocluster refers to an aggregate of atoms or molecules from several tens to thousands. They are generally organized in structures having dimension ranging between 1 nm and 100 nm, and showing a large number of surface and interfaces.

Furthermore, metal nanoclusters must posses some requirement such as very well defined composition and monodisperse size distribution (size dispersion < 15%).

Nanostructures materials can be obtained by a large number of synthesis methods and their properties often depend on the fabrication route. Some commonly used deposition processes of metals nanoparticles are: electrodeposition, sputtering, vacuum deposition (Physical Vapour Deposition (PVD), Chemical Vapour Deposition (CVD)), diffusion processes. These deposition methods give some undesired effects, such as carrier gas in sputtered films, residual gas in the imperfect vacuum-evaporated films, solute molecules in vapour-deposited films and in film produced by diffusion process. There is evidence that the presence of electrons or ions in the condensing beam may influence structure in a marked way.

These technique operates in completely different conditions and can produce nanostructured thin films having very diverse structures and physical-chemical properties. Comprehensive information is seldom available to enable detailed comparisons between different films present problems related to the adhesion of the metals to the host matrix.

The growing interest of scientific community and industry in the area of the nanostructured materials led to develop and optimize further synthesis methods. There is not a universal method for production of small particles applicable to every element. In many cases the preparation

methods must be chosen according to constraints imposed by the experimental measurement techniques. For example, the measurement of the heat capacity requires good thermal contact between particles and a large amount of material, while optical absorption experiments can be more easily interpreted if the particle are widely dispersed in a matrix, The most exploited synthetic strategies can be divided in two different categories: *chemical routes* and *physical routes.*

Chemical synthesis is often the easiest and most economic route for the preparation of small metal particles. Chemical reactions for nanoparticles synthesis can be carried out in solid, liquid or gaseous state.

Chemical synthesis of metal powders can be performed in aqueous or no-aqueous media by introducing in solution some reducing agents. Nanostructured metals show a high reactivity due to their large surface area; for this reason the washing , filtration and drying processes, which follow the chemical synthesis, must be performed with great care in order to avoid hydrolysis or oxidation reactions.

One of the most conventional approaches in solid state chemistry for the synthesis of nanoclusters, is the use of solid precursors of the metal, like metal oxides or organometallic compounds.

An organometallic compound is one which has a direct metal to carbon bond.

Advantages of using organometallic compounds are that precursors can be synthesized that have the constituents in molecular proximity to each other and that can be decomposed at relatively low temperatures to yield the delivered final product. These reactions can be used in fine chemicals synthesis.

In some of the earliest systematic studies for the production of small particles, the evaporation of the material under a relatively high pressure of an inert gas, such as helium, neon or argon was exploited. This

methods can be used to create a fairly narrow size distribution of most metal, semiconductor particles and many compounds.
In these last years advanced methods to produce any kind of cluster assembled materials in a wide range of size have been developed.
In this regards , it has been shown that the intense and ultra-short linearly polarized laser pulses are able to ablate a metal surface immersed in a liquid, producing metal nanoparticles.
This research work was focused on the nanostructured materials prepared by laser ablation in liquid.
As already mentioned, the great interest on nanocluster science is due to their characteristic to exist in an intermediate state between the nuclear and the bulk state. This allowed advanced materials to be synthetized, having unique properties with respect to the traditional materials.
In the following, some peculiar properties of these materials are reviewed.

1.2-Uv-Vis characterization of metal nanoparticles using Mie theory

Among all nanomaterials, the nanoparticles are very attractive due to their physical and chemical properties and to their applications in a wide range of fields. In nature, nanoparticles are present almost everywhere and can be found as solids (all crystals are “nanocrystal” in their early existence), liquids (droplets) or gases (gas bubbles in nanoporous materials).
Metal nanoparticles are of great interest because of their size- and shape-dependent properties. Among those, the nanoparticles made of noble

metals like gold and silver started to be intensively studied in the last decades, because of their unique properties which make them useful for applications in several rapidly developing fields like photonics, information technology, cancer treatment and in vivo Raman spectroscopy [1]. The unique optical properties of small metallic particles are exploited in the manufacturing of optical filters, labels for bio-macromolecules, in reversible photosensitive monochromatic glasses, for optical switching based on their large, ultrafast nonlinear optical response, and for optical trapping due to their high polarizability.

For the beauty and resilience of their colour, since the time of the Romans, the metal nanoparticles (at that time known as gold powder) are used as decorative pigments. Maybe the most interesting and precious evidence of this use of the metal nanoparticles is the Lycurgus Cup (Fig.1.1), famous for its unique feature of changing colour depending on the light in which is viewed. The glass analysis reviled that it contains a small amount of ~ 70nm metal crystals containing Ag and Au in a molar ratio of 14:1.

Fig 1.1: Lycurgus Cup (4th century AD)

Even if their were used in stained glasses very early, the first systematic study of the synthesis and colors of colloidal gold was done only in 1857 by Michael Faraday [2]. He attributed the beautiful reds, burgundy, or purples colors of the stained-glasses to the presence of "very finely divided dispersed gold" (known today as gold nanoparticles). Since then thousands of scientific papers have been published on the synthesis, modification, properties, and assembly of metal nanoparticles, all this leading not only to reliable procedures for the preparation of metal nanoparticles of any desired size and shape, but also to the understanding of many of their physic-chemical features.

Modifying the size or shape of the nanoparticles results in a change of their colour. This effect is due to the occurrence of the surface plasmon resonance [3], the frequency at which conduction electrons oscillate in response to the alternating electric field of incident electromagnetic radiation (Fig. 1.2).

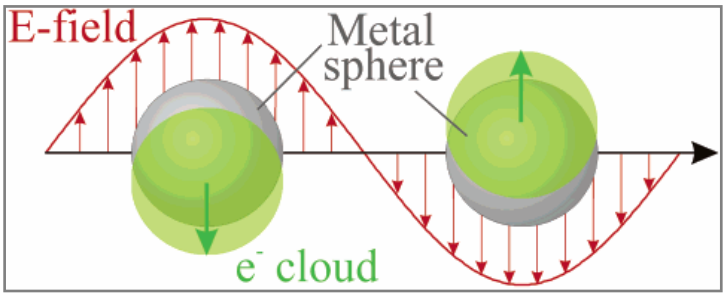

Fig 1.2: Schematic of plasmon oscillation for a sphere, showing the displacement of the conduction electron charge cloud relative to the nuclei.

Therefore, the interest in the optical spectra of metal hydrosols and nanocomposites in these last decades is essentially motivated by the fruitful information expected to be gained on the electronic structure and the dynamics of the delocalized conduction electrons. Most works have focused on the surface plasmon excitation (the dipolar Mie resonance) which dominate the photoabsorption spectra in the near UV and visible range for metal particles of diameter much lower than the wavelength of light.

So the colloidal suspension of noble metal particles were subjected to spectral analysis using a Perkin Elmer Lambda 2 spectrometer in the region 190-1100 nm, with a 1 nm resolution power.

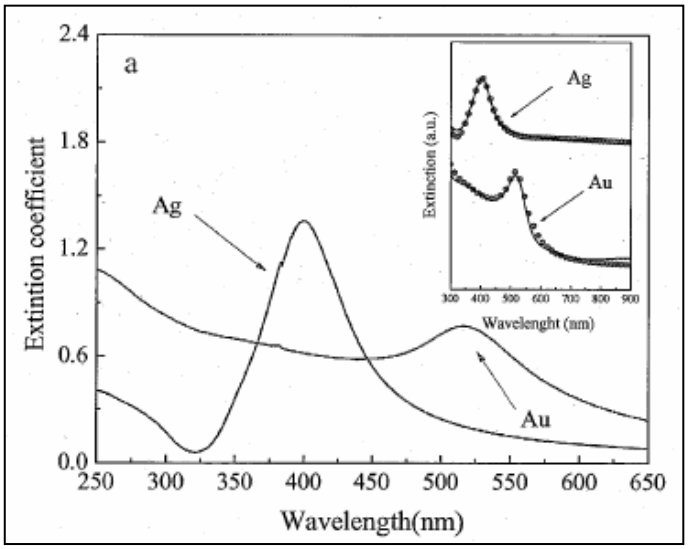

Fig1.3: Surface plasmonic resonance spectra of silver and gold nanoparticles. The inset shows the best fit of experimental spectra (dot) with the Mie-Gans model we have adopted (continuous lines).

The extinction of each sample was monitored in the relevant plasmonic resonance (PR) region that is around 400 nm for silver and around 520 for gold.

Typical PR spectra of these samples are shown in figure 1.3. The reader may see the noticeable intensity difference between gold and silver PR spectra . The role played by the complex dielectric constant of two metals in producing these differences has been analysed.

The visible absorption (PR) of these colloids is instead interpreted at the ligh of the Mie theory [4], introducing the Gans approximation [5], to take into account the role played by the dielectric function of liquid medium in which the colloids are sunspended.

Therefore, our spectra have been modelled, in the framework of Mie's theory, with the equation given by Papavassiliou [6], for the extinction coefficient K defined for N particles of volume V.

In this regard, if one consider that the extinction coefficient of a well dispersed collection of small particles, it is possible to obtain a simple expression in the cases in which ε_m is real and frequency independent, so that the extinction coefficient for *N* particles of volume *V* is given by the following equation:

$$k = 4.5 \times 10^7 NV \frac{E\varepsilon_m{}^{3/2}\varepsilon_2}{(\varepsilon_1 + 2\varepsilon_m)^2 + \varepsilon_2^2}$$

In this equation *E* is the photon energy in eV, *V* is the particle volume in m^3, ε_1 and ε_2 are the real and imaginary components of complex dielectric function. It is interesting to note that *k* has the dimensions of a cross-section (m^2), which can be directly considered for a valuation of the total

amount of metallic atoms present in the sample, through the use of the atomic density.

In this regard, we would like to stress that HR-TEM data are of relevant importance for a check of the sample shape or size.

In fact, for particles smaller than the bulk electronic mean-free path, the dielectric function of the metal must be corrected for quantum size effects.

This point must be considered with much attention, because it directly influences the particles' optical response and may be taken into account if one considers a classic Drude model.

In this case the dielectric function of each metallic cluster can be expressed as

$$\varepsilon = \varepsilon_b(E) + 1 - {E_p}^2/(E^2 + i\lambda E).$$

In this equation λ, correlated with the experimental width of the Mie absorption, can be considered as a damping factor to make terms on the right-hand side of equation, excluding the $\varepsilon_b(E)$ term, when $E = E_p$, *i.e.* at resonance conditions. It measures also the mean collision rate of conduction electrons at optical frequencies. $\varepsilon_b(E)$ is the contribution coming from interband transitions and from all other non-conduction electrons to the dielectric function of the metal, E_p is the plasma energy of free electrons, *i.e.* the PR energy at the absorption maximum.

When the particles are not too small, one can correct the dielectric function approximately by modifying the λ value. For very small particles the quantum size effect corrections can be complicated and may result in band narrowing, band splitting and frequency shifts in either directions from the PR band centre of bulk particles.

The range of size for this correction on the PR spectra has been detailed in ref. [7], and this is the case in our experiments.
The general expression which takes into account a classic quantum size effect relatively to λ quantity is to following:

$$\lambda = \lambda_B + A\,\nu_F/R.$$

Recently is has been shown [8,9] that it is possible to fit, by the use of very few fitting parameters, the surface plasmon spectra of gold colloids starting from the known bulk optical constants of the metal and correcting them for the above-mentioned quantum size effects.
Figure 1.4 shows the simulated PR spectra of silver and gold, when the simulation was performed by taking into account the role of the complex dielectric function of the system constituted by water and the relevant metal colloids.

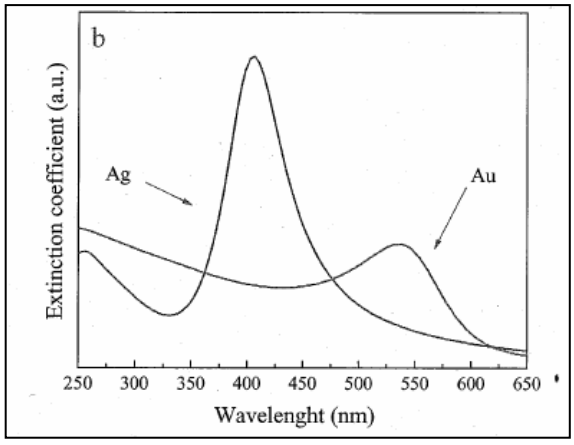

Fig. 1.4: Simulated PR spectra of silver and gold nanocolloids in water.

In our laboratory either SERS [10] and catalytic application [11] have been carried out in there last years by the use of silver and gold nanoclusters. Especially in the latter case, an estimative measure of gold particle dimensions have been made by low-frequency Raman- modes (LOFIS modes) and their behaviour under different polarization conditions of incident light [12]. It is well known fact, since the pioneer work by Lamb [13], that surface acoustic phonons propagate in assumed spherical nanometric objects, producing dilatational and shear motions that scatter quasi elastically the visible light as a consequence of density fluctuations [14-16].

The Raman frequency shift, with respect to the elastic peak, is inversely correlated to the radius of the particles through the sound propagation speed and a dimensionless constant whose value is assumed to vary within a restricted range between 0.7 and 0.9, depending on the material [14-16].

Due to acoustic nature of these features in the low-frequency Raman spectra of the nano-objects, one can retrieve analogies with the hydrodynamic triplet of the Rayleigh-Brillouin spectra [17], where the Brillouin frequency shift is proportional to the sound propagation speed in the relevant medium through the transferred wave vector. On the other hand, in the equation describing the transferred wave vector, one has at the denominator the wavelength of the scattered light, which plays the role of length as that of the particle size in the LOFIS spectrum counterpart.

1.3-Thermodynamic Properties

Almost any properties in a solid in associated with a particular length scale, below this length, the properties vary. As the size decreases to the nanometer scale, the thermodynamic properties are significantly different form those of the bulk. This is mainly related to a very increased number of atoms or molecular units that lie on the surface.

An interesting physical property is the melting point. It is well know the melting point of small particles may differ form their bulk value. It has been reported that nanoparticles melt at temperature significantly below their equilibrium melting points. This reduction of melting point with size is not restricted to any particular material but it was found in a wide variety of materials: metals, semiconductors, and molecular organic crystals. It seems that the melting process beings with the formation of a liquid "skin" layer around the particles. The depression of the melting point of small particles can be explained in term of a higher surface energy contribution to the Gibbs free energy of the particles, as a significant fraction of atoms lie in the surface. In order to explain the experimental data on the lowering of the melting temperature for small nanoparticles, some theoretical models have been proposed. The first one was presented by Palow in 1909 [18].

Theoretical phenomenological considerations Pelow to develop a quantitative relationship between the melting temperature, T_m, and the particle size. The Palow correlation is not quantitatively accurate, but it is still often used to estimate the size dependence of T_m .Afterwards, other models have been proposed, based on various assumptions [19-22].

The general result of most of the experimental, theoretical, and computer simulation studies suggest that the melting temperature, T_m, depends on the clusters size with the relationship:

(3) $$T_m = T_b - \frac{C}{R}$$

Where *R* in the radius of a spherical nanoparticles, T_b is the bulk melting temperature, and *C* is a constant depending on the material in specified conditions.

One of the most famous relations between the particle size and the melting point was proposed by Buffat and Borel [23].

Their version of the modified Palow relation is:

(4) $$\frac{T_m(r)}{T_b} = 1 - \frac{4}{\rho_s \lambda}\left\{\gamma_s - \gamma_1(\rho_s/\rho_l)^{2/3}\right\} 1/D$$

where D is the particle diameter, λ is the heat of fusion and ρ and γ are the density and surface free energy of the solid (*s*) and the liquid (*l*). The equation (4) gives a good descriptions of the experimental observations [24].

Zhao et al. studied the melting properties of size-selected isolated silver nanoparticles by using molecular dynamics simulation. They based their studies on phenomenological models that predict, at the melting point, the coexistence of a solid sphere core and a concentric liquid shell of a critical thickness, t_0.

The relation proposed by Zhao is reported below:

(5) $$T_b - T_m = 2T_b/\lambda \left\{ \gamma_{sl}/\rho_s(R-t_0) + \gamma_{lv}/R(1/\rho_s - 1/\rho_l) \right\}$$

where γ_{sl} is the interfacial surface tension between the solid and the liquid, while γ_{lv} is the one between the liquid and its vapour. By substituting the following values for silver nanoparticles:
T_b = 960.7 ºC
λ = 1.06 x 10^9 erg/g
ρ_s = 10.49 g/cm^3
ρ_l = 9.35 g/cm^3
γ_{sl} = 184 dyn/cm
γ_{lv} = 910 dyn/cm

equation **(5)** becomes:

(6) $T_m = 960.7-2463\ (1/0.603(R-t_0) + 1/R)$

Other later theoretical treatments have improved the accordance with the experimental data, but they all predict the inverse dependence. In addition large depressions of the melting point, about 500 ºC, were observed in 5 nm gold nanoparticles and about 140 ºC for 4 nm size aluminum particles.
There is also a large change in the vapour pressure of small particles due to the high curvature. This is called the " Gibbs-Thompson effect" and can be described by the "Kelvin equation", originally proposed for small liquid droplets and later extended to the phase transition of nanoparticles. The Kelvin equation is reported below:

(7) $P = P^* e^{(-2\gamma/vm\ r\ RT)}$

where P* is the pressure of the liquid, γ is the surface tension, v_m is the molar volume, and r is the radius of the droplet.

1.4-Chemical Properties

As mentioned, the surface atom/volume atom ratio is mainly responsible of the peculiar properties of nanoparticles. This becomes particularly important in the chemical reactivity areas. It is well known that when matter is subdivided in such a way that the surface area is large, it becomes more reactive. Therefore, the use of nanoparticles is a very attractive area to develop matrices for any chemical reaction, this could be particularly interesting for example in pollution clean-up, and it is being seriously pursued, *e.g.* to destroy chlorinated hydrocarbons.

Another area in chemistry where the high surface area of nanoparticles has been exploited for many years is in the heterogeneous catalysis. In this case the active catalytic component may be a metal or a metal oxide, which is usually present in small quantities. The heterogeneous catalysis are prepared in the form of highly dispersed particulate material, often in conjunction with molecular sieve, and in the form of porous materials for either chemical processing to synthesize compounds or to clean up pollutants by catalyze action. An example of this is the use of TiO_2 nanoparticles that catalyze the formation of free radicals, which can be used to destroy bacteria, viruses or hydrocarbon contaminants [25].

Fundamentally, catalysis involves a cyclic process in which a site on a catalyst forms a complex with reactants from which products are desorbed, thereby restoring the original sites and continuing the cycle. In nanostructured materials the active site of the reaction may be a croup of cluster of neighboring atoms on the catalyst surface, or a species absorbed onto the catalyst. These sites are associated with surface structures, lattice defects, and edges or corners of crystallites. Using a number of different synthesis process it is now some control over aspects such at the lattice parameters and the amount or type of internal defects

with a meta-stable structure quite different from what is expected with a normal equilibrium process. Furthermore, as the crystallite size decreases below 10 nm, and even below 5 nm, surface atoms will start to dominate while, at the same time, other structures, such as triple junctions, will be more and more present. The surface design of materials, as well as the increased presence of these structures could have a large impact on the properties of catalytic materials.

In catalytic reactions, metal clusters must allow the migration of coordinated ligands from a metallic atom to another one (CO, H etc.). This mobility is important in catalysis because it allows atoms or molecules to approach each other. For example, CO and H are common ligands on metal clusters, so they give the opportunity for the development of selective catalyst for synthesis gas conversion.

In addition, unusual coordination modes of a ligand to more than one metal atom were observed. In fact, some ligands are mostly found in clusters because they need stabilization by bonding to several metal atoms (CCO, BCO, CS, SO, CH, PO, etc.). Therefore, it is possible to stabilize unstable or highly reactive intermediate species in solution by supporting them on a cluster. Isolation of such metal clusters containing rare ligand, by multi-metal attachment allowed the study the elementary reaction steps involved in catalysis.

Metallic nanoparticles with an average grain size between 1 to 20 nm, such as Pt or Rh, dispersed on various substrates like SiO_2 or Al_2O_3 have been often used in heterogeneous catalysis [26].

These materials have been used extensively in many industries, such as petrochemical production, automobile emission control and fine chemical synthesis.

Recent studies showed that surface diffusivity can be significantly higher than in the bulk. This suggest that the atomic transport in a nanometric cluster is faster, since most of the atoms are on the surface.

Therefore, all cluster chemical reaction are greatly affected by several factors such as the atomic structure, the steric effects, the atom bond energy, etc., and a strong dependence on the number of atoms which form the cluster was observed. Studies on the reactivity of the clusters were conducted by saturating such nanometric aggregates with different types of adsorbed molecules. From the number of adsorbed molecules, the nature of the absorption sites was deducted, thus suggesting the possible structure of the clusters. Usually, metal clusters have a roughly spherical shape. In addition, it was observed that the ratio of the absorbed species and the surface metal atoms is less than 1 for metals of first transition series.

In many cases, for cluster having specific dimension, a very narrow distribution of absorbed species was detected, suggesting a quite rigid conformation with only one structure. In those cases when saturation was reached, bimodal distributions were detected and the presence of two or more isomeric species was suggested.

Studies on the absorption thermodynamic of clusters suggested that the [27] absorbate-cluster bond energies are significantly higher than in bulk materials, and , as a consequence, they decrease by increasing the particle dimensions.

Recently, an experimental procedure was developed, which combines thermodynamic measurements with reactivity and composition measurements at the saturation.

References

[1] Kreibig, U. and Vollmer, M., *Optical properties of metal clusters*, Springer-Verlag Berlin.

[2] Faraday, M., *Philos. Trans. Royal Soc. London*, (1857), **147**, 145.

[3] Bohren, C.F. and Huffman, D. R., *Absorption and Scattering of Light by Small Particles*, Wiley New York, (1998).

[4] Mie G., *Ann. Phys.*, (1908), **25**, 377.

[5] Compagnini, G.; Messina, E.; Puglisi, O. and Nicolosi, V., *Appl. Surf. Sci.*, (2007), **254**, 1007.

[6] Papavassiliou, G.C., *Prog. Solid State Chem.* , (1980), **12**, 185.

[7] Link, S. and El-Sayed, M. A., *J. Phys. Chem. B*, (1999), **103**, 8410

[8] Amendola V.; Polizzi, S. and Meneghetti, M., *J. Phys. Chem. B.*, (2006), **110**, 7232.

[9] Link, S.; Wang, Z.L. and El-Sayed, M. A., *J. Phys. Chem. B*, (1999), **103**, 3529.

[10] Compagnini, G.; Patanè, G.; D'Urso, L.; Puglisi, O.; Cataliotti, R.S. and Pignataro, B., *J. Phys. Chem. C.*; (2008), **112**, 20301.

[11] Cataliotti, R.S.; Compagnini, G.; Crisafulli, C.; Minicò S.; Pignataro, B., Sassi, P. And Scirè, S., *Surf. Sci.* , (2001), **494**, 75.

[12] Cataliotti, R.S., Compagnini, G.; Morresi, A.; Ombelli, M. and Sassi, P., *Phys. Chem. Chem. Phys.* (2002), **4**, 2774.

[13] Lamb, H., *Proc. London Math. Soc.*, (1882), **12**, 189.

[14] Duval, E.; Boukenter, A. and Champagnon, B., *Phys. Rev. Lett.*, (1986), **56**, 2052

[15] Montagna, M. and Dusi, R., *Phys. Rev. B.*, (1995), **52**, 10080.

[16] Fujii, M.; Nagareda, T.; Hayashi, S. and Yamamoto, K., *Phys. Rev. B*, (1991), **44**, 6243.

[17] Berne, B.J. and Pecora, R., *Dynamic Light Scattering* (1976).

[18] Palow, P., *Z. Phys. Chem.*, (1909), **65**,1.
[19] Couchman, P.R. and Ryan, C.L., *Phil. Mag. A*, (1978), **37**, 369.
[20] Matsubara, T. and Nataniski, A., *J. Phys. Soc. Japan.*, (1975), **39** 1415.
[21] Hoshino, K. and Shimamura S., *Phil Mag. A* , (1979), **40**, 137
[22] Wautelet, M., *Solid State Comm*., (1990), **74**,1237.
[23] Buffat, P. and Borel, J. P., *Phys Rev. A*, (1976), **13**, 2287.
[24] Zhao, S.J.; Wang, S.Q.; Cheng, D.Y. and Ye, H.Q., *J. Phys. Chem.,* (2001), **105**, 12857.
[25] Hayashi, C. and Oda, M., *J. Aerosol Science*, (1998), **29**, 757.
[26] Davis, S.C.; Klabunde, K.J., *Chem. Rev.*, (1982), **82**, 153
[27] Andres, R.P., *J. Mater. Res.* (1989),**4**.

2 SYNTHESIS

2.1 Fundamental aspect of PLAL

Pulsed Laser Ablation in Liquids (PLAL) has become a key method for synthesis of nanoparticles with controlled geometry and size. Pulsed laser ablation was first developed in the 1960s, shortly after the invention of the pulsed ruby laser. Since then, laser ablation in a vacuum or dilute gas has been studied by many researchers. By using different target materials and background gases, and varying parameters such as the laser wavelength, fluence, and pulse duration, it is possible to produce a wide variety of thin films. These include high temperature superconductors [1], metals, semiconductors, oxides, and other ceramics [2], and diamond-like carbon [3].

These studies clearly indicate that PLAL has become a successful material fabrication technique, allowing versatile design through choosing suitable solid targets and confining liquids.

Compared to the conventional physical methods (including chemical vapour deposition [4], vapour phase transport [5], and pulsed laser ablation in vacuum [6], and chemical methods (including hydrothermal methods [7], soft-template [8] and use of various surfactants [9,10]), the technique of PLAL has many distinct advantages.

These include (i) a chemically 'simple and clean' synthesis, the final product is usually obtained without by-products and no need for further purification; (ii) low cost of experimental setup and easily controlled parameters; (iii) the extreme confined conditions and induced high temperature, high pressure region favour the formation of unusual metastable phases.

In experiments of pulsed laser ablation of solid materials, submerged in liquid environments (PLAL), colloidal suspensions of objects at a nanometer-size scale are obtained. The nature of these nanoparticles and the characteristics of the plasma plume that is surrounding the struck point of the solid target, present a strong dependence on the experimental conditions and diverse a clear description in their physical implications.

This because it is possible to modulate the shape and the size of the ablated materials, only acting with the pulsed laser beam and regulating its fluence, i.e. the amount of energy of the laser electromagnetic field releaser on the target, expressed in J/cm^2 of surface [11].

In our laboratory, the PLAL technique is commonly carried out with the aim of obtaining nanometer-sized metal particles, which are ideal supports for SERS measurement [12].

In fig. 2.1 the simple set-up we used to perform PLAL experiments in shown. Briefly, it consist of a pulsed laser source, which is a Nd-YAG by Continuum, model Surrelite II, operating at 1064 nm in the first harmonics and 532 nm in the second harmonics.

The laser beam has been focused on the target by a lens of 250 nm focal length and the target was submerged in the liquid medium.

Typical irradiation conditions has been: pulsed repetition was set at 10 Hz with 3 ns pulse duration; the irradiation period has been protracted for twenty min.

The laser spot size on the surface has been varied in the range 1-3 mm of diameter to get always as energy density on the target fluence of around 2 J/cm^2.

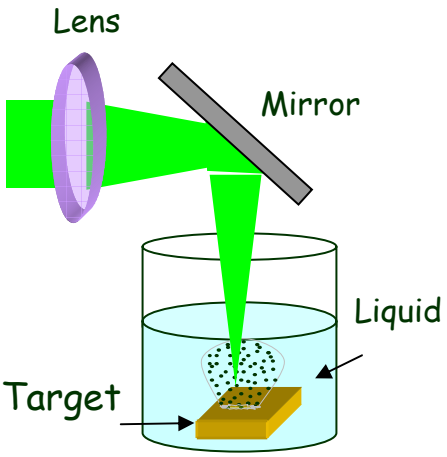

Fig.2.1: A block scheme of the set-up used in our experiments to produce nanoparticles in liquid media. The irradiation condition are described in the text.

It was observed that, when we varied the asset of experiments by suspending vertically the target in the liquid medium, instead to put it in the vessel bottom, and irradiate sending the laser beam at 90 degrees to sample, a clear double layer having particles suspended on the top was observed in the irradiated zone only.

This phenomena was more clearly visible with gold that with silver, due to intense red colour of gold colloids. Suspending the irradiation and allowing the system to restore equilibrium conditions, diffusion of Brownian particles in the whole submerging fluid was observed in a few minutes.[13]

During a irradiation a typical plasma plume was observed and its appearance is that shown in Fig. 2.2.

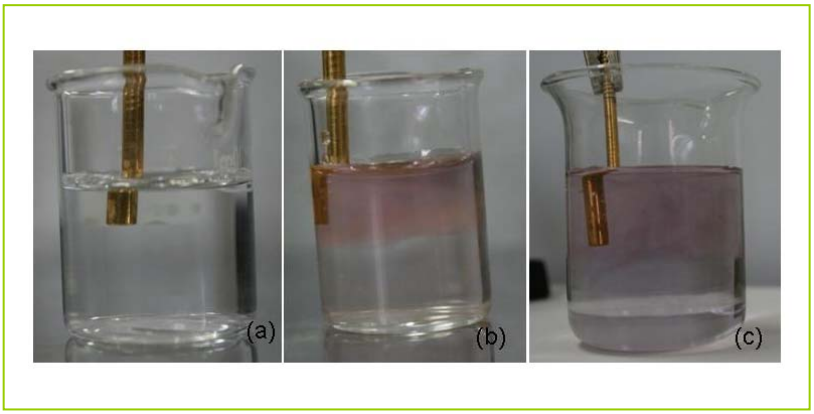

Fig.2.2: Laser ablation of a noble metal target vertically submerged in liquid water and ablated by a pulsed laser beam impinging at 90 degrees.

The strong luminosity is due to electromagnetic radiation emission by the ionic states of metal atoms in the plasma. At the end of irradiation, we observed a coloured colloidal suspension of gold or silver in water, that appeared red or yellow, respectively. The aqueous suspension was transparent and just ready for optical measurements in the visible spectral region.

Analysis of the plasma plume was performed observing the propagation of sound waves in the liquid confined region around the struck point, whereas the shock waves in the solid target were studied at the light of Courant [14] and Cole [15] treatments, that consider the failure of the Navier-Stokes equations to treat this matter.

Fig.2.3: A 1000 times magnification of the plasma plume generated in water by pulsed ablation of solid noble metal targets.

When a laser ablation experiment is carried out in a liquid medium, the confinement action operated by the liquid in which the ablated solid target is submerged determines the formation of a shock wave in the plasma plume [16-18]. The laser produced plasma tends to expand at a supersonic velocity, but this expansion creates the shock waves because the liquid confines the expansion itself. The laser energy of pulses, impinging on the solid target, produced a continuous supply of ablated material in the plume; this is the source of the plasma intense luminosity. In fact, the vaporizing species are highly excited ionic particles, that incoherently relax towards fundamental quantum states emitting electromagnetic radiations. The emission process is however different from that occurring in a LASER resonator, since the light emission from the plume is spontaneous and it is not coherently stimulated as in the

laser effect. As shown in fig. 2.3, the plasma appears strongly illuminated due to these incoherent emission processes.

Thermodynamic and kinetic factors may influence the formation of different phases due to the evolution of the laser-induced plasma. As reported by Yang [19], three are the thermodynamic factor which are of importance in determining the nature of phases in the plasma. There are: density of ablated species, temperature and pressure in the plasma.

The first parameter, *i.e.* the density of ablated species, may be evaluated by measurements of the expansion volume of the plasma plume itself. In practice, this expansion volume and the amount of the ablated species here contained, is measured trough the volume of the hole which remains on the target surface after the ablation.

As shown in fig. 2.4, taken form Yang's review [19], the expansion volume of the plasma is measured through the images of the light emitting region on the surface. In this case the image refers to a graphite target submerged in water [20]. In such an experiment, the volume of the plasma plume, being a hemisphere of diameter corresponding to the FWHM intensity of emitted light, is estimated as $9.9\times10^{-7}cm^3$.

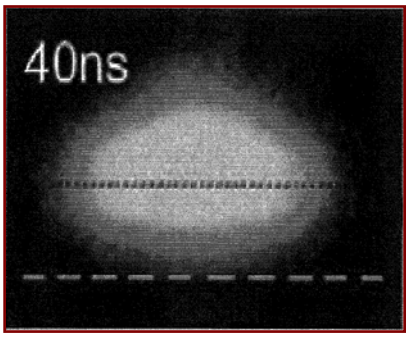

Fig. 2.4: Image (taken from ref.[20]) of the expansion volume of the plasma plume in the graphite ablation in water, whit laser pulses having 40ns pulse duration.

Assuming that the hole volume on the surface of target is linearly increased by a number pulses, the ablation volume for a single pulse is determined to be $7.4\times10^{-8}cm^3$. Therefore, the density in the plasma plume of carbon species, coming form graphite ablated with pulses of a Nd-YAG laser, resulted $6.7\times10^{21}cm^{-3}$.

The second thermodynamic parameter is the extra temperature of the plasma plume. This is measured, as in a pyrometer, through the optical emission spectra of the ablated species form the plasma confined in the liquid medium. Again, using a graphite target as ablation source, a plume temperature of ca. 5000 K has been determined when the optical emission spectra of C_2 molecules as measured. These species were obtained in water, ablating the target with a Nd-YAG laser at 1064nm, and pulses having 20ns duration and energy fluence of 10 J/cm^2 [20].

Finally we must talk of the third parameter, *i.e.* pressure. By conducting in the liquid state the ablation of a solid target with a pulsed laser, this parameter depends on the sum of two contributions.

The first one is the adiabatic expansion of the plasma under the confined action of the liquid. In this medium an acoustic wave propagates longitudinally under the action of the expanding plasma, whilst a shock wave will propagate in the bulk of the solid target. Such situation is schematically depicted in fig. 2.5, taken from ref. [19]. Thus, the shock wave inside the solid target is the origin of the second contribution to the extra pressure generated in the system, when the plume is obtained for the ablation in a liquid. Many experimental techniques have been developed, especially by Fabbro and co-workers [21-26], to measure the pressure generated by the shock wave propagating inside the solid target.

These experiments were also accompanied by the development of theoretical models for the extra pressure due to the shock waves, done by the same author and his school.

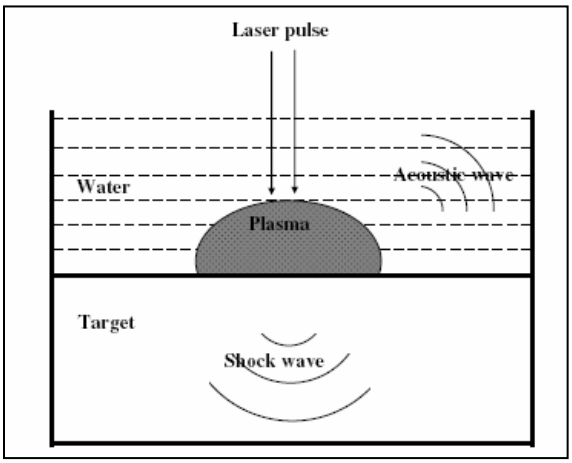

Fig.2.5: A scheme (taken from ref. [20]) showing the acoustic waves propagation in the confining liquid (water, and the shock waves generation inside the solid target.

The shock wave induce in the plasma plume extra conditions of pressure, temperature and density. As to the pressure increase, for instance, Berthe [25] reported a pressure of 2-2.5 GPa, when pulses of 50 ns form the wavelength 0.308 μm of a XeCl excimer laser were employed. With shorter pulse durations, as for instance 3 ns, pressure up to 10 GPa have been reported. Concerning density and temperature values, densities up to 1022-1023 atom/cm^3 have been reported for the ablated species in the plasma, and the plume temperature reaches values of 4000-5000 K [20].
From Fabbro's studies [21-26], a relationship for the extra pressure in the plasma can be given as

$$P(GPa) = 0.01\sqrt{\frac{\alpha}{\alpha+3}}\sqrt{Z(gcm^{-2}s^{-1}\sqrt{I_0(GWcm^{-2}),}}$$

α being the internal energy fraction which is of thermal nature (α ~ 0.25), I_0 the intensity of incident power, and Z the reduced shock impedance between the confining liquid medium and the solid target. In the case of water as liquid medium, Z is defined by the formula

$$2/Z = 1/Z_{water} + 1/Z_{target}$$

To give an exemplum of the Z values [21-26], for aluminium and silicon targets, ablated in water as submerging medium, these are:
$Z_{water} = 0.165 \times 10^6$, and $Z_{silicon} = 2.1 \times 10^6$, being the units g $cm^{-2}s^{-1}$.
In our case, the corresponding values have been measured to be $Z_{gold} = 1.96 \times 10^6$, and $Z_{silver} = 1.33 \times 10^6$ g $cm^{-2}s^{-1}$, respectively.
With these values of Z, and assuming for α the value 0.25, pressures in the range 2.8-5.2 Gpa were obtained as a function of our I_0 values. It must be noted that the plasma state is very far from the thermodynamic equilibrium, so tat the application of any type of state equation to evaluate the real pressure form the temperature value is not possible. For instance, if one would assume the plasma state as an ideal gas in thermodynamic equilibrium and would apply the relevant state equation

$$P = nN_a K_B T / V$$

N_a and K_B being the Avogadro and Boltzmann constants, respectively, the estimated pressure by such equation will result much lower than the measured in the plasma plume in experiments of pulsed laser ablation in liquids.
Under equilibrium conditions, the propagation velocity may be expressed with the formula

$$c = \sqrt{\left(\frac{\partial p}{\partial \rho}\right)_S} = \sqrt{\gamma \left(\frac{\partial p}{\partial \rho}\right)_T}.$$

The quantity *c* is a thermodynamic property of the system and constitutes the speed of propagation of the sound waves. In the perfect gas approximation

$$c = \sqrt{\gamma \frac{p}{\rho}} = \sqrt{\gamma k T / m}$$

being

$$\gamma = C_p / C_v = 1 + R/C_v$$

The linearised equation of motion becomes

$$\frac{\partial v}{\partial t} + \frac{c^2}{\rho_0} \frac{\partial \rho}{\partial r} = 0.$$

Introducing the continuity equation , where the term (υ·δρ/δr) is a very small quantity of the second order, we get the *linearized equation of continuity* in the form [27]

$$\frac{\partial \rho}{\partial t} + \rho_0 \left(\frac{\partial}{\partial r} \cdot v\right) = 0.$$

Regarding the kinetic aspects, there are some peculiarities of PLA in liquid confined targets. Surprisingly, the velocity of ablation of a solid target submerged in a liquid medium is much higher than the corresponding velocity in vacuum or in a diluted inert gas. In fact, due to the confining action operated by the submerging liquid , the plasma having the above said characteristics of high temperature, pressure, and density, can continuously etch the solid target at the interface solid-plasma, not expanding very fat from the etched target as happens in the vacuum, or in diluted gas environments [19] .

In fig. 2.6 we show the effect of laser ablation of a silicon target with an UV laser, having pulses in the range of 20-30 ns, when two different confining media, *i.e.* water and air, are submerging the target [28-31].

It is also shown as the thickness of the submerging water has a maximum efficiency at a definite depth, but it decays more than linearly when the thickness of submerging layer overcomes a certain value.

Although the layer thickness of the submerging liquid is very important for the mechanisms of energy dissipation, the maximum observed at a certain value of thickness in the plot ablation rate *vs.* layer thickness (Fig.2.6 b) may be explained with the minor possibility given to the plasma plume to expand when the layer of the submerging medium is less. Therefore, a more confined plasma, around the etched point in the target, will concentrate better the energy due to the high temperature and high pressure of the plume, to promote more easy etching of the solid sample.

The mechanism seems to be controlled by the shock waves generated in the target under the laser pulses having an opportune fluency, because they decay into acoustic mechanical waves in the liquid medium that are called *ablative piston*. The action exerted by the *ablative piston* enhances

that one due to extra pressure and high temperature of the plume increasing the ablation rate.

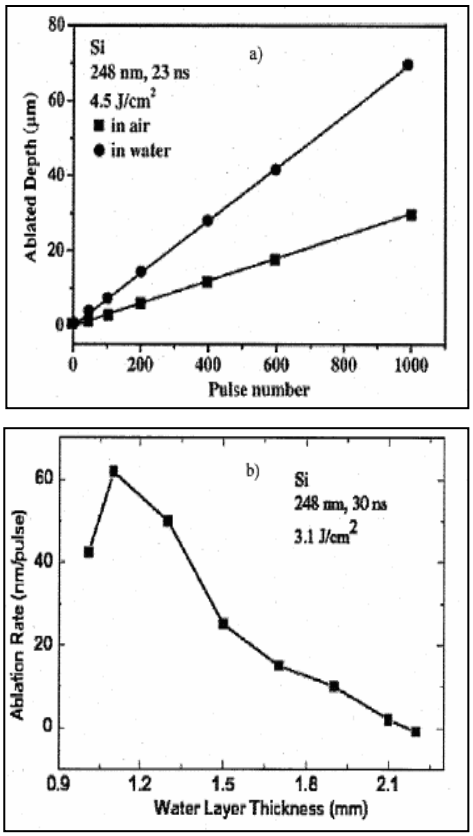

Fig.2.6: The effects, on the ablated particle amounts, of different confining media(a) and of the layer thickness (b) in PLAL experiments.

Because the confining liquid absorbs the laser energy in the beam crossed layer [13], the etching action by the plasma plume and the depth of the liquid layer must reach a right compromise. The absorption of the laser beam energy by the submerging liquid produces so high temperature

increase in the crossed layer, that the density of heated portion of liquid may be strongly modified respect to the equilibrium value [11], especially if the density *vs.* temperature curve of the relevant submerging liquid has a great slope.

On the other side, the depth of the liquid layer can reduce the ablation threshold of the solid target surface and the dissipation of the plasma temperature at the plasma-liquid interface. In conclusion, high production of ablated particles by PLAL in confining liquid media is possible either for thin films deposition that for small particles synthesis [19].

An important kinetic aspect of PLAL in liquid media is the rapid dissipation of the plasma plume energy at the boundary on the confining liquid. Such a quenching action determines, from one side, the possibility to repetitive shoot on the surface target by the pulsed laser beam and this fact increases the amount of produced ablated species, but, from another site, determines the heating of the layer strictly in contact with the plume and crossed by the laser beam; we noticed that this fact affects the density variations such layer [13]. The rapid quenching action operated by the presence of liquid medium can be seen in fig. 2.7, taken from ref. [19].

Here the plasma light emission in water, of a solid graphite target is generated in PLAL experiments with different pulse duration.

One can see, from the dimension of emitting plume volume, that with longer duration of pulse, the confining action of the liquid in dissipating the energy of system is more efficient.

In fact, in the case of liquid confined plasma, the plume is confined near to the target surface, thus providing a continuous supplying of ablated material which , in state of plasma , enforces the luminosity of the emission [19].

Finally, the cooling effect operated by the liquid confining medium should enhance the formation in the plasma plume of metastable structures and phases.

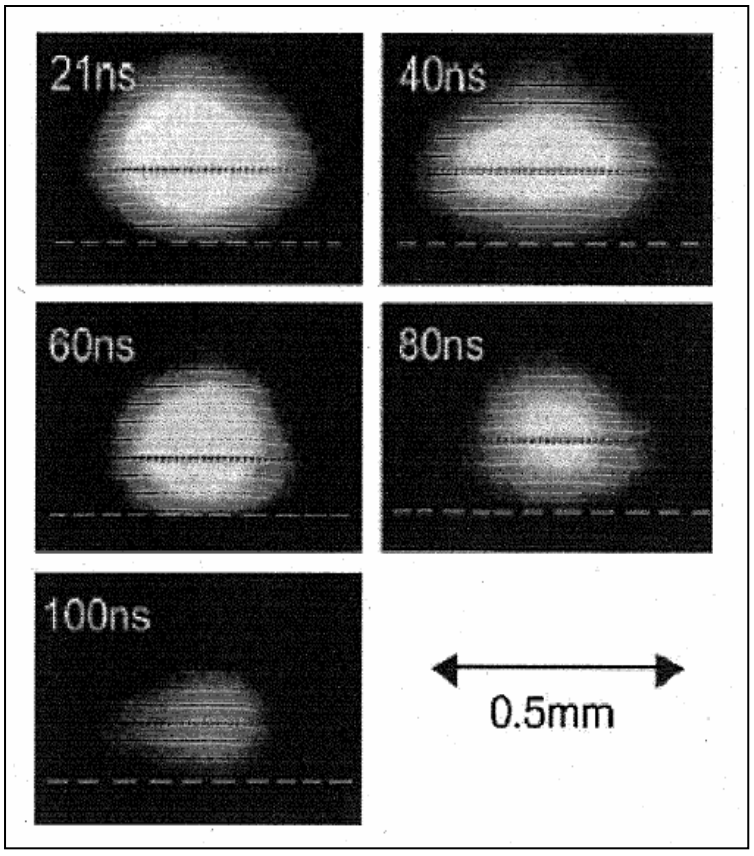

Fig.2.7: Influence, on the expansion volume of the plasma plume. Of the laser pulses duration (taken from ref.[20])

There rapidly convert to the stable phases due to the short quenching times that the confining liquid exerts at the plasma-liquid interface. These metastable phases are the results of the reactions occurring inside the

plasma and at the plasma-liquid interface due to the high temperature and high pressure conditions.

In fig. 2.8, a series of chemical reactions between B (solvent) and A(solid target, and among their ions, are schematically reported. Of course, changing either A or B, these reactions will strongly change, also because the possibility of having ionic species in the plume and at the interface depends on the ionisation energies of the relevant species. In our laboratory, it has been shown that the nature of ablated species coming from the same target will change in different liquid media [33]. The plasmonic resonance spectra, have been used to reveal these differences, depending on the used solvent.

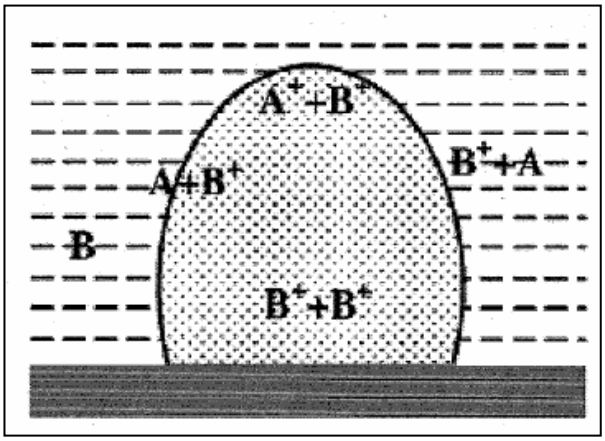

Fig. 2.8: A scheme showing the chemical reactions occurring between solute (A), solvent (B) and among their ions, inside the plasma plume and at the plume-solvent interface.

Of course, a compressed treatment like this, does not allow to speak of many other physical aspect that are important in plasma states. There are,

for instance, the role played by the discontinuities in the distribution function of plasma electrons, and as these discontinuities can be modelled with approaches deriving from the continua mechanics.

Moreover, it should be important to introduce the effect of the electric fields inside the plasma due to the plasma electrons and to the ions, on the mechanical waves propagating in the plasma plume. The effect is in practice a wave-breaking one, when the intensity of the electric field inside the plasma plume overcomes certain critical values.

Shifting again our attention on the shock waves, we want to describe the hydrodynamic processes accompanying the waves propagation[27].

First of all, we will define a shock wave a system in which the properties of a fluid phase change sharply within a very short distance in the space. There is in the gas phase, a certain tendency of any compression-wave to transform into a shock wave.

Neglecting in the hydrodynamic equations terms involving thermal conductivity, diffusion, and viscosity, the shock wave manifests itself as a mathematical discontinuity in the solutions.

However, including these dissipative term, the effect is that to change the discontinuity in a transition slightly more gradual, which for instance, in a gas at TPS conditions, occur within a distance of few mean free paths, *i.e.* approximately within 10^{-5} cm [27].

Due such sharp gradients in the macroscopic properties o a gas subjected to a shock wave, the Navier-Stokes equations are not sufficiently accurate to describe both structure and thickness of a wave.

We tried to apply at our system of plasma plume the *Hugoniot equation* for a steady-state one-dimensional problem [14-15]. Assuming that the derivates at $x = -\infty$ are zero, we obtain the relations below between the variables in the two sides of the shock wave:

$M = \rho_0 v_0 = \rho_\infty v_\infty$,
$M v_0 + p_0 = M v_\infty + p_\infty$,
$H_0 + (1/2) v_0^2 = H_\infty + (1/2) v_\infty^2$

These relations, called *Hugoniot equation*, correlate the eight quantities ρ_0, v_0, p_0, H_0, ρ_∞, v_∞, p_∞ *and* H_∞. However, using the thermodynamic dependence of H on ρ and p, the number of variable is reduced to six [27]. Thus, the equations are sufficient to express three of the variables in terms of the remaining three. Usually, we will specify the density and pressure on the low pressure side of the shock wave, ρ_0 and p_0, together with an additional parameter which indicates the strength of shock, for instance the pressure in the high side, p_∞ . The v_0 value represents the velocity of propagation of the shock wave into the expanding plasma, on the low pressure side. v_∞ is instead the velocity of hot gases away from the wave front of the plasma.
We rearranged the *Hugoniot equation* in a different form, and from the equation continuity and motion we obtained

$$M = \left(\rho_0 \rho_\infty \frac{p_\infty - p_0}{\rho_\infty - \rho_0} \right)^{1/2}$$

Moreover, because ½ (v_∞^2 - v_0^2) = ½ (v_∞ - v_0) (v_∞ + v_0), using the same couple of equations, we may obtain [28]:

$$1/2(v_\infty{}^2 - v_0{}^2) = -\frac{(p_\infty - p_0)(\rho_\infty + \rho_0)}{2\rho_\infty \rho_0}$$

Now, combining this result with the conservation of energy equation and using the relation $H = U + \rho/p$ we have got the relation

$$(U_\infty - U_0) = \frac{(p_\infty + p_0)(\rho_\infty - \rho_0)}{2\rho_0\rho_\infty}.$$

This equations can be considered the *Hugoniot equations* in a more convenient form.

As we cannot solve explicitly these equations, we have introduced the equation of the state and the thermodynamic condition for the gas in the plasma plume. These are of course large but necessary approximations, and allowed us to calculate values of pressure in the plasma going from ca. 2.8 GPa to ca. GPa, depending on the laser energy we released over the target, whilst the temperature was estimated by the plume luminosity to be around 4200K. With the same above equations and the ideal gas approximations, we obtained energy values of the order of 2.5 J in the plasma, values that are well above those of the impinging pulses of the laser. Therefore, the role played by the energetic of chemical reactions in the plume, and at confining liquid-plume interface, to enhance the energy well above the threshold given by the laser pulses is undoubtedly dominant.

2.2 PLAL of silver nanoparticles

Shape control of metal nanoparticles has received considerable attention in recent years because of the strong correlation between the shape and the chemical, physical, electronic, optical, magnetic and catalytic properties of a nanoparticle.

Wet chemical methods are widely accepted as practical and versatile approaches that produce nanoparticles in cube[34] rod [35] triangular[36] and wire[37] shapes. However, very few of them have been successful in controlling simultaneously both the size and shape of the products.

Photochemical methods have provided alternative approaches to modulate the size and shape of the nanoparticles synchronously. In recent years, numerous reports have focused on photoinduced or laser-induced growth of nanoparticles with definite shape and size.

Zheng et al, observed that the photoinduced method can be used for converting large quantities o silver nanospheres into triangular nanoprisms [36].

Lombardi et al [38] present a method for the tunable production of monodisperse silver nanoparticles. Using monochromatic light of different laser wavelengths to irradiate an initial solution of seed crystals, the size and shape of the products can be controlled.

Trace quantities of Au and Ag nanoprism have been observed as by products of method that predominately produce spheres [39].

In the last few years the growing interest for “plasmonics”, even due to the possibility to produce surfactant-free nanoparticles by pulsed laser ablation in liquid [40] has led to the development of new “nano-photonic” concepts with applications in extremely advanced fields [41].

Interesting studies on the surface chemistry of surfactant-free noble metal nanoparticle obtained by PLAL was reported by Sylvestre et al[42] and Muto et al[43]. Metal nanoparticles produced by PLAL present negative charges on the surface, that stabilize the colloidal solution due to the presence of electrostatic repulsion forces, and therefore do not require the addition of stabilizers or binders in order to control aggregation process.

It was demonstrated that the negative charge is induced by the presence of oxidized metal atoms on the surface nanoparticle. Furthermore, several studies conducted by Liao et al.[44] associated aggregation phenomena of noble metal nanoparticles in water to strong dipole/dipole interactions generated by an asymmetric charge distribution onto the cluster surface.

Changes in the surface charge state and therefore on aggregation phenomena can be photo-induced by laser irradiation at different wavelengths.

Therefore, silver colloidal sols were prepared using laser ablation in water. A Nd:YAG laser beam was focused through a lens on a pure metal target submerged in Millipore grade water (5 mL). Both the first (1064 nm) and the second harmonic (532 nm) wavelengths have been used. The laser (Surelite II model by Continuum) has a pulse duration of 5 ns and a repetition rate of 10 Hz. Plasma (plume) generated by the beam- target interaction generally contains ablated species as well as ions and radicals coming from the water [45].

Synthesis and properties of silver colloids have already been investigated through spectroscopic and microscopic techniques.

Each colloidal system have been immediately characterized by performing Uv-Vis extinction spectra using a Perkin Elmer Lambda 2 spectrometer in the range 300-1100 nm.

It is well known that, among the most important features of metal nanoparticles, optical properties play a dominant role. Absorption spectra of silver colloidal dispersions exhibit broad bands in the UV–Vis range due to the excitation of plasma resonances and interband transitions. The existence of a plasmon resonance associated to the nanosized nature and spherical shape of the metal is confirmed by the presence of a peak at about 400 nm, while the interband transitions from the filled d band to the Fermi level is detected in the UV–Vis spectrum in the range from 200 to 350 nm.

The extinction of each colloid has been monitored for a few days and in this time interval the sol seems to be stable and does not show any tendency towards aggregation.

Dynamic Light Scattering (DLS) has been employed to obtain an 'in liquid' size distribution of the obtained particles by using a Horiba LB-550 system. Some drops of each colloid have also been deposited onto a single crystalline silicon substrate in order to perform SEM analyses using a ZEISS SUPRA 35 FE-SEM system with a field emission electron gun, while copper grids have been used to obtain TEM images using a JEM 2010F JEOL microscope.

The same procedure has been used to deposit some particles onto a silicon substrate for XPS measurements.

These were obtained using an AXIS-ULTRA spectrometer with a basic pressure in the range of 10-9 Torr. The X-ray radiation was generated by an Al Kα line decay (1486 eV) at operating conditions of 10 KV and 15 mA. The emitted photoelectrons were analyzed with a hemispherical electron energy analyzer. The detailed spectra have been acquired with a resolution below 1 eV.

A first attempt to determine the size distribution of the produced nanoparticles has been done by using dynamic light scattering (Fig. 2.9).

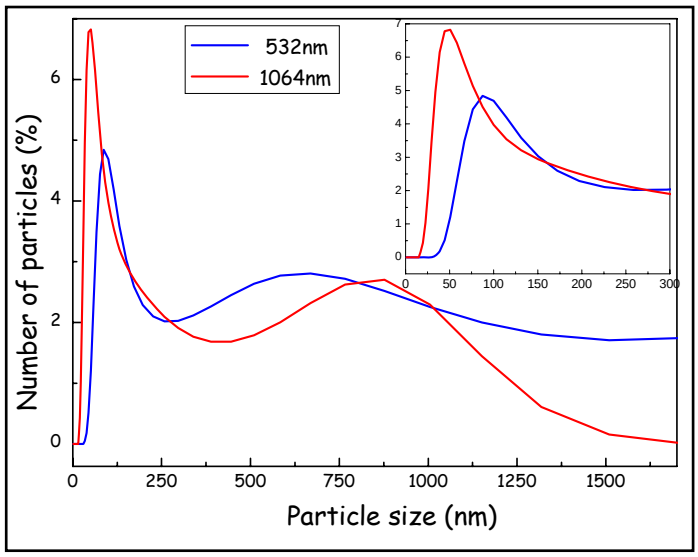

Fig. 2.9: DLS of silver nanoparticles produced by laser ablation in water using both 1064 nm and 532 nm irradiation wavelengths.

The technique exploits the Brownian motion of the particles which causes a Doppler shift in the incident light frequency.

The amount of frequency shift is related to the frequency of the Brownian motion, which is related to the size of the particles. In the case of silver sols obtained by using 532 and 1064 radiations the size distribution as obtained by DLS is reported in Figure 2.8.

It is straightforward to observe two well separated components at sizes (diameters) of few tens and few hundreds of nanometers. The inset shows a zoom of the size distribution in the range 0-200 nm in which it is clear that that infrared radiation is able to produce smaller particles (20-50 nm), while the ablation performed at 532 nm gives clusters with sizes extending up to 100-120 nm.

The first part of the size distribution is generally attributed to the presence of almost spherical metal nanoparticles which are produced by nucleation during the plasma plume cooling followed by nuclei growth and coalescence.
Three experimental findings support this observation.

- First, transmission electron microscopy (TEM) and UV-Vis analysis evidenced the polycrystalline structure of the silver nanoparticles obtained by PLA as reported in Figure 2.10.
- Second, nanoparticles obtained by LP-PLA in the presence of ligands or stabilizing agents have a smaller average size with respect to particles obtained in pure solvents[46].
- Third, LP-PLA in reactive solvents did not originate pure metal nanoparticles. [47]

As a matter of fact the driving force for the nucleation of metal embryos in the plasma plume is the supersaturation, given by the ratio between the actual vapour pressure to the equilibrium vapour pressure at the system temperature. The nucleation process is fast and is followed by a diffusion limited growth process of the nuclei, which continues for hundreds of nanoseconds after the laser pulse.
During the growth, free metal atoms condense on nuclei which can also coalesce together, originating the typical polycrystalline structure of the metallic nanoparticles. Mafunè and co workers observed that the growth of ligand-free nanoparticles can continue for several days after the synthesis, because metal ions can last in solution for a long time after the formation of the plasma plume in the case of high affinity with the solvent, as for Pt^{+} and Ag^{+} in water[46].

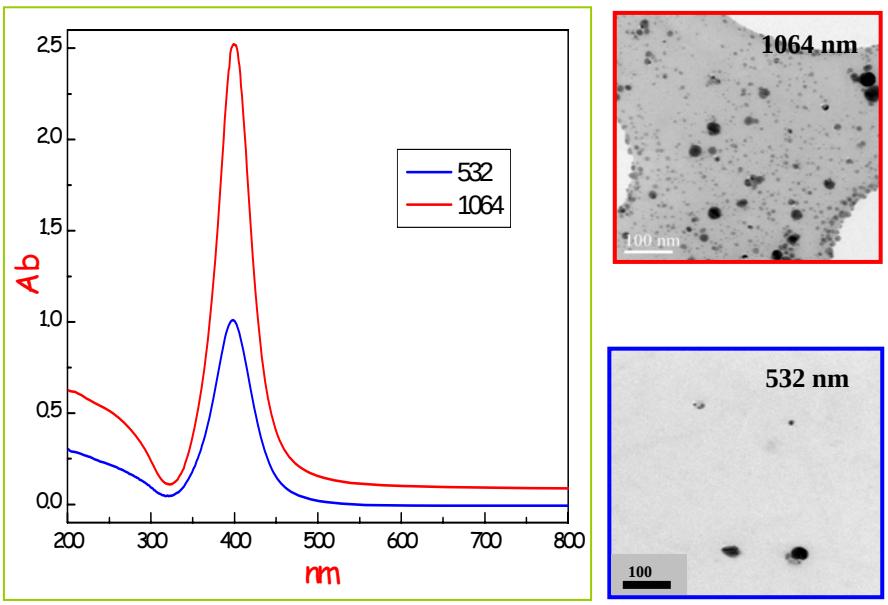

Fig. 2.10: Uv-Vis spectra (on the left) and TEM images (on the right) of silver nanoparticles prepared by two different irradiation wavelengths.

The origin and the specific nature of the larger particles observed in the size distribution of Figure 2.9 is much more intriguing and need a specific investigation.

For this reason we performed a series of SEM analysis on both filtered and unfiltered solutions. Filtering has been done by using 200 nm pore size filters in order to separate the two distributions. Figure 2.11 shows the results of such an analysis.

In particular Figure 2.11a reports a plenty of spherical like silver particles after filtering which represents the low size distribution already discussed, while Figure 2.11b and c (large size distribution) give a clear

indication of the clusters obtained after the ablation with 1064 and 532 nm radiation respectively.

The nature of the micrometer sized silver aggregate is now clear. They consist in well defined regular solids, namely cubes in the case of the ablation at 532 nm and octahedra when 1064 nm radiation is used. The faces of these silver nanosolids are smooth and their average length varies between 200 and 500 nm. The images also evidences that the corners and edges of some particles are truncated.

Several previous paper have accounted for the formation and size control of silver nanoparticles with well defined shapes.

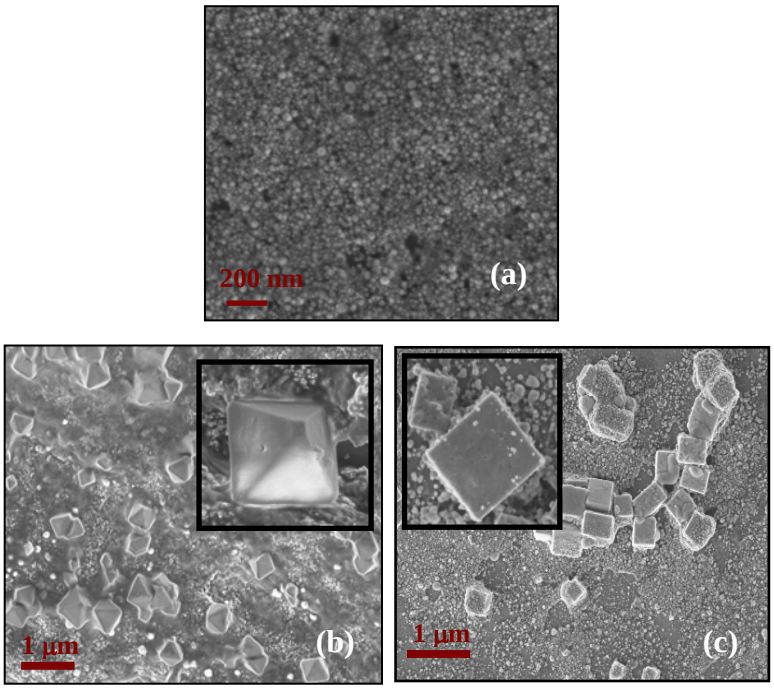

Fig. 2.11: SEM images of silver nanoparticles

Two approaches are generally followed. In the first case chemical effects, like polymer mediated processes or the presence of halide ions, have been proposed during a classical reduction of $AgNO_3$[48].

A second approach has been considered with the so called photoinduced nanoparticles conversion[47]. In this case nanoseeds in the growth solution undergo a photochemical rearrangement to give birth to spherical nanoparticles of smaller and uniform size, while in a following step, the growth process moves into coalescence, where the newly formed nanoseeds aggregate to form rudimentary species which generally consists of silver platelets. The platelets then could evolve towards more complex structures depending on the irradiation wavelength as demonstrated by the already reported micrographs.

In our study we have conducted all experiments in pure water thus we can exclude any chemical effect.

On the contrary it is obvious to consider that the silver particles, which are initially produced during the ablation, are continuously irradiated by the laser beam itself during the overall process. This means that the effect of the laser beam is twofold. First the ablation produces spherical clusters, slightly different in size if infrared or visible radiations are used. These seeds are further induced to grow once the initial colloidal suspension continues to be irradiated.

In this regard, we performed some XPS analysis on the as-produced silver clusters deposited on silicon substrates.

It is well known that the sampling depth of XPS is a few angstrom. Considering that the particles size is about 10-20 nm, then we obtain information confined to few atomic layers around nanoparticles. Moreover the binding energies and line widths determined by XPS are strongly influenced by the nanometric size. In order to detect differences in the chemical state, Ag 3d core level spectra have been analyzed for the

two Ag systems and reported in figure 2.12. XPS analysis clearly indicate that the Ag_3d binding energies of Ag@532 aggregates (dashed line) are located at lower (0.93 eV) energy respect to the Ag@1064 peaks (solid line).

This is one indication that oxidized silver atoms (AgO and/or Ag_2O) are present on the at Ag@532 nm cluster surface.

These species are probably formed during or immediately after the nanoparticles formation. In the case of Ag@1064nm the amount of oxide is negligible and the surface can be considered "metallic".

Figure 2.12 also shows the position of metallic silver and the increase of the line width for the oxide signal, in agreement with literature data in which AgO is considered a mixed oxide with the presence of both Ag^+ and Ag^{3+} ions [49].

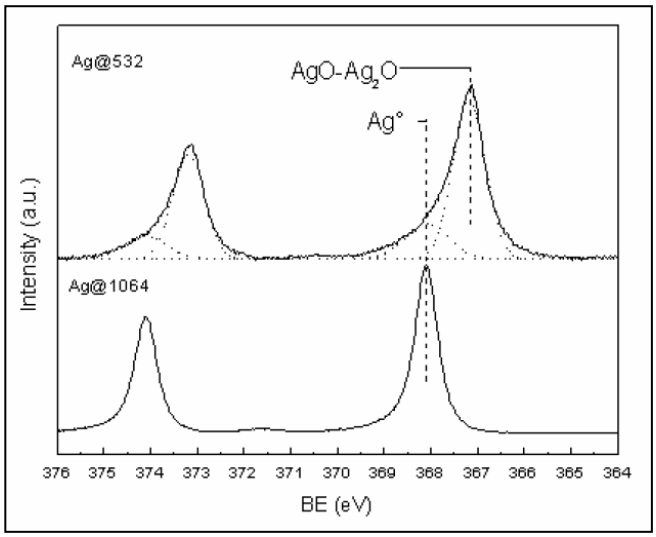

Fig.2.12: XPS spectra of Ag@532 nm nanoparticle(upper part of the figure) and Ag@1064 nm nanoparticles (lower part of the figure).

In view of XPS results we suggest that during laser ablation the Ag clusters are partially oxidized forming an Ag_2O layer on the surface.
Indeed, Yan an co-workers [50] reported a laser-based approach to fabricate Ag-Ag_2O micro-cubes, octahedral and truncated octahedra directly from bulk Ag in polysorbate 80 aqueous solution at room temperature.
So, Yan results are further confirmation of what suppose by XPS analysis.
Additional confirmation can be explaining by the different interaction with LCCs. The two as prepared silver colloids (solid lines in figure 2.13) show a moderate difference in the SPR signal and position and width seem to be not influenced by the laser wavelength used for the ablation.
It is to be observed that while at 1064 nm the pulsed beam do not interact with already formed particles in water (at this wavelength the light absorption is negligible), the radiation at 532 nm can be considered partially in overlap with the tail of the plasmonic signal thus locally increasing the colloidal temperature [51].
Once LCCs solution is added, the two colloidal suspensions behave in a deeply different way.
Slight variations were detected in the SPR for LCC-Ag@ 532nm samples; after the interaction a red shift of 14 nm and a certain increase of the signal width is observed and it was already associated to aggregation phenomena [52].
On the contrary in LCCs-Ag@1064nm samples a second plasmon component appears at about 713 nm, while the component at lower wavelength remains positioned at about 416 nm.
Several works reported in literature [53] explain the split of SPR ($\lambda - \lambda_0$) as indicative of a plasmon coupling among metal nanoparticles.

An exponential decay is reported as function of the distance (g) between two interacting nanoparticles of diameter D.

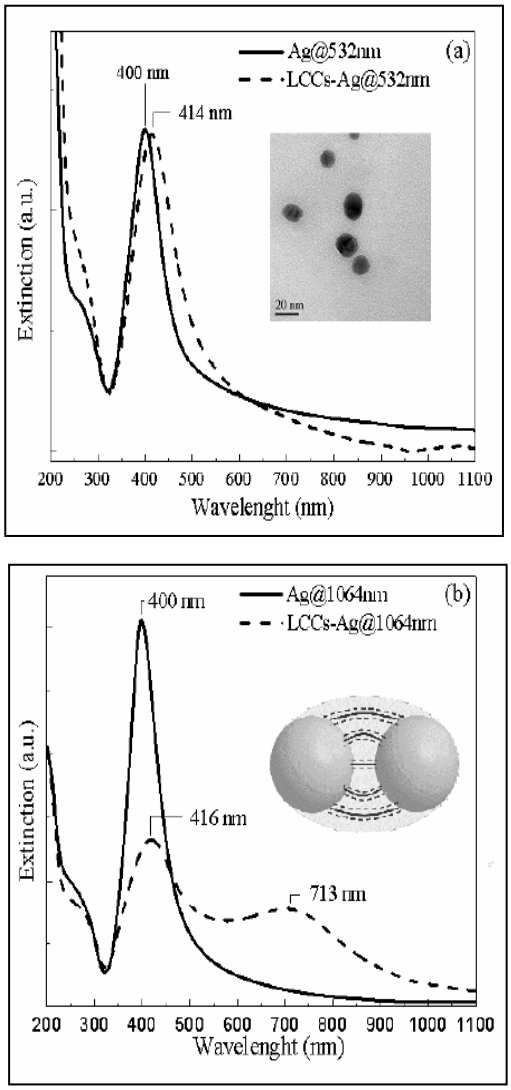

Fig. 2.13: shows extinction spectra in the surface plasmon resonances (SPR) region for either silver colloidal sols prepared by ablation at 532 (Ag@532nm) (a) and 1064 (Ag@1064nm) (b) before and after the interaction with LCCs.

The so called plasmon ruler equation is reported below:

$$\frac{\lambda - \lambda_0}{\lambda_0} = 0.18 \exp^{\left(\frac{-(g/D)}{0.23}\right)}$$

It is also useful to define σ as the *g/D* ratio. This mathematical model is based on a simple dipole dipole coupling approximation and is roughly valid for all kinds of metals.

In our case, if we suppose that the average silver cluster diameter is 15 nm (see TEM image in the inset of figure 2.13a) and the average carbon chain length is 1.19 nm (corresponding to 8 carbon atoms/chain, detectable by SERS studies, as reported [54]), the value of σ should result far below 1.05, consistently with the presence of two different contributions. Moreover carbon chains present an extended π electron system, so they could act as linkers between nanoparticles, and the conjugation of their electron could lead to the plasmon coupling between single nanoparticles as schematically depicted in figure 2.13b as an inset. As previously mentioned marked differences in the as prepared silver nanoparticles features should be observed when different ablation wavelengths are used.

In view of XPS results we suggest that the oxide layer block the chemisorptions of LCCs thus preventing the phonon coupling. Moreover the oxide layer also inhibit the coalescence of the silver clusters. This is an important result because it has been demonstrated that the wavelenght of laser source can influence either the size of nanoparticles [55] and their surface chemistry. At this stage we can suppose that LCCs-Ag@1064nm present a structure in which carbon chains bridge among metallic nanoparticles, so explaining the plasmon coupling effect while,

in the case of Ag@532nm, LCCs tend to self-assemble around aggregated nanoparticles. Further structural analysis are in progress.

2.3 PLAL of gold nanoparticles

Gold nanoparticles are widely studied for their properties, which find application in many different fields, from material to medical science [56]. A key factor in the progress of this research area is the easy availability of AuNP with controlled size and shape [57], which can be obtained with appropriate synthesis methodologies.

The intense research in this field is also motivated by the search for new multifunctional materials that will allow designing of the modern miniature electronic and optical devices for ultra fast data communication and optical data storage.

One of the way to obtain contaminant free metallic nanostructures, including metallic colloids in a reproducible and environmental sustainable fashion is laser ablation of bulk targets in liquid media.

Similarly to silver nanoparticles PLAL of stable gold nanoparticles in pure water is possible without using reducing agent or stabilizing molecules.

Therefore, gold colloidal sols were prepared using laser ablation in water. A Nd:YAG laser beam was focused through a lens on a pure metal target submerged in Millipore grade water (5 mL). Both the first (1064 nm) and the second harmonic (532 nm) wavelengths have been used. The laser (Surelite II model by Continuum) has a pulse duration of 5 ns and a repetition rate of 10 Hz.

Shape and size information on clusters in a liquid dispersion can be generally achieved through a series of investigations which involve the interaction of electromagnetic radiation (in the field of the Uv-vis-NIR range) with the colloid either using extinction.

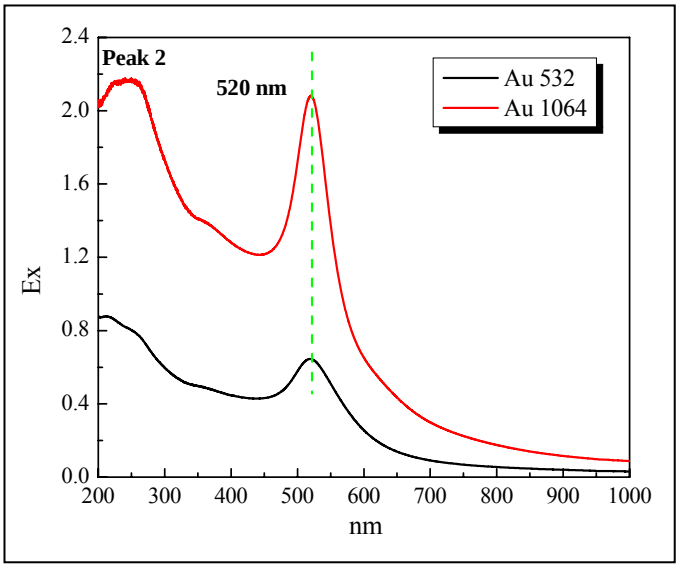

Fig. 2.14: Uv-Vis spectra of gold nanoparticles prepared by 1064 and 532 wavelengths.

UV-vis absorption spectra at 2 J/cm^2 fluence for 532, and 1064 nm wavelength ablation are shown in Fig. 2.14.

The spectra consist of strong absorption due to plasmon band around 520 nm.

The observation of an additional absorption peak in the ultraviolet wavelength region (Peak 2) is the important result.

Peak 2 can be attributed to the absorption due to the interband transition in Au nanoparticles. An interband absorption can be possible at shorter wavelengths due to the transition of an electron from the occupied *d-level* state to an empty state in the conduction band above the Fermi level in noble metals [58]. A weak and broad absorption peak corresponding to interband transition has been observed at a wavelength of around 240-

320 nm with a very strong plasmon peak in chemically prepared Au nanoparticles [59].

A comparison of absorbance of inter-band transitions at 270 nm indicates that the formation efficiencies of colloids increase with an increase in the laser wavelength under our conditions.

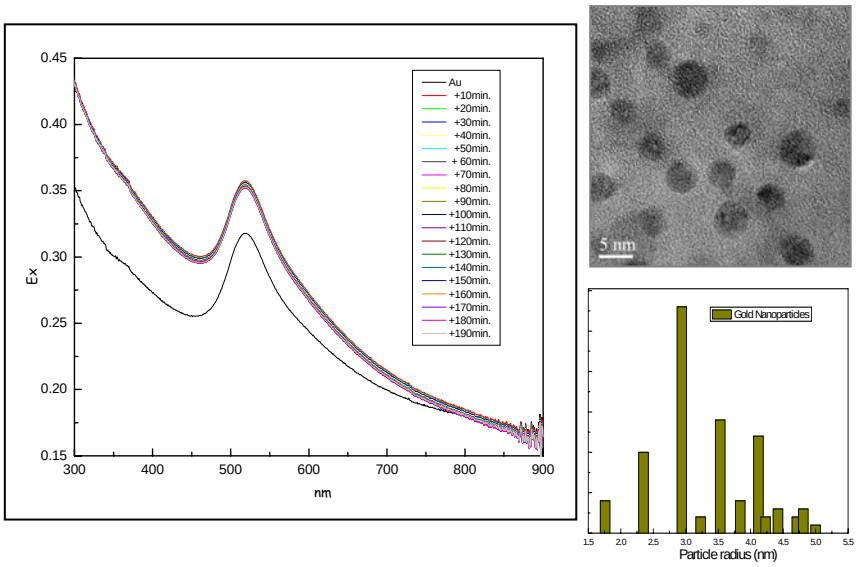

Fig. 2.15: Uv-Vis spectrum of aged gold nanoparticles8on the left) and Tem images of gold nanoparticles "as prepared"

The solutions of free nanoparticles, without any stabilizing agent, are stable at least for several hours at room temperature without any appreciable change of their Uv-Vis spectrum (Fig. 2.15).

These spectra show a stable colloid (up to 10 hours) constituted by spherical particles. The averages diameter measured with TEM analysis is R=3.34

Studies of stability of pure systems have been carried out with UV-Vis spectroscopy.

Fig. 2.16 reports the UV-vis experimental spectra of Au "as prepared"(black line) obtained in water by laser ablation with second harmonic (532 nm) and the spectrum recorded for the same "aged" sample (red line).

The same figure shows that the width of the 520-nm peak is broadened and the height is lowered more greatly by aging of nanoparticles.

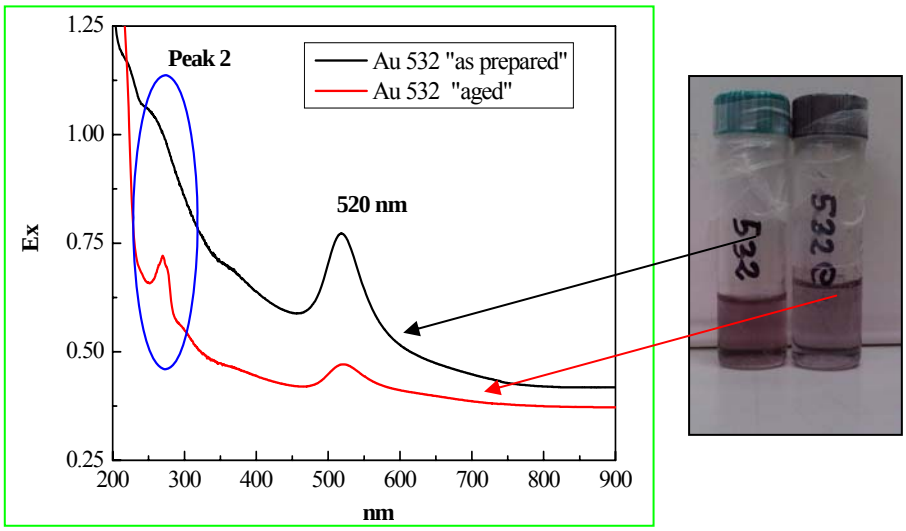

Fig. 2.16: Comparison between gold nanoparticles" as prepared" and "aged"

As reported in literature, the optical absorption due to interband transition has been observed to dominate the plasmon absorption on decreasing the particle size. Balamurugan an co-workers[58] observed this phenomena for nanoparticles smaller sized of 2.5 nm.

In this regard, the spectral change implies that the average diameter of the gold nanoparticles is reduced due to aging.

Further experiments are needed to understand the concentration dependence of dynamic of aggregation.

Moreover, in order to study the influence of the solvent into the aggregation phenomena of gold nanoparticles, water was gradually removed, by evaporation in air at room temperature, until the suspension volume was reduced of 80%.

With this in mind we monitored changing in the extinction spectra after a gradual removal of water until its whole elimination. Figure 2.17 reports UV-vis spectra of colloidal suspensions with a reduction of volume respectively of 50%, 66%, 80% and 100% to respect the starting solution. In the same figure extinction spectrum of the as prepared gold colloidal solution (lowest concentration corresponding to 0% of water removal) is also shown for comparison.

By varying the water volume the plasmon band (at 520 nm) gradually changes; at first an absorption spectrum with one symmetric peak is observed, which grows in intensity without any changing in the shape (50%, 60%) and position. However, after a removal of 80% in volume of water (by evaporation in dry air) a marked broadness of the plasmon resonance with the appearance of a shoulder at low-energy (630 nm) and a clear increasing in intensity is observed, while remaining the maximum of SPR in the almost same position (523 nm). Spectral changes in the latter spectrum are respectively associated to the highest concentration sampled (increased intensity) and nanoparticles aggregation phenomena that take place in liquid (variations observed in the shape of the plasmon), even if in small extent, and they are merely due to the improved interaction for the significant reduction of the volume.

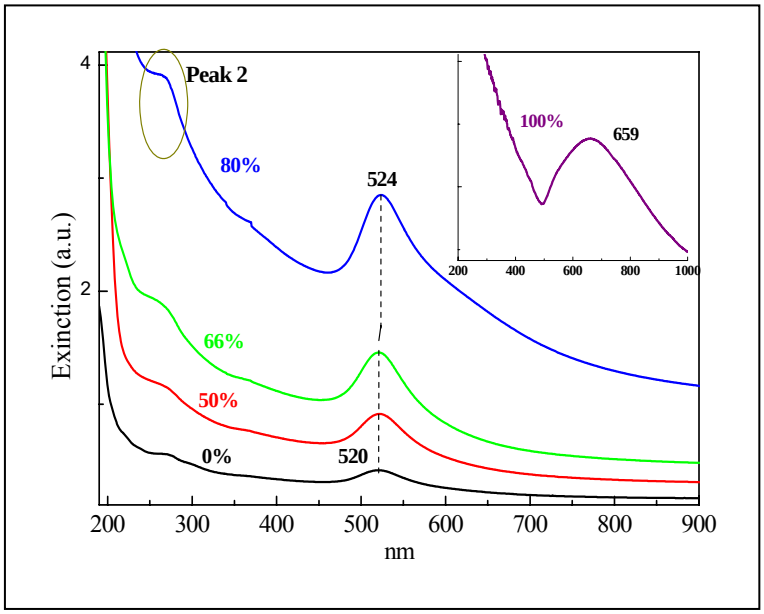

Fig. 2.17: Comparison of Uv-Vis spectra of gold nanoparticles art different concentration.

Also, in these extreme conditions, the appearance of the peak at 270 nm could be explain the shape of the plasmon resonance peak is due to size of nanoparticles, due to since bigger nanoparticles tend to sediment, so the main contribution to extinction is given by smaller nanoparticles

Only, After the total solvent removal, we measured the extinction spectra of the deposited colloidal nanoparticles on a fused silica substrate (see inset in Fig.2.17). In solid state the SPR peak exhibited a much more significant red-shift to respect the concentrated colloidal dispersion and it is relocated to 660 nm.

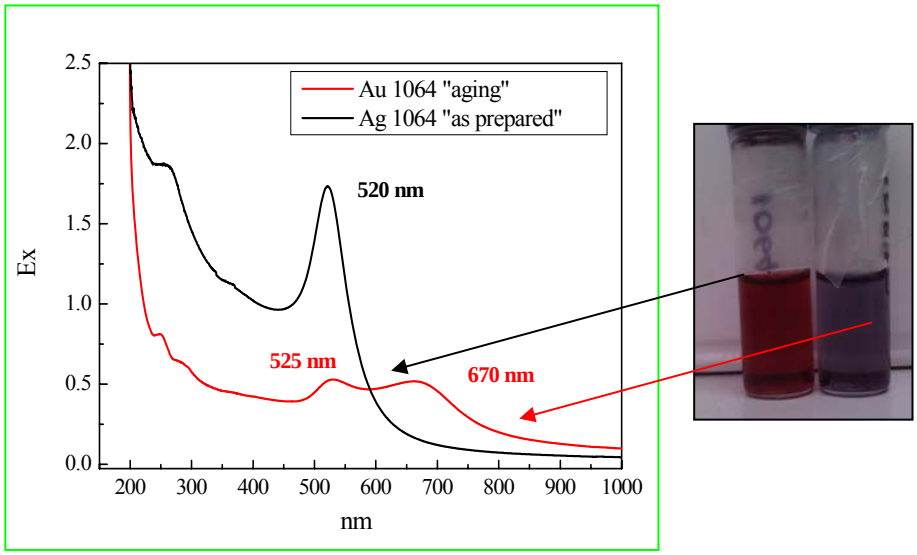

Fig. 2.18: Comparison between gold nanoparticles" as prepared" and "aged"

The same procedure has been done for gold nanoparticles prepared by 1064 nm wavelengths. Figure 2.18 show the aging effect on the Uv-Vis spectra of this sample. In this case the shape of the plasmon bands changed drastically and a strong band near 670 nm clearly indicating that aggregation of gold nanoparticles took place. Aging of the solution of free nanoparticles leads to large aggregation in particular because they are not capped with other molecules that could induce electrostatic repulsion between the particles, if they are charged, or to steric effects like in the case of polymers.

The strong differences observed in the UV-Vis spectra of aging gold nanoparticles synthetized in water by two different wavelenght can be understood by using DLS measurement.

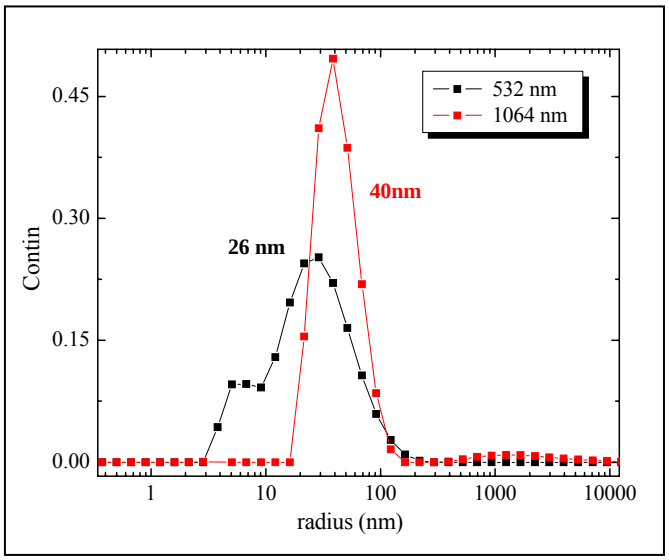

Fig. 2.19: DLS of gold nanoparticles

Dynamic Light Scattering (DLS) has been employed to obtain an 'in liquid' size distribution of the obtained particles by using a Horiba LB-550 system. The technique exploits the Brownian motion of the particles which causes a Doppler shift in the incident light frequency.

The amount of frequency shift is related to the frequency of the Brownian motion, which is related to the size of the particles. In the case of silver sols obtained by using 532 and 1064 radiations the size distribution as obtained by DLS is reported in Figure 2.19.

The figure shows that the ablation performed at 532 nm given small particles (26 nm), while the infrared radiation (1064 nm) is able to produce clusters with sizes extending up to 40 nm.

Further XPS investigation have demonstrated that the chemistry of the surface appeared similar for both samples. So, probably, aging effect depends on the different starting sizes.

Controlling the aggregation of gold nanoparticles have useful application in nanotechnology. Welding and sintering at the nanoscale is of fundamental importance in bottom-up fabrication of nanodevices. Strong efforts have been given in recent years to interconnect metallic nanoparticles taking the advantage of interactions existing between the nanoparticles when they are covered with suitable organic or inorganic shells.

Of course these last processes leave behind problems with respect to the ohmic contact when specific electrical properties or plasmon propagation features are requited in the fields of electronics and plasmonics.

It is then desirable to find out new routes to join together metallic clusters in a controlled way with the following specifications:

- low temperature and low load processes
- save either the single electron transfer and the propagation of plasmon waves
- limit as much as possible the introduction of defects

In this way it could be possible to use these approaches in a broad range of modern organic/inorganic devices, including organic light emitting diodes and photovoltaic cells.

In this caption we report how gold nanoparticles produced with this method in pure water, spontaneously form gold nano-networks with micrometer scale long gold wires obtained by cold welding among the already formed metallic clusters.

Particular emphasis has been given to the microscopic study of the network through a high resolution TEM investigation of the contacts points.

Welding and networking between the nanoparticles is obtained with the as prepared colloid after the deposition onto a hydrophilic surface (carbon TEM grids) with a slow evaporation process as reported in Fig.2.20a.

The network is composed by well joined gold structures whose welding has been further investigated by the powerful features of the aberration corrected TEM machine as reported in Fig.2.20b

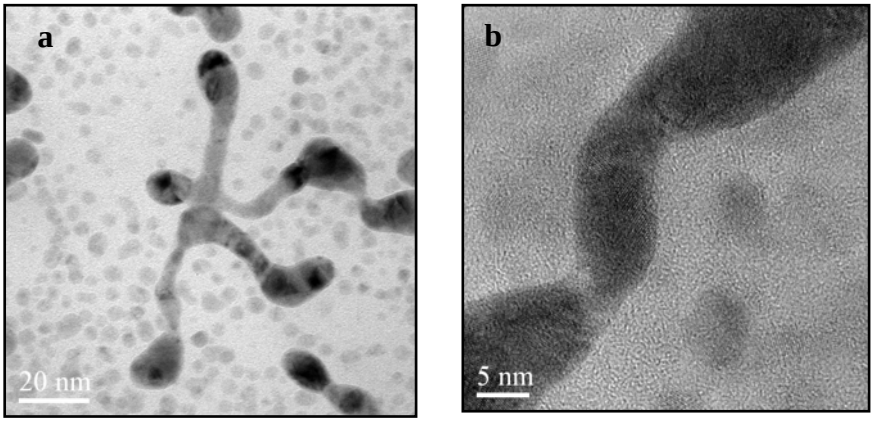

Fig. 2.20: TEM images of gold nanoparticles prepared by pulsed laser ablation using 532 nm irradiation wavelength

Similar structures are also observed by SEM as reported in Fig.2.21.First of all we notice that nearly all welding junctions present a typical neck-like structure as recently observed [60] during a study on spontaneous welding of gold nanowires (see arrows in fig.2.20). Indeed it has been

established that unlike traditional cold welding of bulk materials, which normally requests high load (>100 MPa for metallic thin films), [61], the cold welding of ultra-thin nanowires can occur easily for clean surfaces where there are matching crystalline orientations) and little external forces. In our specific case this force can be built in during the evaporation of the solvent still providing browning motion of very close clusters with increasing collision frequencies, responsible for the random nature of the network. In this phase, particles are still free to rotate enabling the contact between suitable matching surfaces.

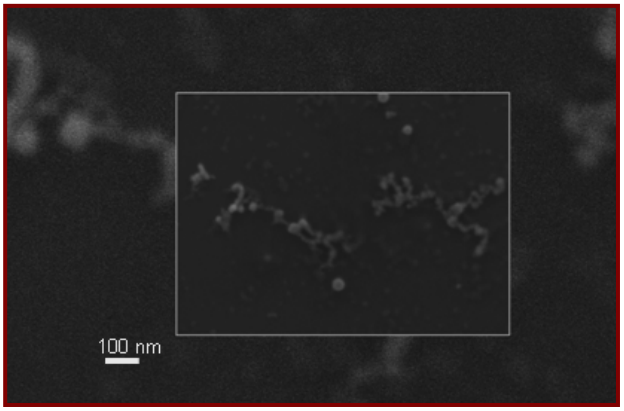

Fig. 2.21: SEM images of gold nanoparticles

Several studies conducted by Liao et al. [44] concluded that a self-organization of gold nanoparticles into linear structures can be explained in terms of strong dipole/dipole interactions generated by an asymmetric charge distribution onto the cluster surface. The interactions are strong enough to overcome the electrostatic repulsions between the colloidal

particles[44]. In addition, Werner et al.[62] demonstrate that the laser irradiation at 532 nm of preformed gold nanoparticles in water produces positively charged Au clusters as a consequence of electron ejection and Coulombic explosions.

Positively charged nanoparticles form aggregates when interacting with pre-existent negatively charged gold particles (the *zeta*-potential of the water suspension is reported negative).

Furthermore, the surface chemistry of surfactant-free gold nanoparticle obtained by laser ablation in water was deeply investigated by Sylvestre et al.[42] and Muto et al.[43] It was demonstrated that surface gold atoms are oxidized (AuOH and AuO^-), and equilibrium between the neutral (AuOH) and the negatively charged species (AuO^-, ξ-potential reported of about -30 mV) exists in solution as follows [42]:

$$Au\text{-}OH \leftrightarrow Au\text{-}O^- + H^+$$

Our experimental data are in accordance with a negative charge (-37 mV for free-gold nanoparticles of about 12.5 nm) on the metal nanoparticle surface. Therefore, we consider our gold colloidal suspension as composed by both neutral and negatively charged gold clusters. Neutral gold nanoparticles probably tend to aggregate in water and to precipitate after a week-long aging period.

In conclusion, these results show that control of the size and shape can be obtained, but further investigation are required for a better control of the new plasmonic structures.

2.4 PLAL of copper nanoparticles

PLA of stable copper nanoparticles has been performed successfully in water. The obtained colloidal solutions show the characteristic PR band of copper around 680 nm(figure 2.22).
Tem images relative to the same sample are reported in fig. 2.22.
In this case the copper nanoparticles average radius is found to be R=3.84
A discrete stability in time has been observed.

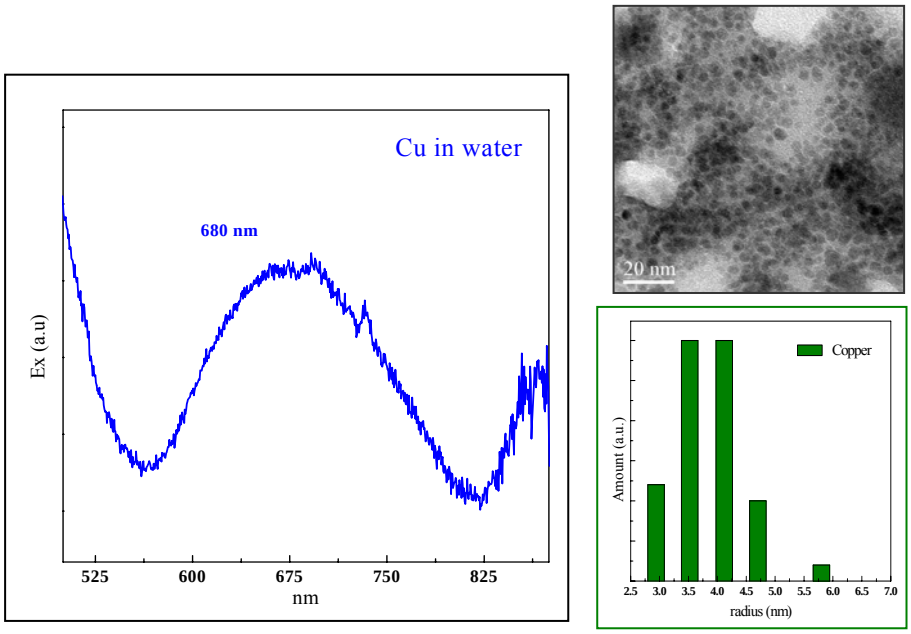

Fig. 2.22: Uv-Vis spectrum of copper nanoparticles and corresponding TEM image.

A fast Fourier transform (FFT) performed on several TEM images simulates the diffraction patterns and mainly reveals the presence of Cu crystalline structure, as evidenced by the diffraction spots (Figure 8a). In some images, traces of Cu oxide are observed (not shown here). Further structural characterization analysis are in progress.

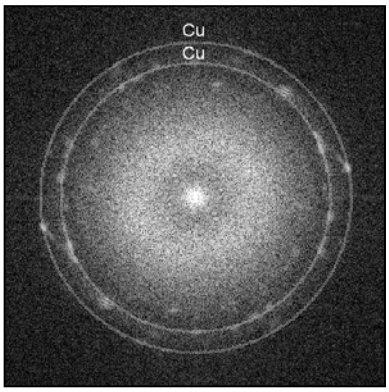

Fig.2.23: Diffraction patterns obtained by fast Fourier transform (FFT) performed on high magnification TEM images of small Cu clusters.

2.5 Generation of AgCl Cubes by PLAL of Bulk Ag in Aqueous NaCl Solutions

The development of nanoparticle generation by pulsed laser ablation in liquid (PLAL) is closely related to the preparation of Ag colloids and nanoparticles by PLAL. Previous work produced Ag colloids using a Q-switched Nd:YAG laser (1064 nm) to ablate bulk Ag in water or aqueous solutions of NaCl and applied the colloids in surface-enhanced Raman scattering spectroscopy [63-65]. Past work has revealed that although NaCl could increase the formation efficiency of Ag nanoparticles, the NaCl would also inhibit or even prevent the formation of Ag nanoparticles (as indicated by the absorption spectra of the colloids) if C_{NaCl} increased to a certain value,[65,66] for example, 0.07 M [65], while the reason for this was unknown.

We have systematically studied the pulsed laser ablation of bulk Ag in NaCl solutions using an excimer laser and proposed a mechanism to explain the particle growth. Previous reports of laser ablation of bulk Ag in NaCl solutions did not include structural analyses of the products and omitted the possible reaction of laser-generated Ag species with the electrolyte [63-67], while in our research, X-ray diffraction (XRD) analyses showed the laser-fabricated products in NaCl solutions with C^{NaCl} e 0.01 M were predominately AgCl instead of Ag. The AgCl particles have cubic morphologies. The presence of the surface plasmon bands (PR) close to 400 nm in the absorption spectra of laser-ablated solutions indicate Ag nanoclusters also existed in the solutions. We consider that the photochemical properties of AgCl in an aqueous solution could benefit the formation of Ag nanoclusters from Ag^+ ions under laser irradiation, which may be the reason that NaCl could promote

the formation efficiency of Ag nanoparticles as previously speculated[66]. Very recently, studies have revealed that AgCl/Ag nanocomposites are plasmonic photocatalysts [68-70].

In particular, Sun et al. fabricated AgCl/Ag hybrid nanoparticles that showed sunlightdriven photocatalytic activity[68]. The hybrid nanoparticles were produced by partial reduction of AgCl nanocubes at an elevated temperature[68]. The research results herein reveal the particle formation mechanism by laser ablation of Ag in NaCl solution and that the products have potential applications for water treatment and solar energy conversion.

The experiments were conducted by pulsed laser ablation of a silver metal target (99.99%) in water or aqueous solutions of NaCl (99.0%). The C_{NaCl} ranged from 10^{-5} to 0.1 M and the volume of the NaCl solution was 5mL for each experiment.

The laser fluence was set to 2 J/cm^2 and the ablation time was either 5 or 20 min. After ablation, the products were collected from the colloids by centrifugation. The resulting deposits, with a small amount of residual solution, were cast onto glass or silicon substrates and dried at room temperature for XRD and scanning electron microscopy (SEM) characterization, respectively.

The formation efficiency of Ag nanoparticles prepared by laser ablation in a NaCl solution could be characterized by the maximum absorbance of the typical SPB in the absorption spectrum [65,66].

Figure 2.24 shows the absorption spectra of the colloids prepared in water and NaCl solutions with different concentrations. The laser fluence was 2 J/cm^2 and the ablation time was 5 min.

An absorption band at ~ 398 nm could be observed in each spectrum when the NaCl concentration is lower than 5×10^{-2} M.

The absorption band corresponds to the surface plasmon resonance of Ag nanospheres [71], indicating that Ag nanoclusters have formed in the solution.

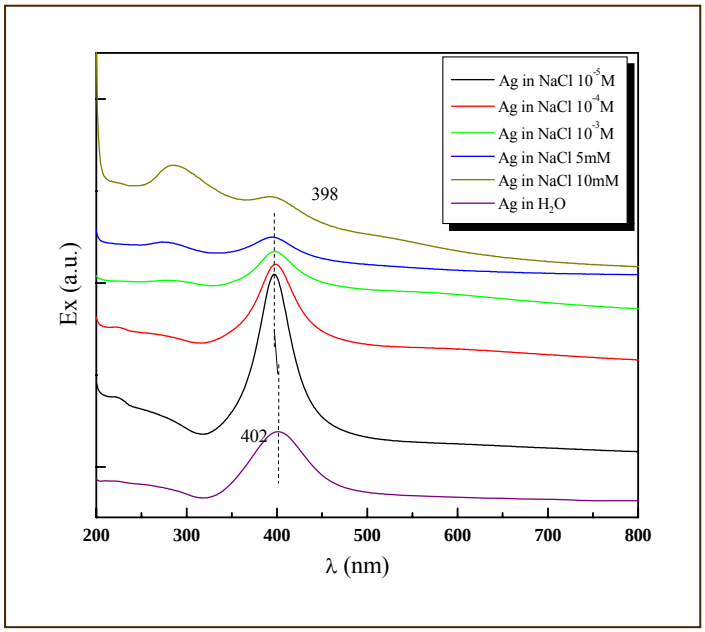

Fig.2.24: Uv-Vis Spectra of silver nanoparticles a different concentrations of NACl solutions.

Another absorption band at ~275 nm also becomes visible when C_{NaCl} is 0.001 to 0.01 M (Fig. 2.25), probably due to the formation of AgCl in the solution. Similar absorption bands around 250 nm has been observed in absorption spectra of AgCl nanoparticles [70,73].

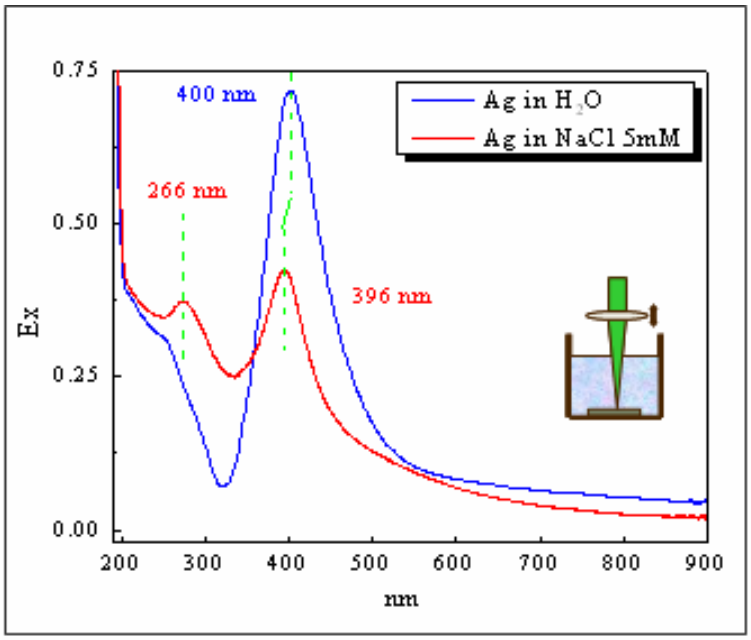

Fig. 2.25: Comparison of silver nanoparticles in water and in NaCl solution.

The centrifuged deposits with ~0.02 mL residual solution from samples prepared with laser fluence of 2 J/cm^2 were dropped onto glass substrates for XRD analyses. Figure 2 shows the XRD patterns of the samples.

The 0.005 M NaCl solution, after 5 min laser ablation, still contains NaCl as characterized by the diffraction peak located at 2θ value of 31.7º in Figure 2.26a. (JCPDS card no. 77- 2064).

A weak peak at 32.2 º belonging to the cubic phase of AgCl (JCPDS card no. 31-1238) also appears. When the ablation time is increased to 20 min, the amount of residual NaCl decreases and diffraction peaks from AgCl in Figure 2.26b becomes more visible than that in Figure 2.26a.

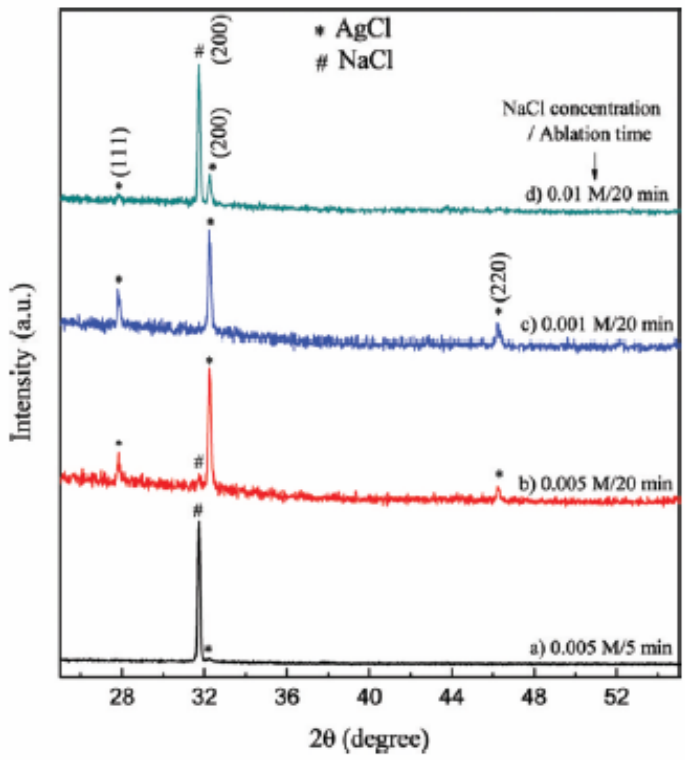

Fig 2.26: XRD patterns of the laser fabricated products and residues from NaCl solutions.

With 20 min ablation time, NaCl is nearly all consumed in the 0.001 M NaCl solution as the diffraction peak from NaCl disappears in Figure 2.26c, but it is still abundant in the 0.01 M NaCl solution as indicated by Figure 2.26d. It should be noted that although Ag nanoclusters exist in the solution as indicated by the absorption spectra, diffraction peaks from Ag could not be identified in the XRD patterns, probably because there was much less Ag than the amount of AgCl particles, or they are too small to be centrifuged from the solutions.

Figure 2.27a,b shows the SEM image of products and residues obtained from 0.005 M NaCl solution after laser ablation for 5 and 20 min, respectively. Microcubes could be observed in Figure 2.27a which are NaCl crystals as indicated by Figure 2.26a and are further confirmed by the EDS pattern shown in the inset. The peak of Si came from the substrate used to hold the sample. In Figure 2.27b, NaCl crystals cannot be observed. Instead, AgCl particles show up and the EDS pattern in the inset reveals the existence of Ag and Cl elements. A magnified SEM image of the AgCl particles is shown in Figure 2.27c. The particles have cubic morphologies although some of them lack well-defined facets.

The cubes are polydispersed with the sizes on the scale of several hundred nanometers. Figure 2.27d shows the products from 0.001 M NaCl solution, similar cubes can be observed.

Recently, AgCl nanocubes with average edge length of 130 nm have been synthesized by a precipitation reaction between Ag^+ and Cl^- ions in polyol synthesis [68]. The AgCl in the laser-ablated solution should also form by the precipitation. It is worth noting that the generation of AgCl is limited by the amount of Cl^- ions, which in turn, depends on the amount of NaCl and the ablation time.

The cubic morphology may be partly caused by the Cl^- ions. Several studies have shown that Cl^- ions have the ability to promote the formation of cubic morphology, including during the PLAL,[74,75], probably due to the preferred absorption of Cl^- ions to {100} facets of a cubic structure as it lowers the surface energy of these facets and stabilizes a cubic morphology.

Although the previous reports did not consider the formation of AgCl in NaCl solution during the laser ablation,[63-67], our experimental results indicate that AgCl should form in a NaCl solution with proper concentration if Ag^+ ions exist. AgCl is almost insoluble in water (the

solubility product $[Ag^+][Cl^-] = 2 \times 10^{-10}$) [75]. A previous study on laser ablation of Ag in aqueous electrolyte solutions, including NaCl solutions, proposed that electric bilayers, such as Ag^+/Cl^-, may build up on Ag nanoclusters that prevent aggregation and/or further growth [67]. While the build-up of a Ag^+/Cl^- electric bilayer is less likely considering the low solubility of AgCl, the formation of a AgCl thin layer on a Ag nanocluster may play similar role, that is, preventing further growth.

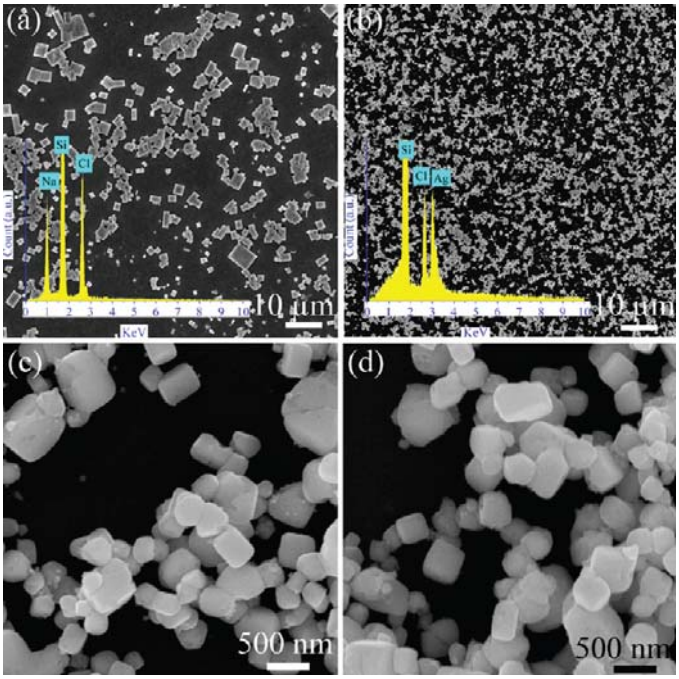

Fig. 2.27: SEM images of products and residues obtained by laser ablation of Ag in 0.005 M NaCl solutions for (a) 5 min and (b) 20 min, and magnified images of AgCl cubes obtained in (c) 0.005 M and (d) 0.001 M NaCl solution with ablation time of 20 min. The insets in (a) and (b) are the corresponding EDS patterns. The laser fluence was set to 15.0 J/cm^2.

The decrease and eventual disappearance of Ag nanoclusters in a NaCl solution with C_{NaCl} g 0.05 M could be explained considering the extra Cl^- anions. With the increasing of C_{NaCl}, complex anions of the type $AgCl_{m+1}$

$$AgCl + mCl^- \rightleftharpoons AgCl_{m+1}^{m-}$$

The reaction will shift to the right with the increasing of $Cl_{concentration}$. The complex anions are soluble in water [75], thus the amount of AgCl will decrease and the reduction of Ag^+ to Ag will be limited. Recent work has shown that AgCl particles could be fabricated into AgCl/Ag plasmonic photocatalysts by heat treatment [68], or light irritation of AgCl particles in a solution of methyl orange dye [70]. While the laser-fabricated AgCl cubes could be also treated by these routes, it is preferred to directly produce AgCl/Ag photocatalysts by a modified laser ablation procedure, and further investigation is under way.

In summary, we have studied the laser ablation of bulk Ag in NaCl solution with different NaCl concentrations, and ablation times. The laser ablation of Ag in NaCl solution provides a facile route to fabricate AgCl cubes, and the colloids of AgCl with Ag/Ag^+ may find applications in organic pollutants treatment and solar energy utilization.

References

[1] Dijkkamp, D.; Venkatesan, T.; Wu, X.D.; Shaheen, S.A.; Jisrawi, N.; Minlee, Y.H.; Mclean, W.L. and Croft, M., *Appl. Phys. Lett.*, (1987), **51**, 619.

[2] Radhakrishnan, G. and Adams, P.M., *Appl. Phys. A*, (1999), **69**, S33.

[3] Pappas, D.L.; Saenger, K. L.; Bruley, J.; Krakow, W.; Cuomo, J.J.; Gu, T. and Collins, R.W.; *J. Appl. Phys.*, (1992), **71**, 5675.

[4] Kempa, K.; Kimball, B.; Rybczynski, J.; Huang, Z.P.; Wu, P.F.; Steeves, D.; Sennett, M.; Giersig, M.; Rao, D.V.; Carnahan, D.L.; Wang, D. Z.; Lao, J.Y.; Li, W.Z. and Ren, Z.F., *Nano Lett.*, (2003), **3**, 13.

[5] Duan, X.F. and Lieber, C.M., *Adv. Mater.*, (2000), **12**, 298.

[6] Sun, Y.; Fuge, G.M.; Fox, N.A.; Riley, D.J. and Ashfold, M.N.R., *Adv. Mater.*, (2005), **17**, 2477.

[7] Yang, H.G.; Zeng H.C., *J. Phys. Chem. B*, (2004), **108**, 3492.

[8] Mirkin, C.A.; Letsinger, R.L.; Mucic, R.C. and Storhoff, J.J., *Nature*, (1996), **382**, 607.

[9] Sun, Y.G.; Gates, B.; Mayers, B. and Xia, Y. N., *Nano Lett.*, (2002), **2**, 165.

[10] Li, Y.D.; Li, X.L.; Deng, Z.X.; Zhou, B.C.; Fan, S.S.; Wang J.W. and Sun, X.M., *Angew. Chem. Int. Ed.*, (2002), **41**, 333.

[11] Ogale, S.B.; Patil, P.P.; Phase, D.M.; Brandarkar Y.V.; Kulkarni S.K.; Kulkarni, S.; Ghaisas, S.V.; Kanetkar, S.M.; Bhide, V.G. and Ghua, S., *Phys. Rev. B*, (1987), **36**, 8237.

[12] Compagnini, G.; Patanè, G.; D'Urso, L.; Puglisi, O.; Cataliotti, R.S. and Pignataro, B., *J. Phys. Chem. C* , (2008), **112**, 20301.

[13] Compagnini, G.; Messina, E.; Cataliotti, R.S.; Grillo, A. and Giaquinta, G., *Phylos. Mag. Lett.* , (2009), **89,** 250.

[14] Courant, R. and Friedrichs, K.O., *Supersonic Flows and Shock Waves* (1948).
[15] Cole, R.H., *Underwater Explosions* (1948).
[16] Compagnini, G.; Messina, E.; Puglisi, O.; Cataliotti, R.S. and Nicolosi V., *Chem. Phys. Lett.*, (2008), **457**, 386.
[17] Fabbro, R.; Fourntier, J.; Ballard, P.; Devaux, D. and Virmont, J., *J. Appl. Phys.* (1990), **68**, 775.
[18] Berthe, L.; Fabbro, R.; Peyer, P.; Collier, L. and Bartnicki, E., *J. Appl. Phys.* (1997), **82**, 2826.
[19] Fabbro, R.; Peyer, P.; Berthe, L. and Scherpereel, X.J., *Laser Appl.* (1998), **10**, 265.
[20]Yang, G.W., *Prog. Mat. Sci.*, (2007), **52**, 648.
[21] Sakka, T.; Takatani, K.; Ogate, Y.H. and Mabuchi, M., *J. Phys. D: Appl. Phys.*, (2002), **35**, 65.
[22] Devaux, D.; Fabbro, R.; Tollier, L. and Bartnicki E., *J. Appl. Phys.*, (1993), **74**, 2268.
[23] Peyer, P. and Fabbro, R., *Opt. Quantum Electron.*, (1995), **27**, 1213.
[24] Peyer, P.; Scherpereel, X.J. and Fabbro, R., *J. Mat. Sci.*, (1998), **33**, 1421.
[25] Berthe, L.; Fabbro, R.; Peyer, P. and Bartnicki, E., *J. Appl. Phys.*, (1993), **85**, 7552.
[26] Berthe, L.; Sollier A.; Fabbro R.; Peyer P. and Bartnicki E., *J. Phys. D: Appl. Phys.*, (2000), **33**, 2142.
[27] Peyer, P.; Berthe, L.; Fabbro, R. and Sollier, A., *J. Phys. D: Appl. Phys.*, (2000), **30**, 498.
[28] Hirschfelder, J.O.; Curtis, C.F. and Bird, R.B., *Molecular Theory of Gases and Liquids* (1967).
[29] Geiger, M.; Becker, W.; Rebhan, T.; Hutfless, J. and Lutz, N., *Appl. Surf. Sci.*, (1996), **96-98**, 309.

[30] Zhu, S.; Lu, Y.F.; Hong ,M.H. and Chen, X.J., *J. Appl. Phys.*, (2001), **89**, 2400.

[31] Zhu, S.; Lu, Y.F. and Hong, M.H., *Appl. Phys. Lett.*, (2001), **79**, 1396.

[32] Kim, D.S.; Oh, B. and Lee, H., *Appl. Surf. Sci.*, (2004), **222**, 138.

[33] Scalisi, A.; Compagnini, G. and Puglisi O., *J. Appl. Phys.*, (2003), **94**, 7874.

[34] Im, S.H.; Lee, Y.T.; Wiley, B. and Xia, Y., *Angew. Chem. Ind. Ed.* (2005), **44**, 2154.

[35] Jana, N.R.; Gearheart, L. and Murphy, C.J., *J. Phys. Chem. B* (2001), **105**, 4065.

[36] Jin, R.; Cao, Y.; Mirkin, C.A.; Kelly, K.L.; Schatz, G.G.; Zheng, J.G., *Science*, (2001), **294**, 1901.

[37] Sun, Y.; Mayers, B.; Herricks, T. and Xia, Y. Nano Lett. , (2003), **3**, 955

[38] Zheng, X.; Xu, W.; Corredor, C.; Xu, S.; An, J.; Zhao, B. and Lombardi, J.R. *J. Phys. Chem. C*, (2007)**, 111**, 14962.

[39] Kirkland, A.I., *Proc. R. Soc. London A* ,(1993), **440**, 589.

[40] Compagnini, G.; Scalisi, A.A. and Puglisi, O., *J. Mat. Res.*, (2004), **19**, 2795.

[41] Ohtsu, M.; Kobayashi, K.; Kawazoe, T.; Sangu, S.; Yatsui, T. *IEEE J. Sel. Top. Quantum Electron.* (2002)**, 8**, 839.

[42] Sylvestre, J.P.; Poulin, S.; Kabashin, A.V.; Sacher, E.; Meunier, M. and Luong, J.H.T., *J. Phys. Chem. B*, (2004), **108**, 16864.

[43] Muto, H.; Yamada, K.; Miyajima, K. and Mafune´, F., *J. Phys. Chem.C* (2007**)**, **111**, 17221.

[44] Liao, J.; Zhang, Y.; Yu, W.; Ge, C.; Liu, J. and Gu, N., *Colloids Surf. A*, (2003**)**, **223**, 177.

[45] Vogel, A.; Noack, J.; Nahen, K.; Theisen, D.; Busch, S.; Parlitz, U.; Hammer, D.X.; Noojin, G.D.; Rockwell, B.A. and Birngruber, R., *Appl. Phys. B*, (1999), **68**, 271.
[46] Mafunè, F.; Kohno, J.; Takeda, Y.; Kondow, T. and Sawabe, H. *J. Phys. Chem. B*. (2000), **104**, 9111.
[47] Amendola, V.; Polizzi, S. and Meneghetti, M. *Langmuir*, (2007), **23,** 6766
[48] Wiley, B.; Sun, Y.; Mayers, B. and Xia, Y. *J. Chem .Eur.*. (2005)**,** **11**, 454.
[49] Cotton, F.A.; Wilkinson, G. *Advanced Inorganic Chemistry,* (1988).
[50] Yan lagmiur cubi di Ag2O
[51] Bruzzone, S.; Malvaldi, M., *J. Phys. Chem. C*, (2009), **113**, 15805.
[52] D'Urso, L.; Grasso, G.; Messina, E.; Bongiorno, C.; Scuderi, V.; Scalese, S.; Puglisi, O.; Spoto, G. and Compagnini, G. *J. Phys. Chem. C* (2010), **114**, 907
[53] Encina E.R. and Coronado E.A., *J. Phys. Chem. C* (2010), **114**, 3918.
[54] Scuderi, V.;Scalese, S.; Bagiante, S.; Compagnini, G.; D'Urso, L. and Privitera, V., *Carbon* (2009), **47**, 2134.
[55] Tsuji, T.; Iryo, K.; Watanabe, N. and Tsuji, M.; *Appl. Surf. Sci.* (2002), **202**, 80.
[56] Salata, O.V., *J. of Nanobiotechnology*, (2004), **2**, 1.
[57] Sun, Y. and Xia Y., *Science*, (2002), **298**, 2176.
[58] Balamurugan, B. and Maruyama T., *Appl. Phys. Lett.*, (2005), **87**, 143105.
[59] Link, S. and. El-Sayed, M. A, *J. Phys. Chem. B*, (1999), **103**, 4212.
[60] Lu, Y.; Huang, J.Y.; Wang, C.; Sun, S. and Lou, J., *Nat. Nanotech.,* (2010), **5**, 218.
[61] Kim, C.; Burriws, P.E. and Forrest, S.R., *Science* (2000), **288**, 831.

[62] Werner, D.; Hashimoto, S.; Tomita, T.; Matsuo, S. and Makita, Y., *J. Phys. Chem. C* (2008), **112**, 16801.
[63] Prochazka, M.; Mojzes, P.; Stepanek, J.; Vlckova, B. and Turpin, P.Y., *Anal. Chem*., (1997), **69**, 5103.
[64] Prochazka, M.; Stepanek, J.; Vlckova, B.; Srnova, I. and Maly, P., *J. Mol. Struct.*, (1997), **410**, 213.
[65] Srnova, I.; Prochazka, M.; Vlckova, B.; Stepanek, J. and Maly, P., *Langmuir*, (1998), **14**, 4666
[66] Bae, C.H.; Nam, S.H. and Park, S.M., *Appl. Surf. Sci.* (2002), **197**, 628.
[67] Siskova, K.; Vlckova, B.; Turpin, P. Y.and Fayet, C., *J. Phys. Chem. C*, (2008), **112**, 4435.
[68] An, C.H.; Peng, S.N. and Sun, Y.G., *Ad*v. *Mater.*,(2010), **22**, 2570.
[69] Li, Y.Y. and Ding, Y., *J. Phys. Chem. C* (2010), **114**, 3175.
[70] Wang, P.; Huang, B.B.; Lou, Z.Z.; Zhang, X.Y.; Qin, X.Y.; Dai, Y.; Zheng, Z.K. and Wang, X.N., *Chem. Eur. J*., (2010), **16**, 538.
[71] Ohde, H.; Hunt, F. and Wai, C.M., *Chem. Mater.*,(2001), **13**, 4130.
[72] Husein, M.; Rodil, E. and Vera, J., *Langmuir*, (2003), **19**, 8467.
[73] Zhang, W. C.; Wu, X.L.; Chen, H. T.; Gao, Y.J.; Zhu, J.; Huang, G.S. and Chu, P.K., *Acta Mater.*, (2008), **56**, 2508.
[74] Liu, P.; Cao, Y. L.; Wang, C. X.; Chen, X. Y. and Yang, G. W., *Nano Lett.*, (2008), **8**, 2570.
[75] Forbes, G.S., *J. Am. Chem. Soc.*, (1911), **33**, 1937.

3 METAL /CARBON STRUCTURES

Most of the applications involving metal nanoparticles require a high resistance to aggregation and oxidation phenomena to preserve and modulate the peculiar reactivity, electronic, optical, and magnetic properties of nanoparticles. Linear carbon chains (LCCs) containing sp hybridization either as alternating triple and single bonds (polyynes) or with consecutive double bonds (cumulenes) are good candidates to create a shell that prevents such unwanted degradation phenomena. In addition, the development of reliable experimental protocols for their synthesis over a range of sizes and high monodispersity is an important challenging issue in most of the biological applications. In this Article, we investigate the interaction between LCCs and different
metal nanoparticles (Cu, Au, Ag) to provide an insight into the factors influencing chemical (reactivity) and physical (optical) properties of the metal/LCCs core/shell systems produced at different experimental conditions.
For this purpose, a range of different complementary experimental techniques such as Raman and UV-vis spectroscopy, transmission electron microscopy, and mass spectrometry are applied, and details on

the different LCCs produced as well as insights into the metal-carbon bonds formed are unveiled.

3.1 Synthesis and characterization of linear carbon chains (LCCs)

The pulsed laser ablation of carbon targets allows a wide range of products starting from several allotropes of carbon under different condition.

So, for example, some techniques may promote the formation of structure diamond-like rather than system similar to graphite.

Furthermore, the ablation of graphite made in a vacuum system allows the deposition of amorphous carbon films with the same features diamond-like [1], or the nano-phase diamond films [2].

Instead, the formation of diamond particulates with cubic crystal structure was obtained only by pulsed ruby laser irradiation of graphite in benzene [3], while the production of nanocrystalline diamond have been obtained using a pulsed laser onto a polycrystalline graphite rod (99,99 %) in water, cyclohexane [4] and acetone [5].

The best result are obtained in the liquid environment because in this condition the plasma has higher value of temperature, pressure and density.

The crystals are formed during the condensation of the plume affected by the quenching liquid. In the case of the nanodiamonds, the plasma contains cluster whit hybridization sp^2 and their ions.

Indeed, when the carbon plate has been irradiated whit the output of the second harmonics (532nm) of ND-YAG laser whit a power density

around 10^{10}W/cm^2, the graphite-water interface there are pressure of 10-15 GPa and temperature 4000-5000 K.

In fig.3.1 shows that this condition corresponding to the stable phase of diamond structure and probably during the quenching of the plasma can take place nucleation and phase transition from graphite to diamond.

The laser ablation of carbon is also used to obtain materials such as carbon nanotubes [6] or a carbon foam [7].

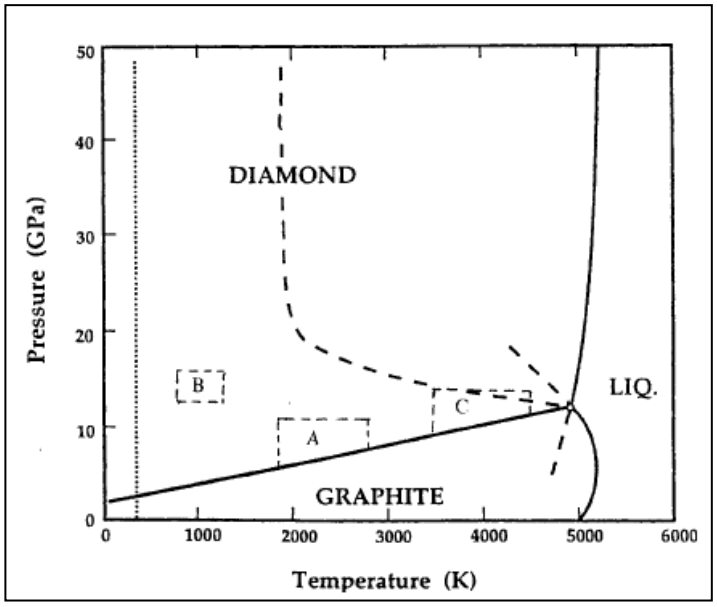

Fig.3.1 : The carbon phase diagram

In addition, this method in liquid environment also led to the discovery of fullerenes [8]. Indeed, ablation of small graphite particles in liquid of various kinds (such as water, iso-propanol and cyclohexane) whit a

pulsed ruby laser (694 nm) , generates different species such as C_{60}, C_{70} and C_{80}-C_{90} [9].

Another particular is represented by linear carbon chain (LCC_s). LCCs (C_nH_2 with n> 4) are carbon-rich molecules of linear configuration. They constitute a linear array of even numbered sp-carbon atoms with alternating single and triple bonds and two cappings at both ends.

The degenerate, cylindrical π-electron system of the molecule is intriguing in view of its optical and electronic properties [10–12].

They can be found also as monocyano or dicyano polyynes and are generally highly reactive under terrestrial conditions and therefore very difficult to synthesize. Interests in their structures and their evolution under different conditions are also due to the detection of these species in interstellar clouds and in the atmosphere of Titan [13].

In material science these species are of central importance because they are considered fundamental structures during the formation of fullerenes and/or carbon nanotubes during their build up [14].

In this respect it has been shown recently that a single chain of carbon atoms can be obtained inside multiwalled and single walled carbon nanotubes which stabilize these evanescent molecular species [15].

Compared to other carbon structure, LCCs remain the most synthetically challenging and difficult to obtain monodisperse and free of other carbon contaminations.

Most of the methods adopted to generate linear carbon chains have as a common feature the formation of hot carbon species under non-equilibrium conditions. Hydrogen-capped C_nH_2 polyynes are formed via polymerization and hydrogenation of C_2 and C_2H radicals with the following scheme:

$$xC_2 \rightarrow C_2x$$

$$C_2x \xrightarrow{+H} C_2xH$$

$$C_2x \xrightarrow{+H} C_2xH_2$$

$$C_2xH_2 + C_{2y} \rightarrow C_2x_{+2y}H \xrightarrow{+H} C_{2x+2y}H_2$$

Since the hydrogen atoms in the last three reactions are supplied from the environment, the role of the bond dissociation and also the nature of the system in which the carbon plasma is ignited are crucial.

Even though a great number of papers are reported in the literature on the mechanism of LCCs formation by pulsed laser ablation or arc discharge in vacuum system, only few group of researchers have worked using liquid as environment.

3.2 LCCs obtained by pulsed laser ablation in water

In our laboratory LCCs solution were prepared using a pulsed laser (PLA) procedure in liquid environment.
In this case it is clear that the role of the environmental species is of crucial importance for the formation of polyynes.
Briefly, a plasma created by the impact of a pulsed ND-YAG laser beam onto a polycrystalline graphite rod (99.99% of purity) was generated in Millipore grade water (5ml) and confined in the surrounding liquid.
The interaction of the high power laser pulse with the target leads to a plume formation, in which both ablated carbon species and small amount of water are vaporised to form a plasma within the liquid.
The high temperatures (of the order of thousands of Kelvin) and pressures (in the range of GPA) reached inside the plume allow LCCs to be created. Consistently, separate sets of LCCs produced by PLA in pure water have been also prepared for comparison.
The incident beam was the second harmonic (532 nm) of a Nd:YAG laser by Continuum, Surelite II model. Conditions for PLA were: pulse duration 5 ns, repetition rate 10 Hz.
The laser irradiation was performed with a fluence at the target surface of about 0.4 J/cm^2 (high enough to overcome the graphite ablation threshold) for 20 min.
The set values of laser fluence and irradiation time were a good compromise to observe appreciable spectroscopic signals and simultaneously prevent the LCCs degradation.
It's important to note that there are not specific data on the solubility of LCCs in water, but in our case the low concentration obtained (10^{-6}M)

allow the preservation of the carbon nanostructures in the liquid, without there being any evidence of precipitation.
In Figure 3.2 shows the diagram instrumental apparatus used. However, a few days later the suspension is unstable and so the system was then characterized immediately by means of UV-Vis spectroscopy.
After irradiation, water appeared the colour of pale yellow, due to the suspension of carbon nanoparticles (Fig.3.3).

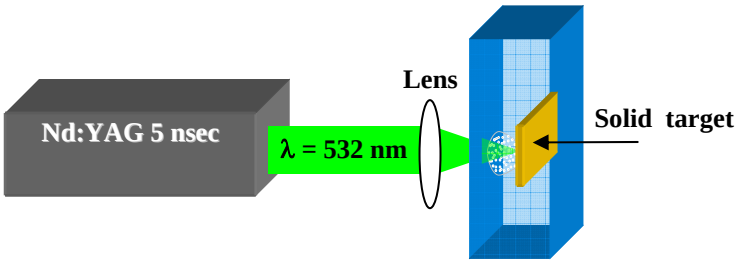

Fig3.2: A block scheme of the set-up used in our experiments to produce LCCs in liquid media. The irradiation condition are described in the text.

Figure 3.3 shows the UV absorption spectra for different polyyne samples obtained by laser ablation in water [16]. The main and most important indication is that the samples obtained provide a simpler spectrum in which the main absorption is found at 200 nm and weaker signals are given at 215 and 225 nm.
Cataldo [17], after HPLC separation from other products, has well classified these last two features indicating that they belong to C_8H_2 species.

No other absorption structures have been observed at higher wavelength, indicating that the ablation in water preferentially produces short molecules with the number of carbon atoms not more than eight.

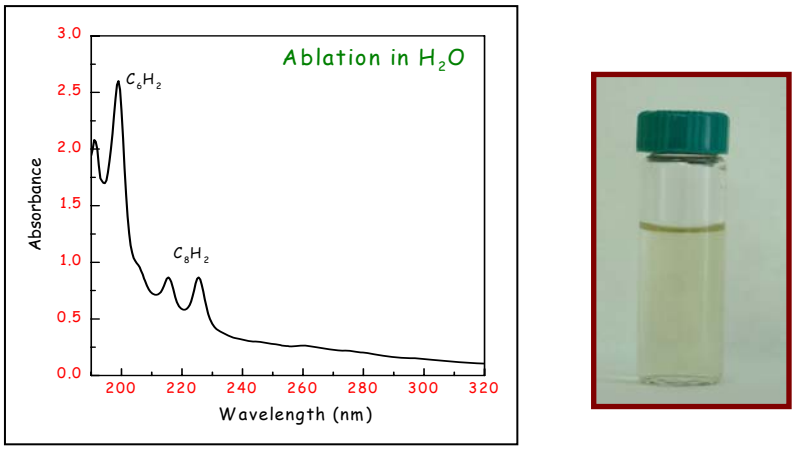

Fig.3.3: Uv-Vis absorption for different polyynes samples.

As already observed in the literature by several authors, one of the most useful indication on the structure and the bonding state of carbon-based materials comes from the study of their Raman scattering.

Furthermore, Raman spectra of the untreated and unfiltered aqueous suspension were immediately performed (fig. 3.4) to test the presence of LCCs through their characteristic and vibrational features (1700–2100 cm^{-1}).

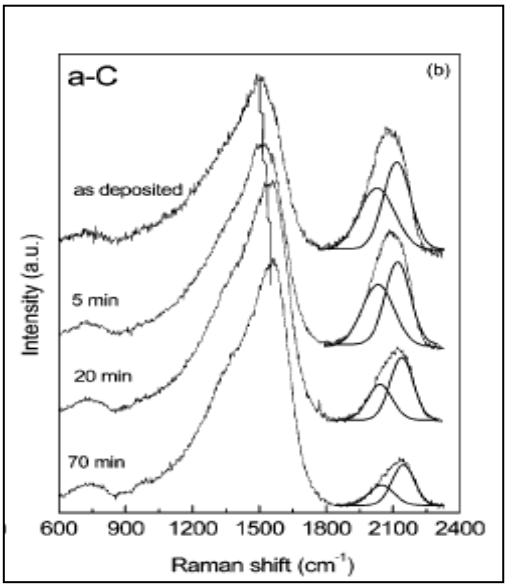

Fig.3.4: Raman spectra of the untreated and unfiltered aqueous suspension

In this figure we can see also the double structure often indicated as a convolution of D (low wavenumbers) and G (high wavenumbers) bands.
Raman spectra were excited by the 514.5 nm radiation of an Ar ion laser and analyzed by a Jobin Yvon 450 mm focal length monochromator, equipped with a CCD camera detector cooled at 77 K.
A macro-configuration was used in order to avoid heating effects of the samples with an estimated laser power density of about 100 W/cm^2.
As a matter of fact, it is quite difficult to analyze polyynes by conventional Raman spectroscopy since they are generally produced at very low concentrations.

In this way, we obtained useful SERS active systems in which a shell of carbon structures is adsorbed on the metal nanoparticle surface (M@LCC, with M = Ag, Au, Cu).

SERS spectra were recorded both in liquid solution and after deposition of a few drops of the M@LCC water solutions on a silicon monocrystalline substrate. Studies on SERS effects have already shown the influence of the employed enhancer system (nanocolloids, metal island film, or metal end-capped carbon chains) on the frequency of vibrational modes [18].

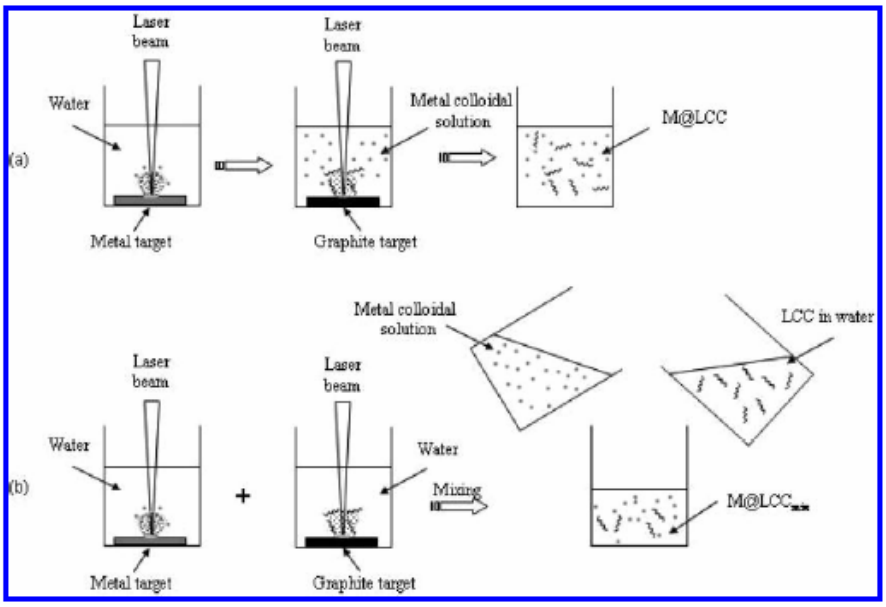

Fig.3.5:Schematic view of the experimental procedure employed for the synthesis of M@LCC (a) and M@LCC$_{mix}$ (b)

In this respect, the assignment of SER features is controversial and seems strongly dependent on the carbon-metal interactions obtained for the different systems.

To highlight the influence of the bond on the carbon chain stabilization and on the SER effect, a different preparation procedure was carried out (see Figure 3.5).

Carbon and metal (Ag, Au, and Cu) colloidal solutions were produced separately and mixed together immediately after their preparation (M@LCCmix). Raman and UV-vis spectra recorded in the presence of metal nanoparticles in water leave many uncertainties as to the presence of polycumulenic species.

Under this aspect, MS spectrometric analysis has helped us to give experimental evidence of their presence. Electrospray ionization (ESI)-MS measurements were carried out by using a Finnigan LCQ DECA XP PLUS ion trap spectrometer operating in the positive ion mode and equipped with an orthogonal ESI source (Thermo Electron Corp., USA). Sample solutions were injected into the ion source at a flow rate of 10 μL min^{-1}, using nitrogen as drying gas.

All of the experimental values of the MS parameters used for the described experiments were the same as in standard ESI-MS measurements and are reported in details elsewhere [19,20].

In summary, the mass spectrometer operated with a capillary voltage of 46 V and capillary temperature of 200 °C, while the spray voltage was 4.3 kV.

To further clarify the morphology of produced nanocomposites systems, colloidal solutions were deposited on carbon grids suitable for transmission electron microscopy (TEM) analysis (JEOL JEM 2010F).

In this section, we first describe optical spectroscopic features and TEM studies of silver, gold, and copper nanoparticles prepared by laser ablation in water. The surface morphological evolutions induced by the LCC coating obtained with two different experimental procedures are also illustrated. A coupled vibrational and MS analysis of the LCC-protected metal nanoparticles is then presented.

3.3. LCCs Prepared in the Presence of Metal Colloids (M@LCC): Aggregation and Coagulation Phenomena.

To study the metal nanoparticles and their interaction with LCCs, the extinction in the metal surface plasmon region (UV-vis) has been studied. The results are summarized in Figure 6 where three typical curves are shown for each metal/carbon produced system.

When the metal nanoparticles were not coated with a carbonaceous shell (blue lines), peaks attributed to the Ag, Au, and Cu surface plasmon resonance (SPR) located, respectively, at 402, 519, and 680 nm were observed. The spectra refer to typical optical extinctions of the corresponding metal nanoparticles.

On the other hand, features of sp-hybridized LCCs (green line in the inset of figure 3.6) dominate the ultraviolet spectral region because of electronic transitions peaking between 190 and 300 nm, with increasing wavelengths as the chain length increases. As reported [21] when a carbon target is laser ablated in water, LCCs C*n*H2 with n = 6-8 are produced. Carbon species with n = 6 have been identified by a prominent absorption feature at 200 nm (with a shoulder at 207 nm), while LCCs with n = 8 produce two weak signals at 216 and 226 nm. Both features from C_6H_2 and C_8H_2 are clearly visible in our LCCs water solution as expected.

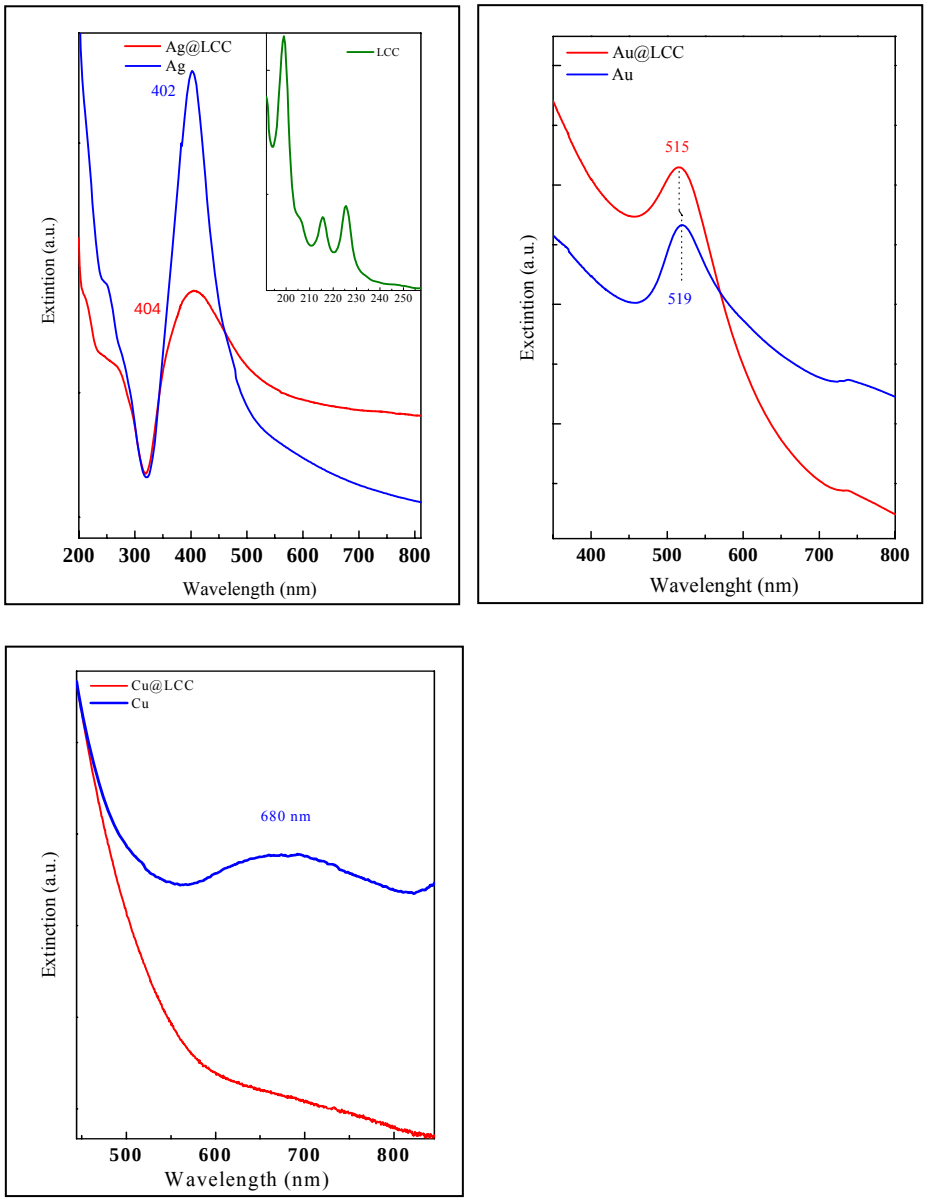

Fig.3.6:UV-vis spectroscopic observation for LCCs (green lines) M (blue lines), M@LCC (red lines), suspension.

As the metal nanoparticles were coated with a carbonaceous shell, some differences are observed in the position and the shape of plasmon absorption peaks (red lines).

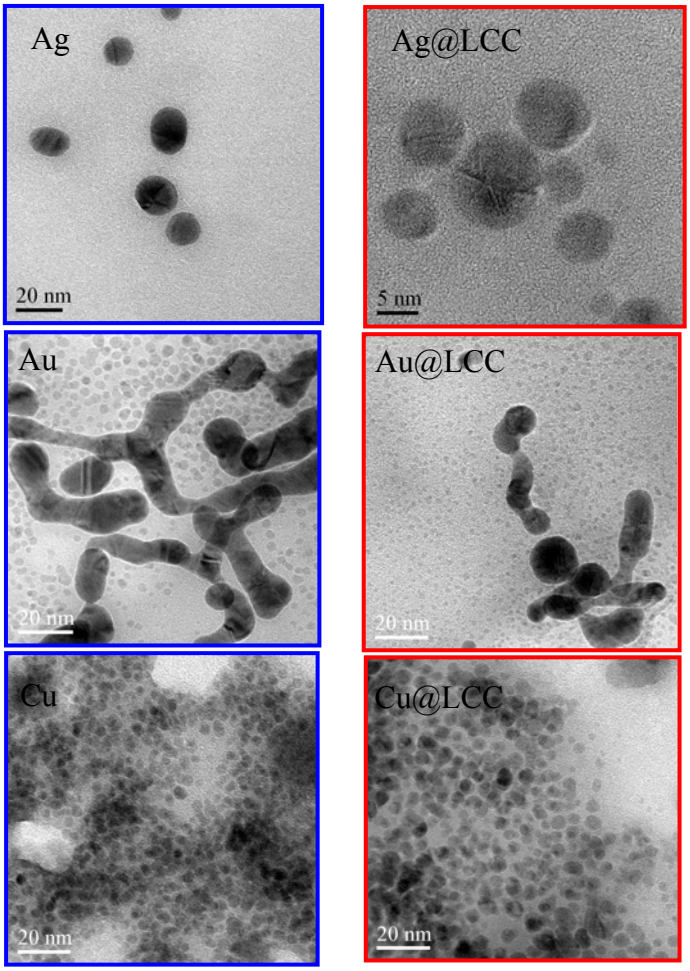

Fig. 3.7: Transmission electron micrograph of M (blue lines), M@LCC (red lines), for the three metals: Ag, Au and Cu.

First, the UV electronic transitions of carbon species were masked by the strong interband transition of metals in the range from 200 to 350 nm as already mentioned.

Furthermore, the SPR of silver nanoparticles decreases in intensity and broadens, indicating that several aggregation phenomena take place in the liquid environment.

To elucidate the effects of the interaction of metal clusters with carbon species, TEM images of the samples were performed (see Figure 3.7).

In the absence of LCCs, silver nanoparticles appeared well separated and almost monodisperse in size (diameter of ca. 10-20 nm) as supported by the position and shape of the SPR peak.

When carbon is ablated in the presence of silver colloids, nanoparticles appeared reduced in size (5-10 nm) and organized in ensembles of aggregates with interparticle distances of a few nanometers. The size reduction is possibly due to further irradiation of the solution (and/or to the presence of carbon species), while the formation of these ensembles can be ascribed to aggregation phenomena mediated by the presence of carbon species at the surface of the silver nanoparticles [22].

Unlike silver nanoparticles that appear well separated and homogeneous in size, in the case of gold nanoparticles a heterogeneous system forms (Figure 3.7): branched gold nanowires (resulting from a coagulation of particles of larger size) and small gold aggregates of different size (<10 nm) and shape (spherical and ellipsoidal are the main nanoparticles morphologies observed in the TEM image), the latter being responsible for the features observed in the extinction spectrum.

Several studies conducted by Liao et al. [23] concluded that a self-organization of gold nanoparticles into linear structures can be explained in terms of strong dipole/dipole interactions generated by an asymmetric charge distribution onto the cluster surface. The interactions are strong

enough to overcome the electrostatic repulsions between the colloidal particles [23]. In addition, Werner et al. [24] demonstrate that the laser irradiation at 532 nm of preformed gold nanoparticles in water produces positively charged Au clusters as a consequence of electron ejection and Coulombic explosions.

Positively charged nanoparticles form aggregates when interacting with pre-existent negatively charged gold particles (the ξ-potential of the water suspension is reported negative). Furthermore, the surface chemistry of surfactant-free gold nanoparticle obtained by laser ablation in water was deeply investigated by Sylvestre et al.[25] and Muto et al.[26]. It was demonstrated that surface gold atoms are oxidized (AuOH and AuO^-), and equilibrium between the neutral (AuOH) and the negatively charged species (AuO^-, ξ-potential reported of about -30 mV) exists in solution as follows [25].

$$Au{-}OH \leftrightarrow Au{-}O^- + H^+$$

Our experimental data are in accordance with a negative charge (-37 mV for free-gold nanoparticles of about 12.5 nm) on the metal nanoparticle surface. Therefore, we consider our gold colloidal suspension as composed by both neutral and negatively charged gold clusters. Neutral gold nanoparticles probably tend to aggregate in water and to precipitate after a week-long aging period. On the contrary, it is very likely that coagulation phenomena in free-silver nanoparticles are inhibited by the presence of stronger electrostatic repulsions (the ξ-potential of the silver-water suspension is still negative). However, the aggregation disappears when carbon is ablated in the solution containing gold nanoparticles as confirmed by the TEM photograph of Figure 3.7. In the latter case, Au@LCC aggregates appear homogeneous and reduced in size (5-8 nm)

as is also suggested by the blue-shift of the SPR position in the extinction spectra (Figure 3.6).

The results of the experiments performed on copper nanoparticles are reported in Figures 3.6 and 3.7.

The UV-vis absorption spectrum (Figure 3.6) of copper nanoparticles suspension (blue line) is characterized by a broadened and depressed surface-plasmon band caused by the small size of the particles.

Surface-plasmon peaks are known to decrease in intensity and width with decreasing particle diameter. Copper oxides in the metal nanoparticles can also contribute to the generation of the above-mentioned broadening and reduction in intensity of the surface-plasmon band.

TEM characterization of the copper nanoparticles was carried out to verify their metallic nature and to ascertain the influence of the carbon on the particle size. TEM images show spherical nanoclusters with fairly well-dispersed, homogeneous in size and shape, particles having a diameter ranging from 4 to 8 nm (Figure 3.7). A comparison between TEM images of Cu and Cu@LCC shows that the nanoparticles size is different: in the case of Cu@LCC, the nanoparticles are larger than in the Cu case. This could be due to the different crystalline structure formed and/or to the presence of carbon.

A fast Fourier transform (FFT) performed on several TEM images simulates the diffraction patterns and mainly reveals the presence of Cu crystalline structure, as evidenced by the diffraction spots (Figure 3.8a). In some images, traces of Cu oxide are observed (not shown here). In the case of carbon ablated in the presence of copper colloids, a similar FFT procedure shows the presence of Cu_2O as evidenced by the diffraction pattern reported in Figure 3.8b.

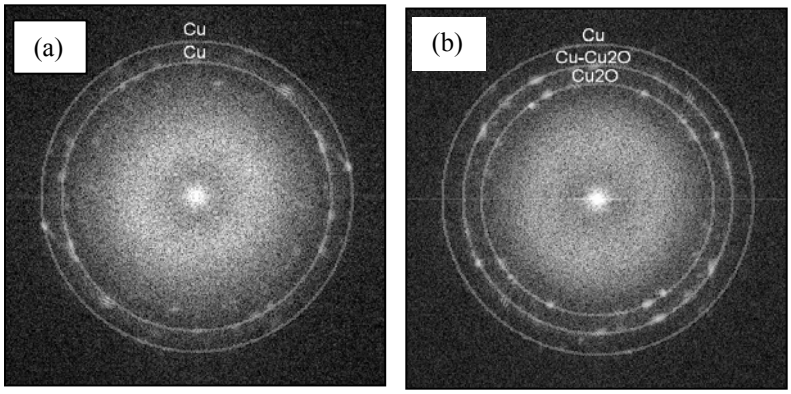

Fig.3.8:Diffraction patterns obtained by fast Fourier transform (FFT) performed on high magnification TEM images of small Cu clusters (a) and Cu@LCC systems (b)

When LCCs are obtained in the presence of copper colloids, carbon chains contributed, together with the oxide, to prevent the further oxidation of the nanoparticles by the ambient oxygen.

The absence of any signal attributable to the SPR in Cu@LCC samples is ascribed both to the formation of a carbon shell and to oxide layers.

3.4 LCCs Mixed with Metal Colloids (M@LCC$_{mix}$): Aggregation and Coagulation Phenomena.

Different core/shell structures were obtained by changing the preparation method (see figure 3.5). In summary, in this last case, the interaction between metal nanoparticles and LCCs has been obtained just by mixing formerly prepared suspensions (Figure 3.5b). The UV-vis spectra of the Ag@LCC$_{mix}$ samples (solid black line in Figure 3.9) reveal their different characteristics compared to the Ag@LCC. The extinction spectrum shows double plasmon resonance peak at 448 and 702 nm, the latter usually associated with an elongated shape of the silver nanoparticles. TEM analysis confirmed the presence of elongated silver nanoparticles of about 20 nm in length as well as silver clusters of 5 nm in diameter, similar to those obtained in the case of Ag@LCC. In this case, the coalescence was not totally suppressed by the mixing between the metals and the LCC suspensions. A quite similar behaviour was observed for gold nanoparticles in Au@LCC$_{mix}$. In particular, although the SPR (solid black line in Figure 3.9) remains quite similar, in terms of position and shape, to those detected for Au and Au@LCC, TEM analysis reproduces again the silver results, because Au@LCC$_{mix}$ some aggregation is clearly visible (Figure 3.10).

Indeed, a no complete inhibition of aggregation is probably due to the aging time of gold colloidal suspensions before mixing (about 20 min), corresponding to the irradiation time necessary to prepare LCC suspensions.

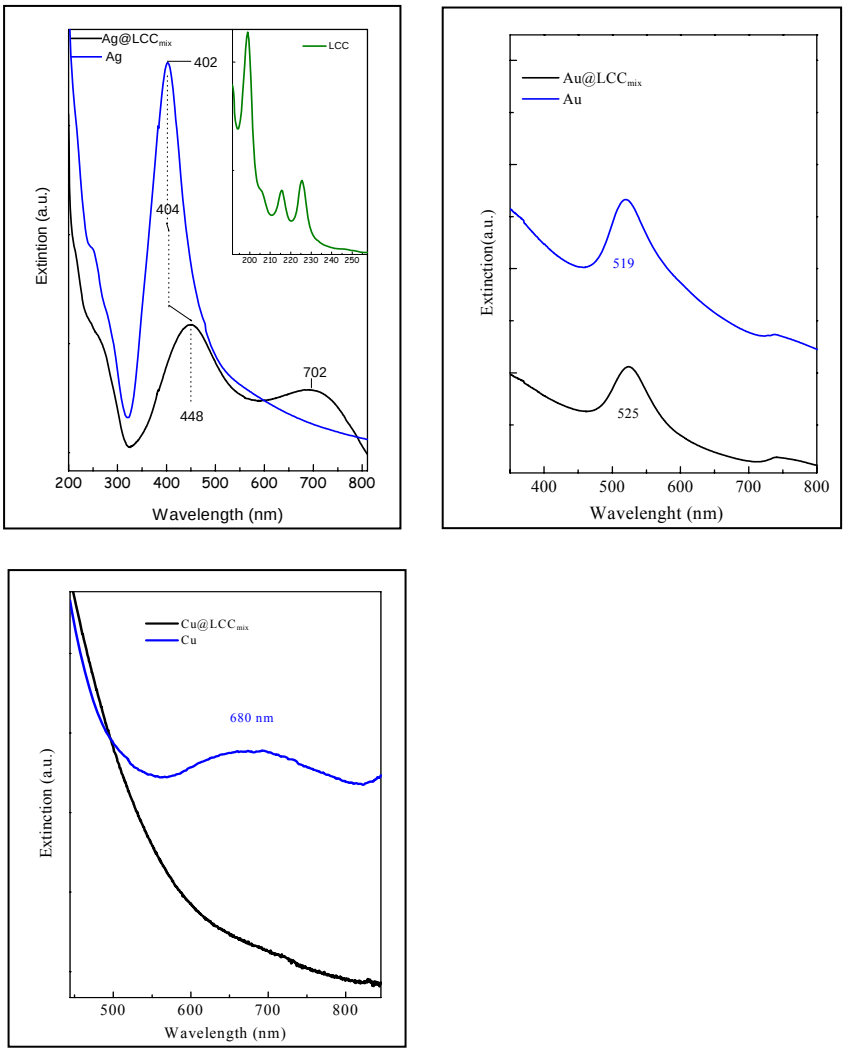

Fig. 3.9: UV-Vis spectroscopic observation for M and M@LCC$_{mix}$ water suspension. In the inset, the LCC spectrum is also reported.

In Cu@LCC$_{mix}$, when copper nanoparticles interact with carbon nanostructures, the presence of the latter and of the pre-existent copper oxide totally quenches the SPR (solid black line in Figure 3.9). In addition, TEM analysis shows that the copper colloid particles remain spherical and well dispersed (fig.3.10). Coalescence does not occur because they are well protected by copper oxide and/or carbonaceous layers.

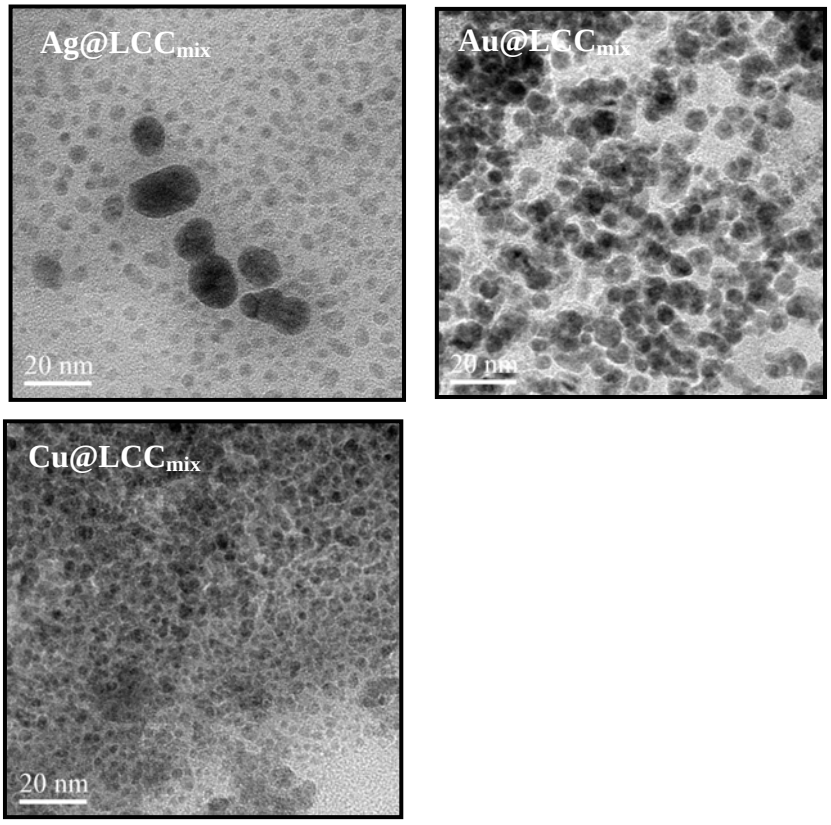

Fig.3.10: Transmission electron micrograph of M@LCC$_{mix}$ for the three metals: Ag, Au, Cu.

3.5 Raman and MS Characterization of LCC-Protected Metal nanoparticles (M@LCC and M@LCCmix)

Raman signals of LCCs are well characterized and detected by separated vibrational bands in the 1800-2100 cm^{-1} range. Figure 3.11 shows the Raman spectra of Ag@LCC (black line) and Ag@LCC_{mix} (blue line).

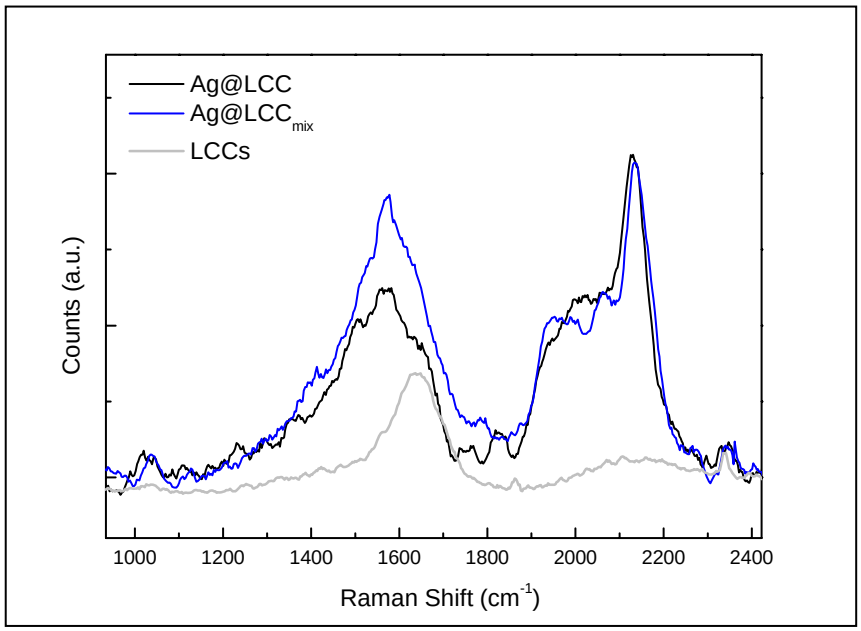

Fig.3.11: Raman spectra of LCCs in water(grey line). Solid black and blue lines represented SERS spectra, obtained in the presence of silver colloids, respectively, of Ag@LCC and Ag@LCC_{mix}

The spectrum of free-LCCs in water is also shown for comparison (grey line). Raman spectra intensities were normalized to the OH stretching

signal of water that appears between 2800 and 3800 cm^{-1} (range not shown). In the absence of silver clusters, only the OH bending (~1600 cm^{-1}) from bulk water is detectable at about 1650 cm^{-1}. When metal nanoparticles are present in the solution with LCCs, the Raman signals of the latter are enhanced by SERS effect [27]. In this case, the spectrum is composed by a broad band located between 1000 and 1700 cm^{-1}, which can be decomposed into high frequency component (the so-called G line) at around 1550 cm^{-1} and a low frequency one (the D line) at around 1360 cm^{-1}, typical of highly disordered graphite-like structures as already discussed in the literature [28,29]. In addition to the expected G and D peaks, a broad signal of almost comparable intensity, between 1900 and 2200 cm^{-1}, also appears. According to previous Raman spectroscopic studies on sp-bonded carbon species,[30-32] this signal is related to the presence of a mixture of polyynes and cumulenes. Differently from the UV-vis and TEM analysis, SERS spectra do not show any marked differences for the two coated systems in terms of vibrational peak positions (blue and black lines in Figure 3.11).

By calculating the ratio of integrated intensity of the sp (I_{sp}) and sp^2 (I_{sp^2}) contributions, a comparison in terms of sp-yield and stabilization is possible. In this respect, it is known that the integrated intensity ratio of the sp signals with respect to the graphite-like one (including both G and D lines, I_{sp^2}) is proportional to the fraction of sp and sp^2-hybridized bonded carbons as follows:

$$\frac{I_{sp}}{I_{sp^2}} = \frac{\sigma_{sp}}{\sigma_{sp^2}} \frac{x_{sp}}{x_{sp^2}}$$

Here, σsp and σsp^2 are the sp and sp^2 Raman scattering cross sections, respectively (corrected for the presence of any resonance effect), and xsp and xsp^2 are the relevant carbon atomic fractions. Both cross sections can be influenced by the structures of the graphite-like domains or by the length of the LCCs, and, consequently, σsp and σsp^2 are to be considered as averages for this specific material [34]. Moreover, due to the coincidences in the vibrational features of two samples, average cross sections of Ag@LCC and Ag@LCC_{mix} can be supposed to have the same value. Therefore, a direct comparison of the integrated intensity ratios is possible. In details, we obtained the values of 1.22 and 0.87, as I_{sp}/I_{sp}^2 ratio for Ag@LCC and Ag@LCC_{mix}, respectively.

This means that, in the case of Ag@LCC, an additional 28% of LCCs units interacts with the SERS active silver nanoclusters, and, consequently, a higher amount of LCCs is stabilized by the bond with the metal. However, for both Ag@LCC and Ag@LCC_{mix}, the amorphous carbon yield seems to be strongly limited. The Raman analysis of LCC is here restricted to the case of the interaction with silver clusters, because, in the case of gold and copper, the moderate SERS effect and the low LCC concentration did not allow any carbon detection in the liquid.

Details on the vibrational region between 1850 and 2050 cm^{-1} are very difficult to discuss. In fact, each LCC is reported to be characterized by two vibrational modes [18]: a main band (α*'* mode) at higher frequency (for LCCs containing up to 14 carbon atoms) and a less intense band (*β'* mode) at lower wavenumber. From UV-vis spectra, our samples seem to contain LCCs with a number of carbon atoms restricted to 6 and 8 (polyyne component). Thus, at least four peaks are necessary to fit our SER experimental data if Tabata's assignment [18] is to be taken into account. In details, the C_6H_2 is positioned at 2136 cm^{-1} (α*'* mode),[21] the C_8H_2 associated with a main peak [18] at 2083 (α*'* mode), and the *β'*

mode at 1943 cm^{-1} with a shoulder at 1895 cm^{-1} (the position of the C_6H_2-*β'* mode is not reported by Tabata). We want to highlight that, although systematic and accurate experimental data and density functional theory (DFT) calculations are reported in the literature for polyynes [27], the assignment of SER frequencies seems strongly dependent on the SERS enhancer interaction.

If the cumulenic contributions are also considered, SER frequencies are not well assigned in the literature, and unfortunately only one DFT calculation is available for the cumulenic species Ag_4-C_8H_2 [27]; this fact impedes a reliable assignment of the experimental features to be obtained, also due to the strong instability of the cumulenic sp configuration (polyyne species are energetically preferred because of the Peierls distortion stabilization) [32,35-36]. Furthermore, to assign several SERS frequencies in the low frequency range (1800-2000 cm^{-1}), Lucotti et al.[27] have also suggested that an interaction between silver clusters and LCCs could either tune the chain electronic properties toward the formation of cumulenic structures or favour the formation of longer polyyne linear chains, in a kind of silver surface-catalyzed polymerization.

We must note that SERS spectra in water solution appear quite weak and noisy and are therefore very different from those reported on SERS active roughened silver surface [21]. In fact, very sharp Raman lines are observed in the latter case, allowing an easier assignment of the relevant modes.

An alternative approach, commonly found in the literature to detect LCCs by Raman spectra, is to deposit a few drops of colloidal solution (M@LCC and M@LCC_{mix}) on silicon substrates and characterize them by Raman spectroscopy after solvent removal. The obtained spectra in the case of silver, gold, and copper are reported in Figure 3.12. Carbon

structures adsorbed on noble metal nanoparticles present good quality spectra.

Because SERS magnification depends on the nature of metal and excitation line, a direct comparison in terms of integrated intensity ratio (I_{sp}/I_{sp}^2) between different interacting metals is not feasible. Modifications of sp and sp^2 components observed for Ag@LCC systems from liquid to solid state are already reported elsewhere [22]. The present SERS results allow us to discuss the nature of the metal-carbon bond. The interaction of LCCs with metal clusters in M@LCC (red lines) seems to be different from the one observed in $M@LCC_{mix}$ (black lines), resulting in several differences in the vibrational features, whereas some analogies in the spectra were observed in terms of nature and strength of bond independently of the metal.

Two broad bands are commonly detected in all spectra in the 1800-2200 cm^{-1} region. We note that frequency positions and relative intensities are very different in the investigated systems, while all wavenumber values correspond to a number of carbon atoms/chains between 6 and 14.

As reported in the literature, the interaction of carbon with silver clusters after mixing results in an ordered layer on metal surface aggregates, and, in our case, it is characterized by frequency values of 1990 and 2140 cm^{-1}, typically of C_{12} and C_6 units. The presence of C_{12}, absent in liquid, can be justified by the already discussed dimerization of C_6 catalyzed by silver atoms on cluster surface [22].

The stabilization action seems more efficient for $Ag@LCC_{mix}$ systems (black line in Figure 12) where the ratio I_{sp}/I_{sp}^2 is found 4 times higher than the value obtained for Ag@LCC (red line in Figure 3.12), in sharp contrast with results obtained in liquid phase.

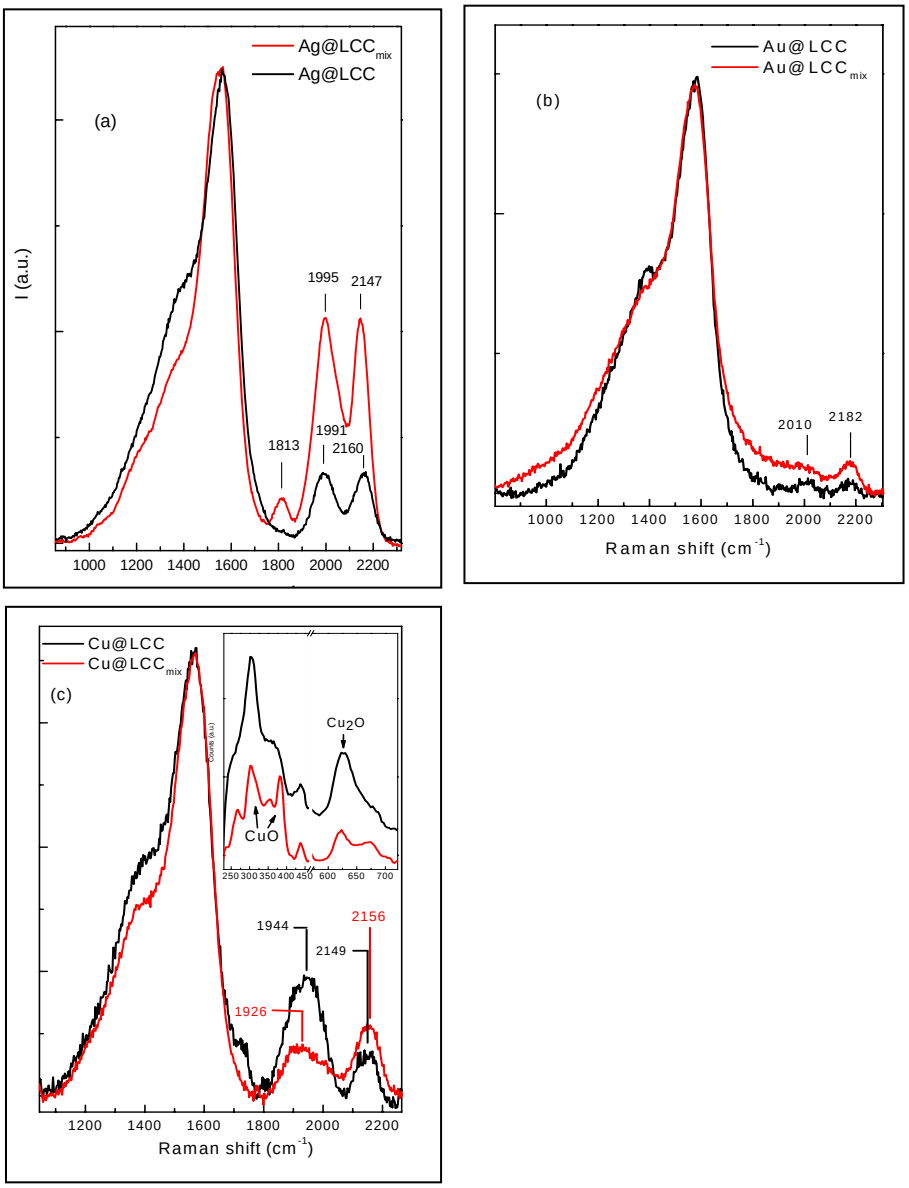

Fig.3.12:Raman spectra of M@LCC$_{mix}$ in solid state. In the inset of figure (c) vibrational features of CuO and Cu_2O are also shown.

It seems likely that LCCs appear to be more stable on larger metal clusters (observed in Ag@LCC_{mix}) than on smaller ones obtained in the Ag@LCC (d<5nm nm); moreover, a lower number of LCC units are stabilized due to the lower number of silver atoms on surface aggregates in the considered unit of volume. In both cases, not just polymerization but also a graphitization process occurs in the solid state, leading to a strong increase of the sp^2 component.

Note that amorphous carbon formation has been observed in all samples independently of the nature of metals, while sp vibrational features are different in terms of position and relative intensity. While the role of silver in the interaction with LCCs is widely reported in the literature, the stabilization operated by gold and copper nanoparticles bonded to LCCs has not been fully investigated. The SER spectra for gold systems have been obtained by using the same excitation wavelength of 514.5 nm as for the other metals. However, such wavelength produces a weaker Raman enhancement for gold nanoparticles than for silver ones, and this causes the decreased intensity of the two sp-bands (2010 and 2182 cm^{-1}) observed in the Au-LCC samples (Figure 3.12). The sp-signals are very low also if compared to the sp^2 components, suggesting that on gold surfaces the LCC-Au interactions are not as efficient as for silver.

Note that, as expected for polyyne frequencies, a weak LCC-metal interaction leads to a low SER effect; as consequence, the 2182 cm^{-1} vibrational band, in both Au@LCC and Au@LCC_{mix}, can be associated with the normal Raman of the C_6H_2 chain. This frequency usually is shifted by about 40 cm^{-1} toward lower wavenumbers in silver samples, where the SER effects are present [21]. It is already reported [33] that the correlation between the overall sp signals and the graphite-like band is of fundamental importance to measure the conversion of cumulenes and polyynes into graphene-like species. In the absence of a metal end-

capping stabilization, LCCs tend to react and crosslink toward sp^2 hybridizations, leading to the vibrational features observed in the Raman spectra of Figure 3.12. This fact is not surprising because the interaction requires metal cations that are more difficult to be obtained in the case of gold. In addition, the presence of the negative charge on nanoparticle surface could contribute to an electrostatic repulsion between highly conjugated sp-systems and AuO^- species on the gold metal surface.

A thorough Raman characterization of copper polyynides and carbynoids structures copper bond end is reported by Cataldo [37,38]

He found a Raman spectrum characterized by a stronger band at lower wavelength followed by a weaker band at higher frequency. In view of the detected frequency values, Cataldo associated the two bands with the presence of triple bond stretching and cumulenic forms, whose formation derives from the presence of oxidized copper atoms at chains ends. Because of the coincidence of some frequency values (1944 and 2156 cm^{-1}) reported in Figure 3.12 (red line), we can also suppose the presence of cumulenic species. Moreover, by comparing silver and copper systems, we observe sp-vibrational features of Cu-LCC at lower frequency than for Ag-LCC.

This is clear evidence of a different size distribution of LCC and of the possible presence of cumulenic species in Cu samples, usually detectable around 1900 cm^{-1}. Note that the presence of copper oxides was detected in both Cu samples by low intensity Raman vibrational bands in the range 200-700 cm^{-1} (see inset of Figure 3.12c).

It has been already reported by our group that it is possible to obtain important information by MS on the kind of carbon species produced by PLA in water containing Ag nanoparticles [22].

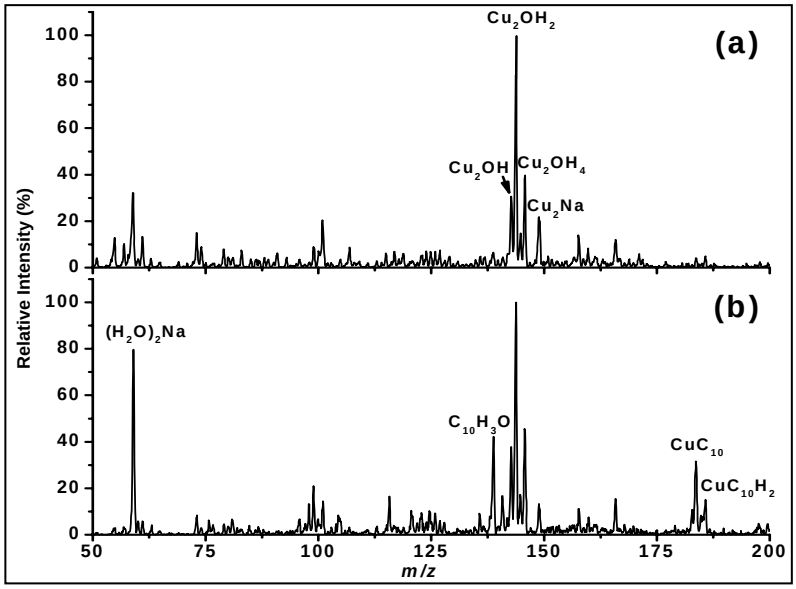

Fig.3.13:ESI positive ion mass spectra obtained for solutions containing Cu nanoparticles (a) and Cu@LCC (b) obtained as described in the text. In (a) four peaks are assigned and they are characteristic for Cu species generated by the Cu nanoparticles. In (b) LCCs with 10 carbon atoms are also detected and have been assigned to polyynic and polycumulenic species.

MS investigations are here restricted to the analysis of Cu and Au samples, whereas a deep study for silver systems has been reported elsewhere [22]. It must be pointed out that, in the case of investigated LCC-silver samples, ions containing Ag were not detected by MS, and LCCs were the only species responsible for all of the peaks detected in the mass spectra.

On the other hand, in the case of Cu nanoparticles alone, some Cu species are detected by ESI-MS as reported in Figure 3.13a.

Furthermore, after PLA of the graphite rod, three more species attributed to LCCs are also detected for the system Cu@LCC, as reported in Figure 13b. These peaks were assigned to the presence of LCCs with 10 carbon atoms. Particularly, the low mass signal rises from the hydrated polyynic species, while the two species at higher *m*/*z* values have been assigned to the polyynic CuC_{10} and polycumulenic $CuC_{10}H_2$ species with an oxidized copper at the end of the chain. It is not possible to infer the total absence of different LCCs in Cu@LCC solution as it could derive from poor ionization efficiency that could hinder their detection.

However, it is reasonable to expect a similar ionization efficiency for the different LCCs and, therefore, to assume from the above-reported MS results that the C_{10} species are the most abundant species in Cu@LCC solutions.

In the case of Au@LCC, the following information could be obtained from Figure 3.14.

More species than in the case of Cu@LCC could be detected, ranging from C_6 to C_{11}. The species containing 6 and 8 carbon atoms seem to be more abundant than others, thus confirming what has been found by UV measurements.

At the soft experimental conditions applied for the ionization, we exclude possible fragmentations of LCCs; therefore, the detected species containing an odd number of C atoms (7,11) can be attributed to cumulenes.

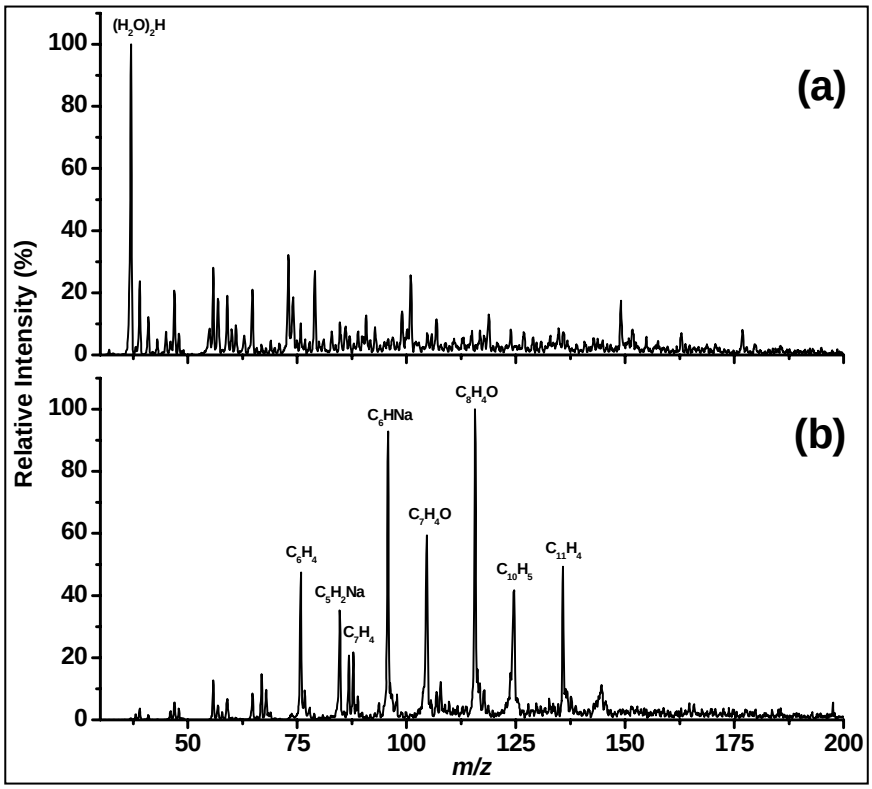

Fig. 3.14: ESI positive ion mass spectra obtained for solutions containing Au nanoparticles (a) and Au@LCC (b) obtained as described in the text. In (b) the LCCs are detected also in combination with Na or oxygen atoms. Discussion is in the text.

Indeed, they appear either with a high number of H atoms or in complex with other atoms (Na, O), in accordance with a cumulenic structure. This fact contributes to a further complication in the fit-analysis of the SERS

spectrum, due to the lack of any correct frequency assignment for cumulenic species of different chain lengths.

The species containing 10 carbon atoms are also detected, even if to a minor extent.

The last point is of particular importance, as in Raman spectroscopy LCCs consisting of 6 or 8 carbon atoms are often indistinguishable from each other. Our MS approach thus allows the direct detection of the length of LCCs, obtaining a very clear indication that the LCCs containing 6 carbon atoms are much more likely to predominate in our experimental conditions for Au@LCC.

In the case of M@LCCmix, the MS results did not provide any useful information because the intensities of the detected species were too low for a meaningful analysis. Such result is in accordance with the previous findings obtained by the other analytical techniques. Indeed, in M@LCCmix, LCCs appear to be more stable than on M@LCC, whereas a lower number of LCC units are stabilized due to the lower number of metal atoms on surface aggregates in the considered unit of volume.

The interaction between LCCs and different metals (Cu, Au, Ag) was investigated to provide an insight into the factors influencing chemical (reactivity) and physical (optical) properties of the metal/LCCs core/shell systems produced at various experimental conditions. For this purpose, a range of different complementary experimental techniques such as Raman and UV-vis spectroscopy, TEM, and MS was employed.

Surfactant-free metal nanoparticles (Ag, Au, Cu) and metal/ LCC (core/shell) structures were prepared by PLA of bulk materials in water. It was found that while silver and copper nanoparticles are very stable in water, due to the presence of a partial oxidation of metal surface (stronger for copper and in minor extent for silver), in the absence of the outer LCC shell, a strong interparticle coalescence in colloidal gold

suspensions was detected by TEM analysis. On the contrary, in the presence of LCC shells, metal nanoparticles result to be extremely stable and almost monodisperse in size (~5 nm). An accurate characterization of the carbon shell and a study of the interactions between LCCs and metal nanoparticles were performed by coupling SERS and MS. While in Ag@LCC samples a direct bond was evidenced between silver and LCCs, in Cu@LCC the interaction probably occurs between LCC and Cu oxides.

In both cases, produced carbon species were very stable in water and were well characterized by MS analysis. In the case of gold, although we were not able to detect a direct Au-C bond, the presence of LCCs totally suppresses coagulation phenomena, as evidenced by TEM analysis. Further work on this matter is in progress.

This study has shown that water PLA technology is a simple and versatile method to produce core-shell structures. Produced LCC-metal nanoparticles form a class of new materials that are likely to have many new applications in the field of electro-optical devices for catalysis or in the biomedical area.

3.6 SERS Hot-spots

In the last few years the growing interest for "plasmonics", even due to the possibility to produce surfactant-free nanoparticles by pulsed laser ablation in liquid [39] (PLA) has led to the development of new "nano-photonic" concepts with applications in extremely advanced fields [40]. Recent experimental and theoretical works on electromagnetic amplification phenomena allowed to amplify non-linear optical processes such as single molecule surface enhanced Raman scattering (SM-SERS) of molecule located in close proximity of suitable plasmonic structures (so called hot-spot). SM-SERS was observed for the first time in 1997 by Nie [41] and Kneipp [42] and immediately has attracted the attention of scientists for application in ultra-sensitive Raman analysis [43]. This is particular interesting because enables the detection of very low concentration species (down to 10^{-9} M)[44] and at the same time to give chemical information through the knowledge of their vibrational features. Several works reported for single molecule detection enhancement signal factors of about 1014 as result of strong electromagnetic (EM) field enhancement in the region between two nanometric spaced metal nanoparticles and electronic resonances of dye molecules[45]. Recently this value was estimated by Won-Hwa Park et al., for an off-resonant molecule interposed between Au films and Au nanoparticles, in a more moderate factor (10^6-10^8) as sum of the two contribution EM and charge transfer (CT), however enough to detect the single molecule. Due to the fact that this value can be frequently recorded experimentally on more traditional SERS substrates such as dimers or nanoparticles aggregates, the authors concluded that no additional molecular electronic enhancement is necessary to detect single molecules. These observations,

together with the possibility to modify peculiar optical, electronic and magnetic properties of metal nanoparticles controlling aggregation phenomena [46] still stimulate scientific attention.

Noble metal nanoparticles are well known for their intensifying effect on electromagnetic field, so constituting SM-SERS hot-spots.

DDA calculations [47] have demonstrated that the electro-magnetic field enhancement in silver dimers used as SM-SERS hot spots depends on the distance between nanoparticles and that the maximum electromagnetic field has been found for nearly touching nanoparticles. In the same work, Camden et al. reported also that SM-SERS present only a slight dependence on excitation wavelength, that is higher at the maximum of the extinction peak with an enhancement factor of 10^9, but maintaining a value of 108 throughout the visible spectrum.

In figure 3.15 we have plotted SERS spectra excited at 514.5 and 632.8 nm either for LCCs-Ag@532nm and LCCs-Ag@1064nm samples. In accordance with Raman spectroscopic studies on sp-bonded carbon species,[48] detected in the region 1800-2150 cm^{-1} are related to the presence of a mixture of polyynes and cumulenes with a number of atoms per chain (n) $6<n<14$. In addition to the sp vibrational features a broad band located between 1000 and 1700 cm^{-1} was detected, which can be decomposed into a high frequency component (the so called G line) at around 1550 cm^{-1} and a low frequency one (the D line) at around 1360 cm^{-1}, typical of highly disordered graphite-like structures as already discussed in literature [29,30].

As previously mentioned, Park et al.[49] have demonstrated that the enhancement factor due to electromagnetic field is of 10^5, while enhancement due to charge transfer between probe molecules and nanoparticles is of about 101, with the amplification of a restrict number of modes.

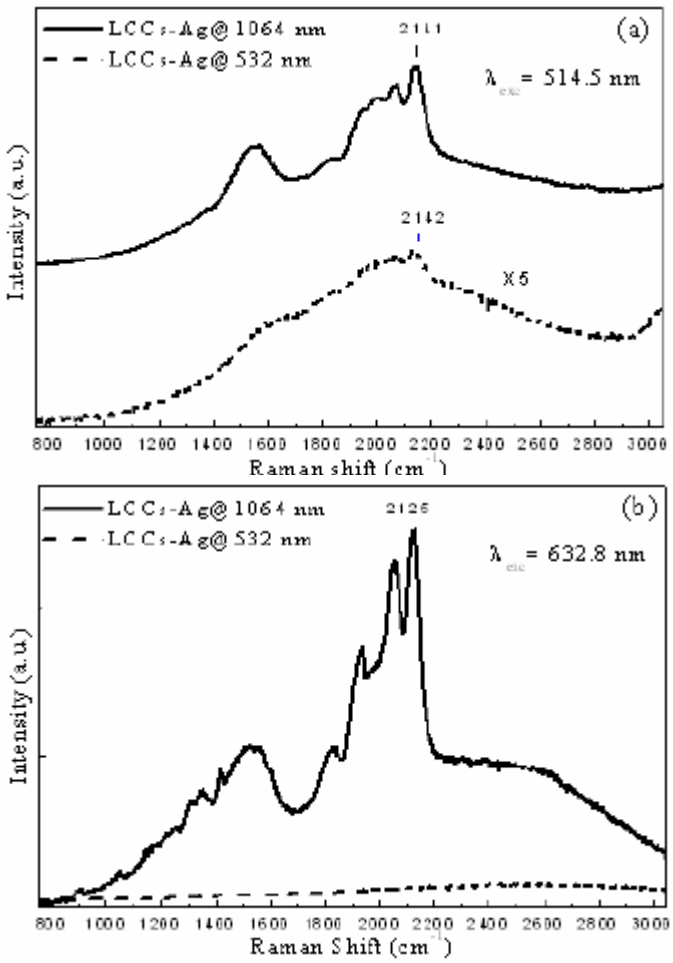

Fig.3.15: SERS spectra of LCC-Ag@1064nm(solid line) and LCCs-Ag@532 nm(dashed line) obtained with (a) Argon (b) He-Ne lasers.

In figure 3.15a a comparison between signals of hybrid LCCs-Ag system excited by the 514.5 nm laser line (in resonance with SPR) indicates that LCCs-Ag@1064nm peaks have an intensity about 35 time higher than

the LCCs-532nm ones. This value is comparable to that reported from Park for CT enhancement. Thus, both mixed systems present electromagnetic field enhancement, but only the LCCs-Ag@1064nm presents a charge transfer enhancement, and signals of one order of magnitude larger were detected. It is well known that charge transfer mechanisms are feasible only when the distance between the probe molecule and the SERS surface is below 0.2nm.

Due to the presence of silver oxides on particle surfaces in Ag@532nm samples (XPS results of previous chapter), the interaction with LCC molecules is almost impeded and the interaction resulted very weak. Therefore only the EM field amplification at longer distance is possible. Whereas Raman signals of LCCs in LCC-Ag@1064nm strongly bonded to silver nanoparticles with a more "clean" surface will be powerfully intensified. Raman spectra obtained with 632.8 nm exciting wavelength (figure 3.15b) shows that only the spectrum of LCCs-Ag@1064nm present the sp carbon signals between 1800 and 2100 cm^{-1}, that do not appear at all in the other one sample. Signals of LCCs-Ag@1064nm sample obtained with 632.8 nm excitation wavelength present a higher intensity respect to that obtained with the 514.5 nm, ascribed to the nearer position of the exciting line to a second maximum in the extinction spectrum. In the case of LCCs- Ag@532nm excited with 632.8 nm, off-resonance Raman conditions (far from the SPR peak) were achieved, thus not allowing the detection of any sp-carbon chains vibrational feature. So data deriving from SERS demonstrate that only Ag@1064nm systems are useful to create "hot spots" because of the peculiar self-assembling with LCCs.

In this paragraph has been demonstrated that the laser irradiation wavelength (532nm and 1064nm) strongly influences surface properties in PLA-prepared silver nanoparticles. As evidenced by XPS analysis

(previous chapter), while 1064 nm silver NPs are resulted almost oxide-free, the higher amounts of silver oxides mixed to metallic silver in Ag@532nm samples, are responsible of the limited interaction with the LCCs units. Moreover, the different chemical surface state results in a dissimilar self assembling behaviour after LCCs interaction. Surface enhanced Raman scattering (SERS) was applied to demonstrated the presence of "hot spots" between plasmon coupled silver nanoparticles. Observed Raman enhancements on LCCs-Ag@1064nm are resulted of 10 times higher than LCCs-Ag@532nm, due to additional charge transfer mechanisms . Our SERS results, even if in accordance with the great amplification behaviour reported in literature for hot-spot silver dimers, are significantly scaled to respect to the 10^5 orders of magnitude observed by Park et al.[49] Due to the lack of a deep knowledge in the electromagnetic amplification mechanisms involved in the hot spot regions further work on this matter is in progress.

References

[1] *Thin solid films* (1979), **58**(1), 107-116.
[2] Proc. of the Inter. Conf. on Lasers (1994), **16**H, 63-67.
[3] *Solid State Communications* (1992), **84**(4), 371-373.
[4] Diamond and related materials (2004), **13**(4-8), 661-665.
[5] Wang, J.B.; Zhang, C.Y.; Zhong, X.L. and Yang, G.W., *Chem. Phys. Lett.* (2002), **361**(1,2), 86.
[6] Guo, T.; Nikolaev, P.; Thess, A.; Colbert, D.T. and Smalley, R.E., *Chem. Phys. Lett.*, (1995), **243**(1,2), 49.
[7] *Appl. Phys. A:* (1999), **69** (suppl.), S755-S758.
[8] *Nature* (London , United Kingdom) (1985), **318** (6042), 162-163.
[9] Berichte der Bunsen-Gesellschaft (1993), **97**(2), 252-254.
[10] Carbyne and AQ1 Carbynoid Strucutures. Kluwer: Dordrecht, (1999).
[11] *Chem. Phys.* (2005), **309**, 77.
[12] Yang ,S. and Kertesz, M., *J. Phys. Chem. A* (2006), **110**, 9771.
[13] Planet. Space. Sci. (2003), **51**, 1017.
[14] Irle, S.; Zheng, G.; Wang, Z. and Morokuma, K., *J. Phys. Chem. B* (2006), **110**, 14531.
[15] Nishide, D.; Dohi, H.; Wakabayashi, T.; Nishibori, E.; Aoyagi, S.; Ishida, M.; Kikuchi, S.; Kitaura, R.; Sugai, T.; Sakata, M. and Shinohara, H., *Chem. Phys. Lett.* (2006), **428**, 356.
[16] Feng, Y.; Feng, W.; Noda, H.; Sekino, T.; Fujii, A.; Ozaki, M. and Yoshino, K., *Carbon* (2007), **45**, 2445.
[17] Cataldo, F., *Carbon* (2004), **42**, 129.
[18] Tabata, H.; Fujii, M.; Hayashi, S.; Doi, T. and Wakabayashi, T., *Carbon*, (2006), **44**, 3168.

[19] Grasso, G.; D'Agata, R.; Rizzarelli, E.; Spoto, G.; D'Andrea, L.; Pedone, C.; Picardi, A.; Romanelli, A.; Fragai, M. and Yeo, K.J., *J. Mass Spectrom.*,(2005), **40**, 1565.

[20] Grasso, G.; Fragai, M.; Rizzarelli, E.; Spoto, G.; Yeo, K.J., *J. Am. Soc. Mass Spectrom.*, (2007), **18**, 961.

[21] Compagnini, G.; Mita, V.; Cataliotti, R.S.; D'Urso, L. and Puglisi, O., *Carbon* (2007), **45**, 2456.

[22] Grasso, G.; D'Urso, L.; Messina, E.; Cataldo, F.; Puglisi, O.; Spoto, G. and Compagnini, G., *Carbon* (2009), **47**, 2611.

[23] Liao, J.; Zhang, Y.; Yu, W.; Ge, C.; Liu, J.and Gu, N., *Colloids Surf. A*, (2003), **223**, 177.

[24] Werner, D.; Hashimoto, S.; Tomita, T.; Matsuo, S.and Makita, Y. *J. Phys. Chem. C*, (2008), **112**, 16801.

[25] Sylvestre, J.P.; Poulin, S.; Kabashin, A.V.; Sacher, E.; Meunier, M.and Luong, J.H.T.,*J. Phys. Chem. B*, (2004), **108**, 16846.

[26] Muto, H.; Yamada, K.; Miyajima, K. and Mafune´, F., *J. Phys. Chem. C*, (2007), **111**, 17221.

[27] Lucotti, A.; Tommasini, M.; Del Zoppo, M.; Castiglioni, C.; Zerbi, G.; Cataldo, F.; Casari, C.S.; Li Bassi, A.; Russo V.; Bogana, M. and Bottani C.E., *Chem. Phys. Lett.* (2006), **417**, 78.

[28] Compagnini, G. and Calcagno, L., *Mater. Sci. Eng. Rep.* (1994), **13**, 193.

[29] Ferrari, A.C. and Robertson, J., *Phys. Rev. B.*, (2000), **61**, 14095.

[30] D'Urso, L.; Compagnini, G.; Puglisi, O.; Scandurra, A. and Cataliotti, R.S., *J. Phys. Chem. C.*, (2007), **111**, 17437.

[31] Kastner, J.; Kuzmany, H.; Kavan, L.; Dousek, F.P. and Kurti, J. *Macromolecules*, (1995), **28**, 344.

[32] Kertesz, M.; Koller, J. and Az´man, A., *J. Chem. Phys.* (1978),**68**, 2779.

[33] D'Urso, L.; Compagnini, G. and Puglisi O., *Carbon* (2006), **44**, 2093.

[34] Springborg, M. and Kavan, L., *Chem. Phys.* (1992), **168**, 249.

[35] Karpfen, A., *J. Phys. C: Solid State Phys.* (1979), **12**, 3227.

[36] Rice, M.J.; Phillpot, S.R.; Bishop, A.R. and Campbell, D.K., *Phys. Rev. B* (1986), **34**, 4139.

[37] Cataldo, F. and Casari, C.S., *J. Inorg. Organomet. Polym.*, (2007), 641.

[38] Cataldo, F., *J. Raman Spectrosc.* (2008), **39**, 169.

[39] Compagnini, G. ; Scalisi, A.A. and Puglisi, O., *J. Mat. Res.* (2004), **19**, 2795.

[40] Ohtsu, M.; Kobayashi, K.; Kawazoe, T.; Sangu, S. and Yatsui, T., *Quantum Electron.* (2002)**, 8**, 839.

[41] Nie, S. and Emory, S.R., *Science* (1997), **275** , 1102-1106

[42] Kneipp, K.; Wang, Y.; Kneipp, H.; Perelman, L.T.; Itzkan, I.; Dasari, R.R. and Feld, M.S., *Phys. Rev. Lett.* (1997), **78**, 1667-1670.

[43] Kneipp, K.; Moskovits, M. and Kneipp, H., Surface-Enhanced Raman Scattering: Physics and Applications Springer: Berlin, Heidelberg, New York, (2006).

[44] Stranahan, S.M. and Willets, K.H., *Nano Lett.* (2010)**, 10**, 3777.

[45] Weiss, A. and Haran, G.J., *J. Phys. Chem. B* (2001), **105**, 12348

[46] Optics Communications (2003)**, 220**, 137–141

[47] J. Phys. Chem. C (2008), **112**, 16801–16808

[48] Camden, J.P.; Dieringer, J.A. ; Wang, Y.; Masiello, D.J.; Marks, L. D.; Schatz, G.C. and Van Duyne, R.P., *J. Am. Chem Soc*. (2008), **130**, 12616.

[49] Park, W.H. and Kim, Z.K., *Nano letters* DOI:10.1021/nl102026p

4 OPTICAL TWEEZERS

Understanding the properties and extend the handling strategies for plasmonic structures of different size and shape is nowadays of primary importance for basic and applied research as well as for modern Technology[1]. Electronics, photonics, catalysis and bio-medicine are among the most relevant research fields in which metal colloids as well as ordered nanoparticle arrays are employed either macroscopically or at the nanometer scale [2]. Due to such an increasing request, researchers are continuously stimulated to find new solutions and develop original strategies for the production, isolation and control of such intriguing nano-objects[3-8]. Moreover aggregation among metal particles in colloidal systems offers the opportunity to study fundamental aspects in surface-enhanced Raman spectroscopy (SERS)[9,10] and in plasmonics[2] since rough or fractal surfaces give a strong coupling of the single particle induced electric field, generating the so called “hot spots” [9-11]. The possibility to isolate individual aggregates gives the opportunity to perform the analysis or the amplification on clusters of specific selected optical and electric properties.

Optical tweezers[12] (OT), tools for the trapping and manipulation of micro[13,14] and nanoparticles[15-20], have led to a real optical revolution[14] in physics, chemistry, material sciences and biology. When used as a force transducer, OT can measure forces at the

femtonewton[15,17], their recent integration with Raman spectroscopy (Raman Tweezers) allowed for ultra-sensitive chemical-physical analysis of trapped particles[21]. OT have been used to hold and manipulate individual metal nanoparticles since the pioneering work of Svoboda and Block[22]. Light forces scale with particle volume[15,22], hence manipulating nanoparticles with optical tweezers is generally difficult, because brownian motion can easily overwhelm the trapping forces. On the other hand the occurrence of plasmon resonances in metal nanoparticles is the key for enhancing light forces that can stably hold particles as small as 10-20 nm in size[23-29]. However only a specific size range has been shown to be trappable in optical tweezers because spherical particles with a size larger than 250 nm have increased absorption that pushes them out of the confining light field [23,28,29]. Metal aggregates have been qualitatively shown to be influenced by optical forces [19,30,31], but this has been demonstrated close to a surface where radiation pressure is neglected and in extreme experimental conditions in the presence of laser-induced heating[30,31]. Here we measure optical forces on functionalized gold nanoaggregates with controlled extinction properties and different average radii in the 20-750 nm range, obtained by laser ablation in liquid, showing how optical trapping efficiencies are enhanced 50 times with respect to forces measured on individual gold spherical particles. We also develop a full electromagnetic theory of optical trapping of metal nanoaggregates, showing how aggregation yields increased forces and wider trapping size range with respect to individual metal nanoparticles.

4.1 Optical trapping

Plasmonic nanostructures with controlled extinction properties have been obtained via a three step procedure. In the first step, gold nanoparticles (AuNPs) with average diameter of 35 nm were produced in water by Laser Ablation Synthesis in Solution (PLAL), according to the protocol[32,33] sketched in figure 4a, consisting in the laser ablation (1064 nm, 9 ns, 10 Hz laser pulses) of a pure gold target (99.99%) dipped in a solution of bi-distilled water [32].

PLAL is a "green" method that does not require any chemicals or other stabilizing agents because so obtained AuNPs have a negative surface charge due to partial surface oxidation (about 5% of surface atoms) and form a colloidal system indefinitely stable in time34.

In the second step, we added variable amounts of pyridine to three different AuNPs solutions to promote particles aggregation (fig. 4.1a).

Pyridine is known to bind gold surface through the nitrogen lone-pair electrons, promoting particles aggregation[35,36]. The stability of the colloidal system is dependent on the pyridine concentration, with larger amounts of pyridine corresponding to larger particle aggregation[35,36].

In the third step, the aggregation process was frozen by adding bovine serum albumin (BSA) to the AuNPs aggregates (AuNPAs in the following) 30 minutes after pyridine addition, exploiting the high conjugation ability of BSA for AuNPs obtained by PLAL [32].

UV-visible spectra (Figure 4.1b) of the four AuNP solutions show that a sharp absorption band at 525 nm is observed for non aggregated spherical AuNPs (Sample 1) and that a second red shifted band appears in Samples

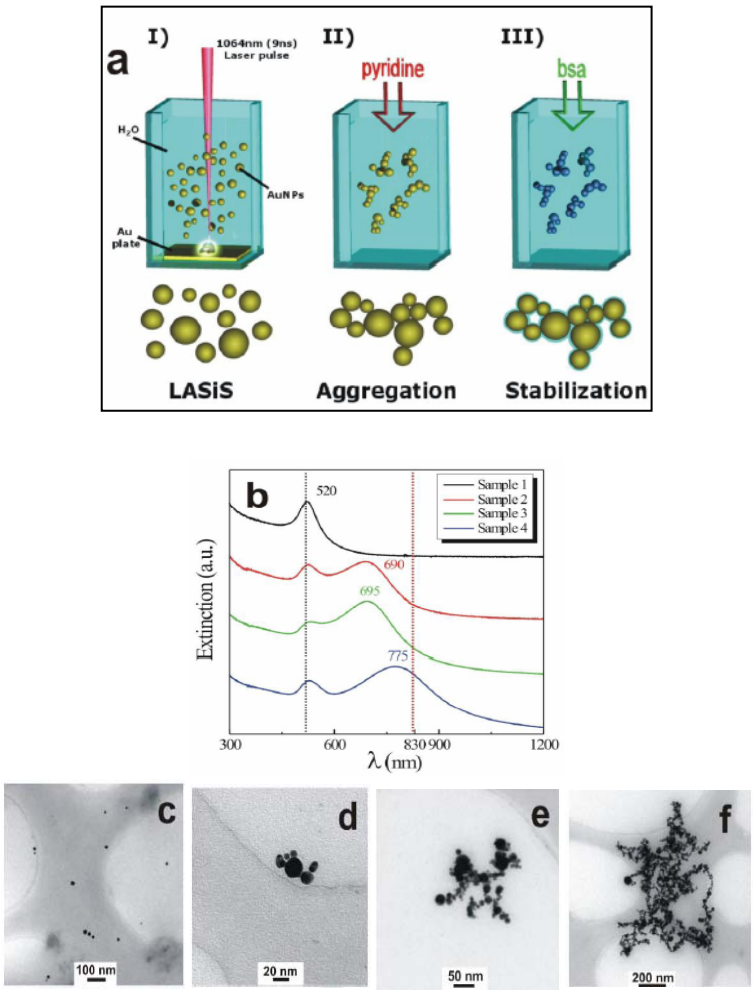

Fig. 4.1: (a) Sketch of the three step procedure for the preparation of AuNPAs: I) PLAL; II) aggregation with pyridine; III) stabilization with BSA. (b) Extinction spectra for the different samples of gold nanoaggregates obtained by laser ablation in water. Sample 1 (black line) is composed of individual nanoparticles with no aggregation. Sample 2 (red line), Sample 3 (green line) and Sample 4 (blue line) are obtained by adding increasing amounts of pyridine to AuNPs solutions. (c-f) TEM images taken for non aggregated AuNPs (c - Sample 1) and for AuNPAs with different aggregation levels (d: Sample 2; e: Sample 3; f: Sample 4), corresponding to different average sizes of aggregates.

2, 3 and 4, that is a clear indication that particles aggregation took place [9]. UV-vis spectra show that aggregation was larger for larger amounts of pyridine added to AuNPs, since a larger red shift and a larger optical density of the second plasmon resonance band are observed going from Sample 2 to Sample 4. Therefore, controlling particles aggregation is a simple way to control the plasmonic properties of such gold nanostructures. We have used transmission electron microscopy (TEM) for investigating the structure of the AuNPAs in Samples 1, 2, 3 and 4. TEM images show spherical nanoparticles with average size of about 35 nm before aggregation (Sample 1), and fractal structures with average size of ~90 nm, ~250 nm, ~750 nm for the aggregated Sample 2, 3 and 4 respectively.

Representative TEM images of the four samples are reported in Figure 1c-f (see also Supplementary Information). The fractal structure of the clusters is typical of Diffusion Limited Aggregation (DLA) processes[37].

Optical trapping is obtained in an experimental set-up with an inverted configuration[17,19], i.e. the trapping laser propagates upwards (fig. 4.2a)**.** The light from a near-infrared laser diode (830 nm) is focused by an microscope objective with a high numerical aperture (NA=1.3) in a sample chamber. The available maximum power at the sample is about 32 mW, but during force measurements of optically trapped AuNPAs it was limited to 15 mW.

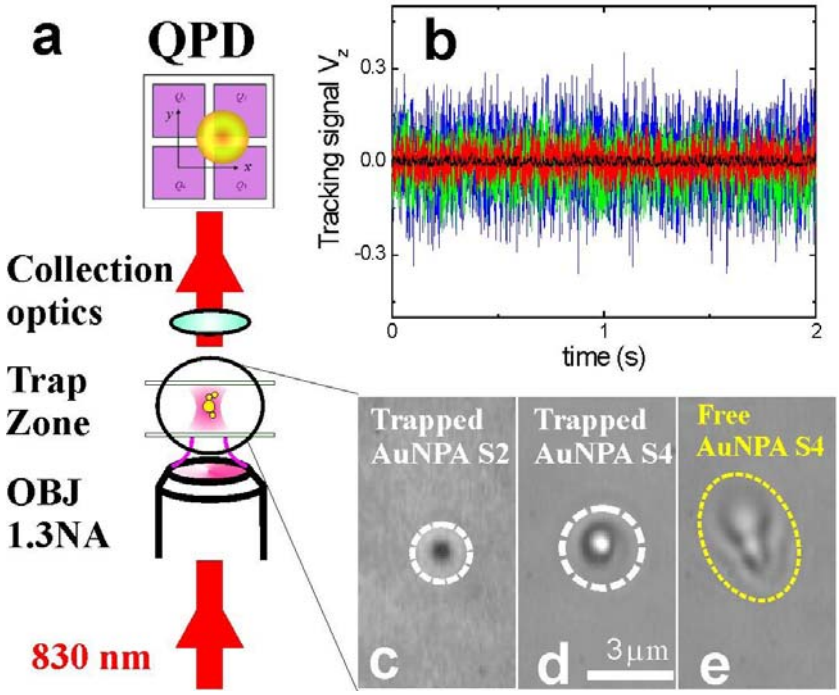

Fig. 4.2: (a) Sketch of the optical trapping setup. A NIR laser beam is focused by a 1.3 NA oil immersion microscope objective. Particles are trapped in a water dispersion were AuNPAs are produced by PLAL. The scattered light from the trapped particle is detected by a QPD through a collection optics yielding electrical signals proportional to the particle displacements. (b) Tracking signals as acquired from the QPD for a trapped AuNP from Sample 1 (black trace), a trapped AuNPA from Sample 2 (red trace), Sample 3 (green trace) and Sample 4 (blue trace). (c-e) CCD images of optically trapped AuNPAs from Sample 2 (c) and Sample 4 (d). In (c) the size of the nanoaggregate is smaller than the diffraction limit of the imaging system. In (d) the nanoaggregate is aligned with the propagation axis having an extent of about 2 μm. This is revealed when the laser is switched off (e) and the same aggregate is untrapped and free floating away from the trap.

In fact, when using maximum power we observed strong heating and bubbling30 while trapping large (micro) aggregates from Sample 3 and 4.

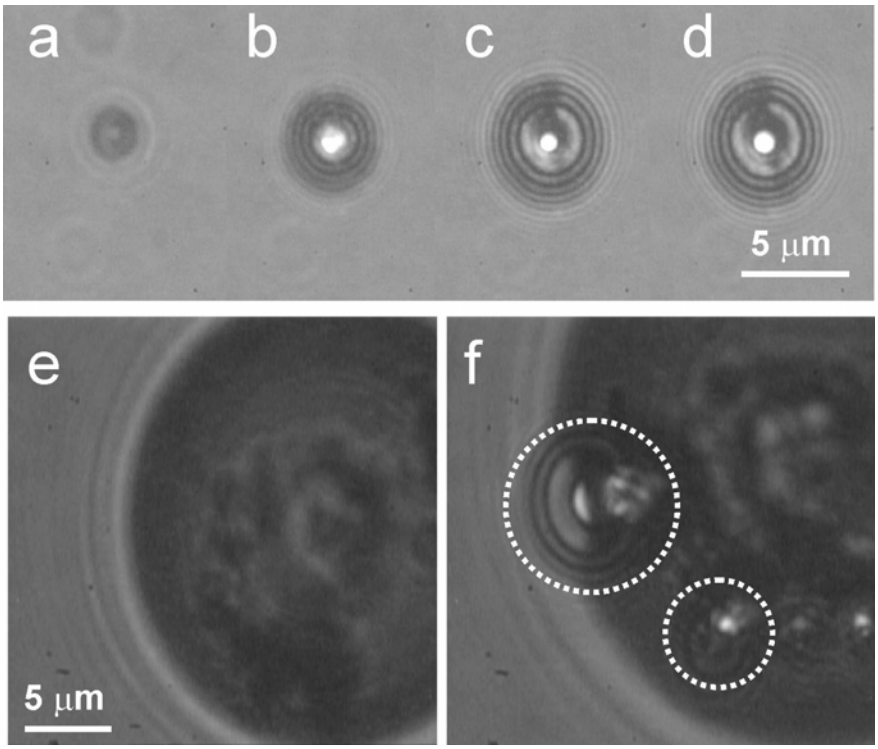

Fig.4.3: Heating of trapped large AuNPAs from Sample 3 and 4 at high laser power (32 mW on the sample) and consequent bubbling. (a-d) Image sequence of bubble formation and growth around a trapped aggregate from Sample 3. (e) A bubble formed around a large AuNPAs in Sample 4 draws other AuNPs in the region on the water-vapor interface. (f) Optical trapping of these particles at the interface yields laser heating that generates secondary bubbles (dashed circles).

In fig. 4.3a-d we show an image sequence of a bubble growth soon after a microaggregate from Sample 3 is drawn into the trap, the bubble growth lasts few seconds, until the bubble reaches a size of about 5-6 microns and the growth stops. In Sample 4 we observed growth of larger bubbles (20-30 micron) indicating a larger heating of the water surrounding the aggregates (fig.4.3e,f)

In our optical setup the same objective allows the imaging of the trapped nano and microparticles onto a CCD camera.

Figures 4.2c,d show images of AuNPAs from Sample 2 and Sample 4 respectively optically trapped at low power. In fig. 2c the size of the nanoaggregate is smaller than the diffraction limit of the imaging system. In fig. 4.2d the aggregate is aligned with the propagation axis[18] having a longitudinal extent at the micron scale (about 2 μm). This is revealed when the laser is switched off (fig. 4.2e) and the same aggregate is untrapped and free floating away from the trap. Moreover continuous rotation in the optical trap is observed for AuNPAs with a strong asymmetric morphology19 The rotation is a consequence of the particle shape i.e. anisotropic scattering causes rotation about the laser propagation direction[38] (the so-called “windmill effect”).

We perform radiation force measurements always with no rotation driven on the trapped particle. The distance from the coverslip is kept much larger than the particle average size, in the range 4-14 μm, where stable trapping is always ensured and the hydrodynamic perturbation of the bottom surface is negligible. Forces on trapped AuNPAs are measured through particle tracking and Brownian motion analysis [15,39] of the signals *Sx, Sy, Sz* from a quadrant photodiode (QPD) proportional to the trapped particle’s displacements in the three spatial directions (*x, y, z*) defined by the trapping potential. Figure 4.2b shows some representative particle tracking signals for trapped AuNPAs in the different samples.

An increase in the dimension of the trapped AuNPAs results in a larger amplitude of the recorded fluctuating signals.

The starting point of force sensing with optical tweezers is the Langevin equation in the confining harmonic potential [15,17]:

$$V(x) = \Sigma \tfrac{1}{2} k_i x_i^2$$

with the k_i being the spring constants.

For a trapped particle with an hydrodynamic radius r this can be written as:

$$\partial_t x_i(t) = -\omega_i x_i(t) + \xi_i(t), \qquad i=x,y,z \qquad (1)$$

where the relaxation frequency

$$\omega_i = k_i / \gamma$$

are related to the force constants and hydrodynamic (viscous) damping

$$\gamma = 6\pi\eta r$$

(Stokes' law), being η the dynamic viscosity of water.The terms ξi(t) describe random uncorrelated fluctuations with zero mean:

$$\langle \xi_i(t) \rangle = 0 \quad \text{and} \quad \langle \xi_i(t)\xi_j(t+\tau) \rangle = 2D \cdot \delta(\tau)\delta_{ij}$$

Where the angled brackets indicate a time-averaged quantity and $D=k_BT/\gamma$ is the diffusion constant (Einstein's relation) dependent on temperature T and damping [15]. In order to get the spring constants from experimental particle tracking signals, we use a time domain

analysis[17,19] of the thermal fluctuations in the trap by looking at their autocorrelation functions[15]

$$C_{ii}(\tau) = \left\langle x_i(t)\ x_i(t+\tau) \right\rangle$$

This method has been shown to be very successful for accurate measurements of optical forces[40] and torques[17,41], hydrodynamic interactions[42], optically induced rotations[19].

From Eq. 1 autocorrelations obey first order uncoupled differential equations with the lag time τ that can be easily integrated giving exponential decays with relaxation frequencies ωi and zero point value:

$$C_{ii}(0) = k_B T / \gamma\omega_i$$

Typical autocorrelation analysis of the tracking signals for a trapped AuNPA from Sample 2 is shown in fig. 4.4.

By fitting these data with an exponential decay we get the relaxation rates ω_x= (5010 ± 70) s^{-1}, ω_y= (6500 ± 100) s^{-1}, ω_z= (620 ± 5) s^{-1}.

We now calculate the hydrodynamic damping coefficient from the Stokes' law by approximating the nanoaggregate hydrodynamic radius to the average radius r=45 ± 15 nm obtained from several TEM images of AuNPAs in Sample 2.

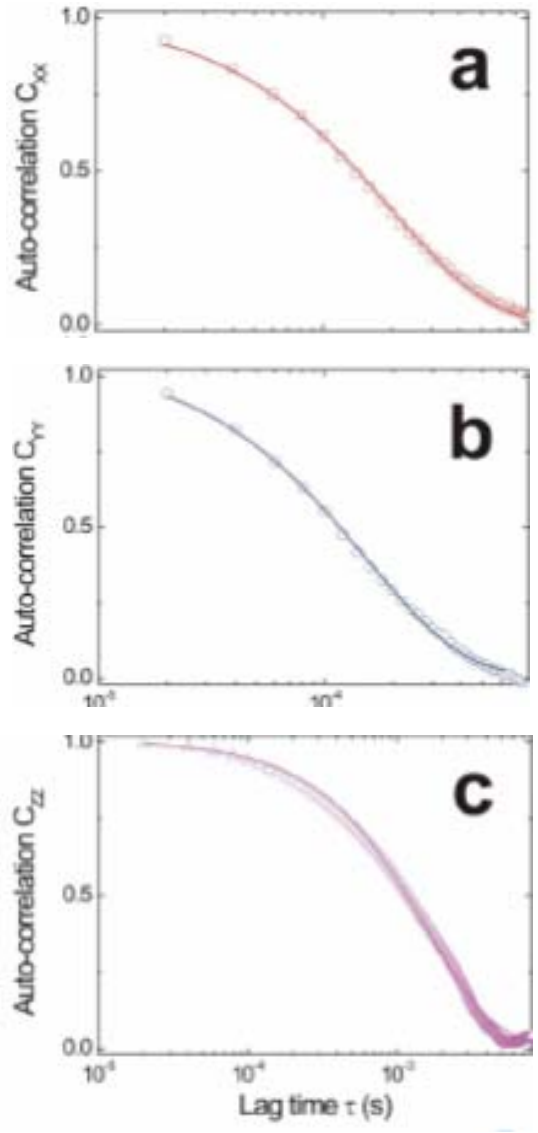

Fig. 4.4: Normalized auto-correlation functions of the tracking signals along the polarization x-axis (a), y-axis (b) and propagation z-axis (c) for a gold nanoaggregate from Sample 2.

Thus γ=(0.77 ± 0.25) fN·s/μm and the corresponding spring constants for this specific data are k_x=(3.9 ± 1.3) pN/μm, k_y=(5.0 ± 1.7) pN/μm, k_z=(0.48 ± 0.15) pN/μm.

The error on these values takes into account the approximation and deviation on the size of the aggregate coming from TEM analysis that propagates through the damping coefficient. Despite the spherical approximation might seem too extreme for the larger and more asymmetric aggregates, we note that even a factor of five in the asymmetry only changes the hydrodynamic damping by only 10% [17,43].

Thus we followed the same procedure for all our samples and studied the general behaviour of the radiation force with the increase of aggregation. We trapped and analyzed ten different aggregates for each sample and averaged the resulting relaxation frequencies and spring constants. These results are shown in fig. 4.5.

In fig.4.5a we plot the autocorrelation decay rates as a function of the lower energy plasmon resonance wavelength measured from extinction (fig.4.1b). The uncertainty on the relaxation rates represent the standard deviation on the measurements for each sample. We then show in fig. 4.5b, c, and d the force constants normalized to power k_i/P, that is a measure of the optical trapping efficiency, as a function of the average radius of the AuNPAs for each sample. Both decay rates and spring constants along the optical (z-)axis are lower than the ones in the transverse plane and the spring constants along the polarization (x-)axis are lower than the ones along the y-direction, as we expect due to the focusing properties of a linearly polarized laser beam at the diffraction limit1[8,29]. The measured force constants for the aggregates (red, green,

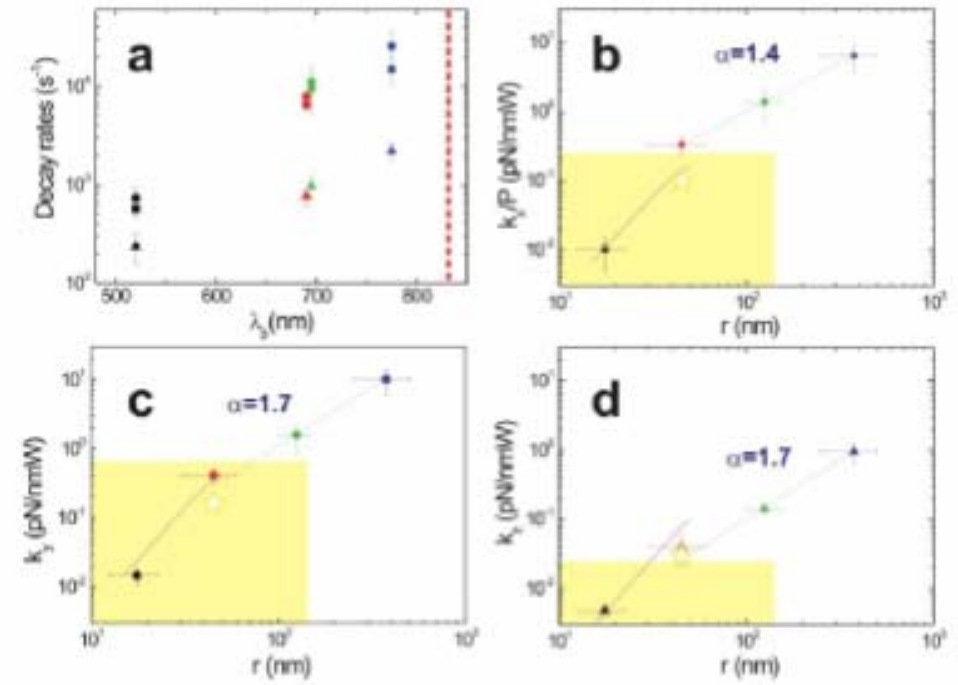

Fig. 4.5: (a) Auto-correlation decay rates ωx (squares), ωy (circles), and ωz (triangles) as a function of the plasmon resonance peak wavelength p. Black symbols are related to the non aggregated Sample 1 with resonance at 520 nm, while red, green and blue are related to Sample 2, 3 and 4 respectively with higher aggregation and a longer wavelength plasmon peak. The vertical red line identifies the trapping wavelength at 830 nm always red-shifted from resonance. The plotted values are averaged over measurements on ten different gold nanostructures in each sample. Error bars are the standard deviation over these measurements. In (b), (c) and (d) we show the force constants kx (along the polarization axis), ky and kz (along the propagation axis) normalized to the power at the sample (15 mW). Particles in Sample 4 with an average size of ~750 nm are trapped with force constants as high as 10 pN/nmW, the largest trapped particle size for this sample. Data are well fitted with a power law scaling, from which we can get a slope α~1.6 taken as the average of the fitted exponents for the three data sets. The purple solid line is the theory for spherical particles optically trapped at 830 nm. The yellow regions are defined by the maximum trapping efficiency and radius obtained in experiments with gold spherical particles.

blue data) are between 50 and 1000 times larger than the values measured for their constituents spherical AuNPs in Sample 1 (black data).

Moreover for AuNPAs in Sample 4 with an average radius of about 750 nm we measured force constants as high as 10 *pN/nmW*, a value 50 times larger than the maximum value reported in experiments with the largest (r=127 nm) gold spherical particles [23,28,29] (yellow region in fig. 4.5 b, c, d).

In conclusion, we have shown that gold nanoaggregates of controlled size and properties can be stably trapped with optical tweezers working in the near-infrared. Plasmonic nanostructures made by AuNPs with controlled extinction properties and average radii in the 20-750 nm range were obtained by a two step procedure consisting in PLAL of AuNPs and their controlled aggregation. The strong field enhancement driven by the nanoaggregates yields an increase in the trapping efficiency by a factor of 50 higher than previously reported for individual spherical gold nanoparticles. Force constants of the order of 10 pN/nmW were measured for the largest aggregates with 750 nm average radius. These larger trapping efficiencies and wider particle size range open perspectives for the use of gold nanoaggregates as improved local Raman probes in liquid environment with a three dimensional position control at the nanometer scale, as well as nano-handles for in vivo manipulation of larger biological material. Further analysis are in progress

References

[1] Maier, S.A. Plasmonics: Fundamentals and Applications, Springer, (2007)**.**

[2] Brongersma, M.L.; Kik, P.G. Surface Plasmon Nanophotonics, Springer Series in Optical Sciences, (2007)**.**

[3] Mafuné, F.; Kohno, J.; Takeda, T. and Kondow, T., *J. Phys. Chem. B* ,(2002), **106,** 7575.

[4] Wang, Y.; Xie, X. and Goodson, T., *Nano Lett.* (2005), **5**, 2379.

[5] Yang, G. W., *Progr. Mater.Sci*.(2007), **52**, 648.

[6] Compagnini, G.; Messina, E.; Puglisi, O.; Cataliotti, R.S. and Nicolosi, V., *Chem. Phys. Lett.*, (2008), **457**, 386.

[7] Menéndez-Manjòn, A.; Chichkov, B.N.and Barcikowski, S.. *J. Phys. Chem. C*, (2010), **114**, 2499.

[8] Liu, P.; Cui, H.; Wang, C.X. and Yang, G.W., *Phys. Chem. Chem. Phys.* , (2010), **12**, 3942.

[9] Kreibig, U. and Vollmer, M. *Optical properties of Metal Clusters*, (1995)

[10] Kneipp, K.; Moskovits, M. and Kneipp, H. (Eds.), Surface-enhanced Raman scattering: physics and applications, Springer, (2006).

[11] Xu, H.; Bjerneld, E.J; Kall, M. and Börjesson, L., *Phys. Rev. Lett.* (1999), **83**, 4357.

[12] Ashkin, A.; Dziedzic, J.M.; Bjorkholm, J.E. and Chu, S., *Opt. Lett.* (1986), **11**, 288.

[13] Ashkin, A., *Optical Trapping and Manipulation of Neutral Particles Using Lasers*, World Scientific Publishing, Singapore, (2006).

[14] Grier, D.G.A., *Nature* (2003), **424**, 810.

[15] Maragò, O.M.; Jones, P.H. and Gucciardi, P.G. *Scanning Probe Microscopy in Nanoscience and Nanotecnology*, (2010).

[16] Nakayama, Y.; et al., *Nature*, (2007), **447**, 1098.

[17] Maragò, O.M.; et al. *Nano Lett*., (2008), **8**, 3211.

[18] Borghese F.; et al. *Phys. Rev. Lett.* (2008), **100**, 163903.

[19] Jones, P.H.; et al. *ACS Nano*,(2009), **3**, 3077.

[20]Neves, A.A.R.; et al. *Opt. Express*, (2010)**, 18**,822.

[21] Petrov, D.V., *J. Opt. A: Pure Appl. Opt.*, (2007), **9**, S139.

[22] Svoboda, K. and Block, S.M., *Opt. Lett.*, (1998), **28**, 930.

[23] Hansen, P.M.; Bhatia, V.K.; Harrit, N. and Oddershede L., *Nano Lett.*, (2005), **5**, 1937.

[24] Seol, Y; Carpenter, A.E. and Perkins, T.T., *Opt. Lett*., (2006), **31**, 2429.

[25] Pelton, M.; et al., *Opt. Lett.*,(2006)**, 31**, 2075.

[26] Bosanac, L.; Aabo, T.; Bendix, P.M. and Oddershede, L.B. *Nano Lett*., (2008), **8**, 1486.

[27] Selhuber-Unkel, C.; et al. *Nano Lett.*, (2008), **8***,* 2998.

[28] Hajizadeh, F.; Nader, S. and Reihani, S., *Opt. Exp.*, (2010), **18**, 551.

[29] Saija, R.; Denti, P.; Borghese, F.; Maragò, O. and Iatì, M.A., *Opt. Exp.* , (2009), **17**, 10231

[30]Liu, Z.; Hung, W.H.; Aykol, M.; Valley, D. and Cronin, S.B. *Nanotechnology*, (2010), **21**, 105304

[31] Zhang, Y.; et al., *Phys. Rev. B*, (2006), **73**, 165405.

[32] Amendola, V. and Meneghetti, M., *J. Mater. Chem.*, (2007), **17**, 4705.

[33] Amendola, V. and Meneghetti, M., *J. Phys. Chem. C.*, (2009), **113**, 4277.

[34] Amendola, V. and Meneghetti, M. *Phys. Chem. Chem. Phys*.(2009), *11*, 3805.

[35] Blatchford, C.G.; Campbell, J.R. and Creighton, J.A., *Surf. Sci.* (1982), **120**, 435.
[36] Galletto, P.; Brevet, P.F.; Girault, H.H.; Antoine, R. and Broyer, M. , *J. Phys. Chem. B*, (1999), **103**, 8706.
[37] Park, S.Y.; Lee, J.S.; Georganopoulou, D.; Mirkin, C. A.; Schatz, G. C., *J. Phys. Chem. B*, (2006), **110***,* 12673.
[38] Galajda, P.; Ormos, P. *Appl. Phys. Lett.*,(2001), **78**, 249.
[39] Pralle, A.; Prummer, M.; Florin, E.L.; Stelzeer, E. H. K. and Horber, J.K.H., *Microsc. Res.Tech*., (1999), **44**, 378.
[40] Rohrbach, A., *Phys. Rev. Lett*., (2005), **95**, 168102.
[41]Volpe, G. and Petrov, D. *Phys. Rev. Lett*., (2006), **97**, 210603.
[42] Martin, S.; Reichert, M.; Stark, H. and Gisler, T., *Phys. Rev. Lett.*, (2006), **97**, 248301.
[43] Broersma, S., *J. Chem. Phys.*, (1981), **74**, 6989.
[44] Borghese, F.; Denti, P. and Saija, R. Scattering from model nonspherical particles, (2007).
[45] Borghese, F.; Denti, P.; Saija, R. and Iatì, M. A., *Opt. Express,* (2007), **15**, 11984.
[46] Johnson, P.B. and Christy, R.W., *Phys. Rev. B*, (1972), **6**, 4370.
[47] Lindhard, J. Kgl. Danske Videnskab. Selskab, *Mat.-Fys. Medd.* (1954), **28**, 8.
[48] Pack, A.; Hietschold, M.; Wannemacher, R.,*Opt. Comm.*,(2001), **194**, 277..
[49] Maragò, O.M.; et al., *Physica E*, (2008), **8**, 2347.